

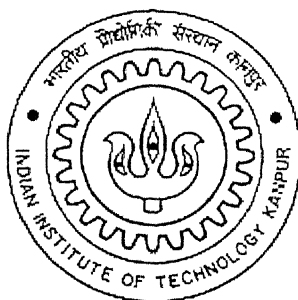
# **A NEW STEP TO EXPLORE THE MODERATE INVERSION REGION FOR SHORT CHANNEL MOSFETS: UNIFIED MOBILITY AND DRAIN CURRENT MODELS AND AN IMPROVED THRESHOLD VOLTAGE MODEL ALONG WITH ITS EXTRACTION PROCEDURE**

*A Thesis submitted in Partial Fulfillment of the Requirements  
for the degree of*

**Master of Technology**

*by*

**Santanu Mahapatra**



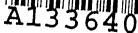
*to the*

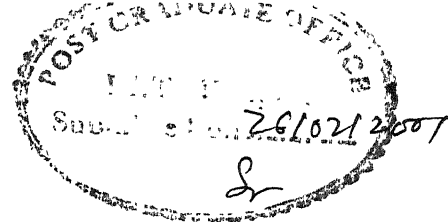
**DEPARTMENT OF ELECTRICAL ENGINEERING  
INDIAN INSTITUTE OF TECHNOLOGY, KANPUR**

*February, 2001*

3117-110

133649





# Certificate

This is to certify that the work contained in the thesis entitled **“A New Step to Explore the Moderate Inversion Region for Short Channel MOSFETs: Unified Mobility and Drain Current Models and an Improved Threshold Voltage Model along with its Extraction Procedure”**, by **Santanu Mahapatra** (Roll No. 9910473) has been carried out under my supervision and that this work has not been submitted elsewhere for the award of a degree.

A handwritten signature, likely of Dr. Alope Dutta, with a horizontal line drawn across it. Below the signature, the date "23/2/01" is handwritten.

**(Dr. Alope Dutta)**

Associate Professor

Department of Electrical Engineering,  
Indian Institute of Technology Kanpur,  
Kanpur - 208016, INDIA  
February 2001

# Acknowledgements

*I am deeply indebted to my thesis supervisor **Dr. Alope Dutta** for his invaluable guidance and encouragement. His teaching was a pleasant experience. He helped me not only in my academics but in my times of trouble as well. Without him this work would not have been possible. A few lines are grossly insufficient to thank him.*

*Also I am grateful to my teachers **Dr. Utpal Das, Dr. Baqer Mazhari, Dr. Samares Kar and Dr. Ajai Jain** whose courses have built the foundation upon which this work is based.*

*I would like to express my sincere gratitude to **Dr. Adelmo Ortiz-Conde**, Departamento de Electrónica, Universidad Simón Bolívar, Caracas, Venezuela and **Dr. Giuseppe Ferri**, Department of Electrical Engineering, University of L'Aquila School of Engineering, Italy. Without their kind co-operation this work could never have finished in time.*

*I would like to thank all of my classmates, especially, **Srikanth, Bhanu and Kamalesh** for their constant support and company. Thank you **Raju** for providing the excellent computing facility in the **Mayukh Lab**. Thank you **Argha, Prithwi, Arup and Debjit-da** for standing beside me.....and.....**Anindya (IISc. Bang'lore)**...thanks a lot...without your help I couldn't do this work. And finally my stay at **IIT Kanpur** wouldn't be the same, had it not been for my friends **Rama, Rajrup, Kaustuv, Sona, Rupen, Balu, Sougata and Arindam**.*

*Santanu Mahapatra*



# ABSTRACT

*A semi-empirical unified mobility model dedicated to the modeling of short channel length MOSFETs for low power analog applications has been developed in this work. The existing BSIM mobility model is taken up and modified here in order to incorporate the Coulomb scattering effect, which plays the dominant role in determining the effective mobility of the channel electrons in the moderate inversion region. Using the proposed mobility model, a new drain current model for the quick calculation of the drain current in the moderate inversion region has also been developed in this work. In addition to this, a new unified drain current model valid for all the three regions (i.e., the weak inversion, the moderate inversion, and the strong inversion) is presented in this work. Results obtained from the proposed model have been verified with the experimental data reported in the literature for 0.26  $\mu\text{m}$  and 0.09  $\mu\text{m}$  channel length MOSFETs, which show a perfect match between the experimental data and the simulated model characteristics.*

*Another important issue for the low-power-analog-IC applications is the proper modeling and extraction of the device threshold voltage parameter. In this work, a new model for the threshold voltage at the 'onset of the moderate inversion region' along with its extraction procedure have been proposed. The development of this extraction method is based on two new integral functions  $\mathcal{V}_x$  and  $I_x$  proposed in this work, which are insensitive to the drain and source series*

resistances of the device and the experimental noise error. The results obtained from the proposed model are compared with the recently reported experimental data for 0.26  $\mu\text{m}$  and 0.09  $\mu\text{m}$  channel length devices and its reliability (i.e., short and narrow channel effects, and the parasitic series resistance effect on the proposed extraction method) is also tested and compared with the other existing methods by means of the AIM-SPICE circuit simulator. The results reveal that the determined threshold voltage values always meet the 'onset of the moderate inversion region' condition, and that, this extraction procedure is insensitive to the drain and source parasitic series resistances and the noise introduced during measurements.

# Contents

<b>List of Figures</b>	iv
<b>1. Introduction</b>	<b>1</b>
1.1 Device Models .....	3
1.2 The Deficiency of The Existing Mobility Models .....	4
1.3 Parameter Extraction .....	5
1.4 Challenges of the Threshold Voltage Extraction .....	5
1.5 Goals .....	7
<b>2. Theoretical Background</b>	<b>9</b>
2.1 The Electron Mobility .....	9
2.2 The Scattering Mechanisms .....	11
2.2.1 The Coulomb Scattering Effect .....	12
2.2.1.1 The Ionized Impurity Scattering .....	12
2.2.1.2 The Remote Charge Scattering (RCS) .....	12
2.2.2 The Phonon Scattering Effect .....	14
2.2.3 The Surface Roughness Scattering Effect .....	16
2.3 The Screening Effect .....	17
2.4 The Effective Mobility .....	18
2.5 The Threshold Voltage ( $V_T$ ) .....	25
2.6 The Drain Current Model .....	28

2.6.1	The Drain Current Model in the Subthreshold Region .....	28
2.6.2	The Drain Current Model in the Strong Inversion Region .....	29
<b>3.</b>	<b>Development of the Mobility Model</b>	<b>31</b>
3.1	The Definition of the Threshold Voltage .....	31
3.2	Development of the Modified Drain Current Model .....	35
3.3	Modeling of the Inversion Charge .....	36
3.4	The Proposed Mobility Model .....	37
3.5	The Drain Current Model in the Moderate Inversion Region .....	40
<b>4.</b>	<b>Model Verification and Discussions</b>	<b>43</b>
4.1	The Modified Drain Current Model .....	43
4.2	Parameter Extraction .....	45
4.3	Comparison Between the BSIM Mobility Model and the Proposed Mobility Model .....	46
4.4	Verification of the Proposed Drain Current Model .....	50
<b>5.</b>	<b>Development of the Threshold Voltage Extraction Method</b>	<b>55</b>
5.1	The ‘Difference Function’ $D$ .....	56
5.2	The Properties of the ‘ $D$ Function’ .....	57
5.3	The ‘ $G$ Function’ .....	58
5.4	The ‘ $V_x$ Function’ and the ‘ $I_x$ Function’ .....	59
5.5	Case of a Constant Series Resistance .....	60

<b>6. Threshold Voltage Extraction</b>	<b>63</b>
6.1 Description of the Procedure .....	63
6.2 The Mathematical Foundation .....	64
6.3 Analysis .....	68
6.4 Verification of the Proposed Method with the Experimental result for sub- 0.1 $\mu\text{m}$ Devices .....	74
6.5 Further Analysis .....	76
6.6 Extraction of $V_{\text{TS}}$ .....	80
<b>7. Reliability Test of the Proposed Method</b>	<b>82</b>
7.1 Effect of Channel Length on the Threshold Voltage ( $V_{\text{TM}}$ ) .....	82
7.2 Effect of Channel Width on the Threshold Voltage ( $V_{\text{TM}}$ ) .....	84
7.3 Effect of Source/Drain Series Resistance on the Extraction of the Threshold Voltage ( $V_{\text{TM}}$ ) .....	87
7.3.1 The Spreading Resistance ( $R_{\text{sp}}$ ) .....	88
7.3.2 The Sheet Resistance ( $R_{\text{sh}}$ ) .....	88
7.3.3 The Contact Resistance ( $R_{\text{co}}$ ) .....	90
7.4 Mathematical Complexity of the Proposed Method .....	91
<b>8. Summary and Conclusion</b>	<b>95</b>
8.1. Summary of the Work .....	97
8.2. Scope for Improvement .....	100
<b>References</b>	<b>101</b>
<b>Appendix</b>	<b>I</b>

# List of Figures

2.1	Measured phonon spectra in silicon as a function of the wave vector along the [001] direction. The legends TO, LO, TA, and LA stand for transverse optical mode, longitudinal optical mode, transverse acoustic mode, and longitudinal acoustic mode respectively (after Sze [21]). .....	15
2.2	Schematic diagram for the comparison between the screened and the unscreened Coulomb potential of a static charge, as a function of the radial distance. ....	19
2.3	The effective electron mobility ( $\mu_{\text{eff}}$ ) at 300 K and 77 K in n-channel MOSFETs versus the effective normal field $E_{\text{eff}}$ , for varying substrate acceptor concentrations ( $N_A$ ), as given by Takagi <i>et al.</i> [2]. ....	21
2.4	Schematic diagram of the effective electric field ( $E_{\text{eff}}$ ) dependence of the carrier mobility in the inversion layer by the three dominant scattering mechanisms, i.e., the phonon scattering ( $\mu_{\text{ph}}$ ), the surface roughness scattering ( $\mu_{\text{sr}}$ ), and the Coulomb scattering ( $\mu_c$ ), as given by Takagi <i>et al.</i> [2]. ....	22
2.5	Inversion carrier density ( $N'_i$ ) dependence of $\mu_c$ for n-channel MOSFETs with varying substrate impurity concentrations ( $N_A$ ), after Takagi <i>et al.</i> [2]. ....	24

3.1	Schematic diagram of the variation of the surface potential $\Psi_S$ with respect to the gate-to-source voltage $V_{GS}$ for a typical MOSFET device, as presented by Tsividis [11]. .....	33
3.2	Plots of $U(V_{GS})$ versus $V_{GS} - V_{TM}$ for four values of $M$ . .....	39
3.3	Plots of the functions $f(V_{GS})$ and $h(V_{GS})$ as a function of $V_{GS} - V_{TM}$ for three values of $\zeta$ . .....	41
4.1	Comparison of the $I_D$ versus $V_{GS}$ characteristics obtained from the proposed model with the experimental data for a $0.26 \mu m$ channel length MOSFET, as reported by Langevelde and Klaassen [15]. This comparison has been shown both in log scale (in left) and in linear scale (in right). .....	47
4.2	Comparison between the traditional BSIM mobility model with the model proposed in this work, based on the experimental data for a $0.26 \mu m$ channel length MOSFET, as reported by Langevelde and Klaassen [15]. .....	49
4.3	Comparison of the $I_D$ versus $V_{GS}$ characteristics obtained from the proposed drain current model [Eq.(4.11)] with the experimental data for a $0.26 \mu m$ channel length MOSFET, as reported by Langevelde and Klaassen [15]. .....	52
4.4	Comparison of the $I_D$ versus $V_{GS}$ characteristics obtained from the proposed drain current model [Eq.(4.11)] with the experimental data for a $0.09 \mu m$ channel length MOSFET, as reported by Mii <i>et al.</i> [16]. .....	54

5.1(a)	The $I_D$ - $V_{GS}$ characteristics of an n-MOSFET for four different values of series source/drain resistances, simulated with the help of the AIM-SPICE simulator (Level -10) [7]. .....	62
5.1(b)	The $I_x$ - $V_x$ characteristics obtained from Fig.5.1(a) for the same values of series resistances as in Fig.5.1(a). .....	62
6.1	The $I_x$ function calculated numerically from the experimental data, as reported by Langevelde and Klaassen [15], as a function of $V_{GS}$ and $V_x$ . .....	65
6.2	The $I_x$ function calculated numerically from the experimental data as reported by Langevelde and Klaassen [15] as a function of $V_{GS}$ and $V_x$ (curves B and C respectively). The results simulated from the theoretical model of $I_x$ [Eqs.(6.4) and (6.5)] proposed in this work is also shown as a function of $V_{GS}$ (curve A) for comparison. ....	69
6.3	Comparison of the $I_D$ versus $V_{GS}$ characteristics obtained from the proposed subthreshold component of the drain current model [Eq.(6.2)] with the experimental data for a 0.26 $\mu m$ channel length MOSFET, as reported by Langevelde and Klaassen [15]. These two characteristics exhibit a close match till $V_{GS} = V_{2\phi} = 0.38$ V, however, they differ afterwards. ....	71
6.4	The $I_x$ function calculated numerically from the experimental data as reported by Mii <i>et al.</i> [16] as a function of $V_{GS}$ and $V_x$ (curves B and C respectively). The results simulated from the theoretical model proposed in this work for $I_x$	



	[Eqs.(6.4) and (6.5)] are also shown as a function of $V_{GS}$ (curve A) for comparison. ....	75
6.5	The $I_x$ function calculated numerically from the experimental data as reported by Langevelde and Klaassen [15] as a function of $V_{GS}$ . The results simulated from the theoretical model of $I_x$ [Eq.(6.11)] proposed in this work are also shown as a function of $V_{GS}$ for comparison. ....	78
6.6	The $I_x$ function calculated numerically from the experimental data as reported by Mii <i>et al.</i> [16] as a function of $V_{GS}$ . The results simulated from the theoretical model proposed in this work for $I_x$ [Eq.(6.11)] are also shown as a function of $V_{GS}$ for comparison. ....	79
7.1	Simulated values of the threshold voltage extracted by the GMLE method [9], the TC method [13], and the method proposed in this work as a function of the channel length (based on the results from AIM-SPICE simulation). ....	86
7.2	Simulated values of the threshold voltage extracted by the GMLE method [9], the TC method [13], and the method proposed in this work as a function of the channel width (based on the results from AIM-SPICE simulation). ....	86
7.3	A schematic cross section showing the pattern of current flow from a MOSFET channel through the source or drain region to the aluminum contact [31]. The diagram identifies various contributions to the series resistance. ....	89
7.4	A schematic diagram showing the resistance component associated with the	

	injection region where the current spreads from a thin surface layer into a uniformly doped source or drain region [31]. .....	89
7.5	Comparison of the percent error in the extraction of the threshold voltages using the GMLE method [9], the TC method [13], and the method proposed in this work as a function of S/D resistance, based on the results of AIM–SPICE simulation. ....	92
7.6	The $I_x$ function calculated numerically from the experimental data, as reported by Langevelde and Klaassen [15], as a function of $V_{GS}$ for two different integration limits. ....	94
7.7	The $I_x$ function calculated numerically from the experimental data, as reported by Mii <i>et al.</i> [16], as a function of $V_{GS}$ for two different integration limits. ....	94

## Introduction

---

Throughout the past four decades, both the productivity and the performance of microelectronics have advanced at exponential rates unmatched in technological history. Consequently, microelectronics has become the principal driver of the modern information revolution and the ubiquitous microchip has had a profound and pervasive impact on our daily lives – enabling such advances as microelectronic wrist watches, hearing aids, implantable cardiac pacemakers, pocket calculators, personal computers, wireless cellular telephones, optoelectronic-fiber networks, communication satellites, and the Internet. Propelled by the rapid advances made in the fabrication technology over the last four decades, the number of transistors per microchip has skyrocketed to about 100 million or more, while the cost of a chip has fallen constantly. The ever shrinking device dimensions, made possible by the improvements in the photolithography techniques, are essentially responsible for such a high packing density.

Computer Aided Design (CAD) and simulation of electronic circuits are the main factors contributing to the success of VLSI. For accurate simulation of electronic circuits, the devices used in the circuits must be modeled accurately. The modeling of MOS transistors for CAD has been driven by the needs of digital circuit designers for many years. However, when these same

models are used for analog work, the outcome is very different: analog circuit behavior, as predicted through the use of such models, can have serious errors [1]. Thus, the rapid growth in low-power, low-voltage analog IC design imposes tighter requirements on the model accuracy.

The continuous scaling down of MOS devices due to rapid advancements made in VLSI technologies require analog circuits to operate with a power supply voltage of less than 5 Volts, with a strong tendency to go further down to 3.3 Volts and below in the near future. At the same time, the development of high-performance portable equipment (e.g., radio receivers, disk drive filters, medical aids, etc.) requires the design of analog circuits having low power drain. The power consumption in analog ICs can be greatly reduced if the amplifiers are designed to work in the weak inversion region (as this region offers a low drain current) and, thus, the thermal cross talk between the devices gets reduced and consequently, the packing density gets boosted. However, the low drain current in this region also tends to degrade the speed of the circuit. Therefore, as the operating region of the device approaches the weak inversion, the packing density and the low power consumption will tradeoff with the speed of the circuit. Hence, in most analog circuits, the best tradeoff among area, power, and speed can be achieved when the devices work in the moderate inversion region, which lies in between the weak inversion region and the strong inversion region. With analog VLSI gaining popularity day by day, the moderate inversion region of operation of MOSFETs is becoming increasingly important for analog circuit designers. Therefore, an accurate modeling of the drain current in this region becomes an essential step in low power mixed-signal circuit design.

Another important feature of the modern low power analog IC applications is that the devices are typically biased just above the threshold voltage ( $V_T$ ) in order to reduce the dc power

dissipation. Thus, the threshold voltage is becoming a key parameter in MOSFET device design, characterization, modeling, and simulation, particularly for modern devices with very small geometry and relatively low power supply voltage. Hence, an accurate definition and extraction of this parameter is extremely important.

## 1.1 Device Models

Mathematically, a device model is an approximation of the device behavior, which can be measured or obtained from device characterization. It is a set of mathematical equations, which describe the physical behavior of the device under various input conditions. The accuracy of a model is determined from the deviation of the behavior predicted by the model from the measured behavior, e.g., from the current-voltage (I-V) characteristics. The reasons why MOSFET modeling for circuit simulation is still precarious are manifold. One reason is the improvement in the fabrication technology: device models based on long-channel MOSFETs with high power supply voltages are losing their validity currently, simply because modern high-performance MOSFETs feature extremely short channel lengths and are operated with a lower power supply voltage. Another reason is the interaction between the circuit complexity and the sensitivity to modeling errors: small errors in the measured device terminal characteristics and even smaller errors in their derivatives may turn into large errors during circuit simulation, or even worse, these may create convergence problems in the simulations. In devices fabricated from advanced deep-submicron CMOS processes, various short-channel effects occur, e.g., the Drain Induced Barrier Lowering (DIBL) effect, the dependence of the threshold voltage ( $V_T$ ) on the channel length ( $L$ ) and the channel width ( $W$ ), etc. It is virtually impossible to account for all these effects accurately with a simple, physically based model. Consequently, the number of

model parameters increases, with most of these being merely fitting parameters without having much physical justifications.

## 1.2 The Deficiency of the Existing Mobility Models

The carrier mobility in the inversion layer of a MOSFET is an important parameter in the simulation of its drain current characteristics. The model for the effective carrier mobility in silicon inversion layers and in the bulk of the semiconductor is the one, which mostly affects the accuracy of the results of the terminal current calculations for a MOSFET. The effective mobility ( $\mu_{\text{eff}}$ ) of the inversion layer electrons is mainly dependent on the Coulomb scattering effect (i.e., the scattering due to the ionized impurities), the phonon scattering effect (i.e., the scattering due to the lattice vibration), and the surface roughness scattering effect (i.e., the scattering due to the surface states) [2,3]. It is found [2] that, in the moderate inversion region,  $\mu_{\text{eff}}$  is mainly determined by the Coulomb scattering effect, whereas in the strong inversion region, the phonon and the surface roughness scattering effects play the dominant role in order to govern the effective mobility ( $\mu_{\text{eff}}$ ). It is also found that the Coulomb scattering effect is a linear function of the inversion charge density [2,4]. Therefore,  $\mu_{\text{eff}}$  increases with an increase in the gate to source voltage ( $V_{\text{GS}}$ ) in the moderate inversion region, where the effects of the other two scattering mechanisms are not that marked. However, as the phonon and the surface roughness scattering effects are decreasing functions of  $V_{\text{GS}}$  [2], hence,  $\mu_{\text{eff}}$  decreases with increasing  $V_{\text{GS}}$  in the strong inversion region [5]. The BSIM mobility model [6], which is widely used for circuit simulation, considers only the phonon and the surface roughness scattering effects and ignores the effect of the Coulomb scattering. As a result, although the BSIM model gives quite accurate results in the strong inversion region, however, it seems to lose its validity in the moderate

inversion region. Hence, for low power analog IC design purpose, it is extremely important to define a mobility model, which is valid both in the moderate inversion region as well as in the strong inversion region.

## 1.3 Parameter Extraction

A device model is an abstract mathematical representation of the actual physical phenomena occurring in the device, which can be used to predict the behavior of the device under known stimulation with a reasonable accuracy. In order to apply a particular device model in circuit simulation, it is necessary to find a practical way of extracting the model parameters from the experimental data. The accuracy of the parameter extraction procedure depends on the accuracy of the model and on the accuracy and completeness of the experimental data. The parameter extraction procedure should be such that it gives fairly reasonable results without parameter adjustment, and can produce a nearly perfect fit to the device characteristics, and, hence, predict the circuit performance fairly accurately using popular circuit or device simulators (e.g., AIM-SPICE [7], MICROTEC [8], MEDICI [9,10], etc.).

## 1.4 Challenges of the Threshold Voltage Extraction

To date, several definitions [8,11] and methods [9,10,12–14] have been presented in the literature in order to define and extract the threshold voltage ( $V_T$ ) parameter. The popular methods frequently used for  $V_T$  extraction from the measured drain current ( $I_D$ ) versus gate-to-source voltage ( $V_{GS}$ ) characteristics are

- 1) the constant current (CC) method [12],

- 2) the transconductance change (TC) method [13],
- 3) the ratio method [14],
- 4) the difference function (D) method [10], and
- 5) the transconductance ( $g_m$ ) linear-extrapolation (GMLE) method [9].

For designing low-power analog circuits, it is required that the definition of  $V_T$  and its extraction method should be

- 1) reliably applicable to the moderate inversion region, i.e., the region where the carrier concentration in the inversion layer starts to become comparable to the depletion charge density,
- 2) insensitive to the parasitic source/drain (S/D) series resistance and the surface roughness factor,
- 3) insensitive to the measurement error due to noise, etc., and
- 4) easily applicable to analog CAD tools.

Unfortunately, however, none of the existing  $V_T$  extraction methods, as illustrated earlier, satisfy these requirements simultaneously. Most of these methods use the derivative method (i.e., taking the derivative of  $I_D$  with respect to  $V_{GS}$ ) and the linear extrapolation technique (i.e., extrapolating the linear portion of the  $g_m$  versus  $V_{GS}$  characteristics) in order to extract  $V_T$  from the experimental data. However, both these techniques have some serious disadvantages. Firstly, if there is a measurement error due to noise, etc., then the error value will go higher after taking the derivative. Secondly, the extrapolation technique is highly sensitive to the S/D resistance and the surface roughness factor [13]. Since this technique depends upon the slope of the linear region of the  $I_D$  versus  $V_{GS}$  (or the  $g_m$  versus  $V_{GS}$ ) characteristics, it is obvious that this slope changes with



a variation in the parasitic series resistances. As reported by Wong *et al.* [13], the slope of the linear region of the  $I_D$ - $V_{GS}$  characteristics also depends upon the scattering caused by the surface roughness, since it degrades the effective mobility of the channel electrons. Therefore, the extracted value of  $V_T$  will be dependent upon the value of the S/D resistance and the surface roughness factor. On the other hand, the D-Method [10], which uses the integral function, is free from the parasitic resistance effect and the measurement errors. Thirdly, most of these methods (except the GMLE method) use the drain current model, which does not take into account the Coulomb scattering effect in the moderate inversion region. As the Coulomb scattering effect is the main factor which determines the effective mobility of the carriers in the channel in the moderate inversion region, hence, these drain current models fail to explain the device behavior in this region accurately. Moreover, they only consider the above threshold region (i.e., the drift region) of the experimental data in order to extract the threshold voltage. As a result, the extracted value of the threshold voltage cannot properly represent ‘the onset of the moderate inversion’. Rather, the threshold voltage extracted from these methods represents the ‘onset of the strong inversion’. Therefore, these methods are not suitable for the threshold voltage extraction for devices to be used in low-power analog circuit designs.

## 1.5 Goals

The moderate inversion region of a MOSFET is a special region of operation [1], with properties distinct from those of the strong inversion and the weak inversion regions. Hence, this region should not be considered just as a “transition” region between the strong inversion and the weak inversion regions, which is mainly used to maintain the continuity of the two characteristics in the two regions. Modern low power analog IC design demands a more accurate

and robust model for the drain current in the moderate inversion region. The goal of the present work is to provide an accurate model of the effective inversion layer electron mobility, which is valid both in the moderate inversion region as well as in the strong inversion region. The existing BSIM mobility model is taken up in this work and modified accordingly in order to make it applicable for both the moderate and the strong inversion regimes. The results obtained from the proposed model is then compared with the recently reported experimental results for 0.26  $\mu\text{m}$  [15] and 0.09  $\mu\text{m}$  [16] channel length devices, and this comparison shows a perfect match between the two.

The present work also addresses all the problems mentioned above with regard to the threshold voltage extraction for submicron channel length MOSFETs. In this work, an improved and unambiguous definition for the threshold voltage along with its accurate extraction procedure have been proposed, which takes into account the Coulomb scattering effect in the moderate inversion region, and, thus, is able to extract the value of the threshold voltage at the ‘onset of the moderate inversion region’. The threshold voltage extraction method developed in this work uses both the drift and the diffusion components of the drain current in order to determine the threshold voltage. Moreover, it uses the integration function rather than the differentiation techniques adopted by the earlier authors, and, thus, is insensitive to the S/D series resistance effect, and suppresses the experimental errors due to noise, etc. The universality and reliability of this method is demonstrated by simulation studies using the AIM-SPICE simulator with varying device parameters (e.g., gate length ( $L$ ), gate width ( $W$ ), and S/D series resistances ( $R_s$  and  $R_d$ )), as well as by comparing the results with the reported experimental data for 0.26  $\mu\text{m}$  [15] and 0.09  $\mu\text{m}$  [16] channel length devices. The results have shown a very good match among our simulation studies, the AIM-SPICE simulations, and the experimental data.

# Theoretical Background

---

The theoretical background required for an understanding of this work is briefly presented in this chapter. It highlights the basic concepts associated with MOSFETs, e.g., the threshold voltage model, the drain current model, the subthreshold region of operation, the scattering mechanisms, the mobility model, etc.

## 2.1 The Electron Mobility

Under low electric fields, the carrier drift velocity  $v$  is proportional to the electric field  $\mathcal{E}$ . Thus,

$$v = \mu_0 \mathcal{E}. \quad (2.1)$$

The coefficient of proportionality  $\mu_0$  is called the low field carrier mobility. This equation can be obtained from the second law of motion for an electron moving in an electric field, given by [17]

$$m_n^* \frac{dv}{dt} = q\mathcal{E} - m_n^* \frac{v}{\tau}, \quad (2.2)$$

where  $m_n^*$  is the electron effective mass and  $q$  is the electronic charge. The first term in the right-hand side of Eq.(2.2) represents the electron acceleration by the electric field, and the second

term describes the effects of the collisions of the electrons with the lattice vibrations, impurities, and crystal imperfections on this motion. This term limits the electron drift velocity and the electron drift momentum. The term  $\tau$  appearing in Eq.(2.2) is called the momentum relaxation time, and, usually, it is of the order of  $10^{-12}$  to  $10^{-14}$  s. Under steady state, the electrons attain a constant velocity, given by

$$v = q\tau \frac{\mathcal{E}}{m_n^*}. \quad (2.3)$$

Under low electric fields,  $\tau$  and  $m_n^*$  are independent of the electric field, hence, the carrier velocity  $v$  can be given by  $v = \mu_0 \mathcal{E}$ , where the low field electron mobility  $\mu_0$  can be expressed as

$$\mu_0 = q \frac{\tau}{m_n^*}. \quad (2.4)$$

It should be noted that this linear dependence of the electron drift velocity on the electric field does not hold good under high electric fields, where the electrons may gain a considerable amount of energy from the electric field. This process can be described by the following equation

$$\frac{dE}{dt} = q\mathcal{E} \cdot v - \left( \frac{E - E_0}{\tau_E} \right). \quad (2.5)$$

Here  $E$  is the electron energy,  $E_0 [= (3/2)kT]$  is the electron energy under the conditions of thermal equilibrium, and  $\tau_E$  is the effective energy relaxation time, and is usually of the order of  $10^{-11}$  to  $10^{-13}$  s. The low field mobility  $\mu_0$  is determined by the electron collisions with phonons and impurities. These collision processes are called the scattering mechanisms, and are discussed in the next section.

## 2.2 The Scattering Mechanisms

An electron moving in a periodic potential essentially behaves as a free electron, with the periodic potential only changing its mass from the rest mass to the effective mass. A perfectly periodic potential is, however, an idealistic assumption. This arrangement of the atoms in a perfect crystal is periodic, however, all the atoms move at all times about their equilibrium positions due to the thermal vibration at a given temperature. This vibration of the atoms changes the periodic nature of the potential. In addition, there are impurity atoms in semiconductors, either intentionally introduced (doping) or inadvertently got introduced during the various processing steps. The potential produced by these impurity atoms also alters the periodicity of the potential distribution. The potential distribution in a crystal can also be altered by crystal imperfections. Lastly, the description of the electron is built on the assumption that there is a single electron moving in the periodic potential. Other electrons when present are also expected to cause perturbation in the periodicity of the potential in their immediate vicinity. Due to these anomalies in the periodicity of the potential discussed above, an electron in a solid cannot execute long range motion without changing its state, which occurs when it arrives near a scattering center (e.g., impurity atoms, thermal vibrations of the lattice atoms, structural defects, etc.). The process causing the electron to change its state is called the collision process or the scattering process.

In MOSFET inversion layers, the effective mobility ( $\mu_{\text{eff}}$ ) of electrons mainly depends upon three scattering phenomena:  $\mu_c$ , due to the Coulomb scattering;  $\mu_{\text{ph}}$ , due to the phonon scattering; and  $\mu_{\text{sr}}$ , due to the surface roughness scattering [2,3]. These three scattering effects are discussed as follows.

## 2.2.1 The Coulomb Scattering Effect

There are different types of Coulomb scattering centers that can affect the carrier mobility in the inversion layer. The role of these Coulomb centers can be described as follows

### 2.2.1.1 The Ionized Impurity Scattering

An ionized impurity center in the lattice of a semiconductor produces a long-range Coulomb field with a potential energy  $U$ , given by  $U = q^2/(4\pi\epsilon r)$ , where  $\epsilon$  is the permittivity of the medium and  $r$  is the radial distance between the electron and the Coulomb center. The motion of a carrier in such a field is in many respects similar to the analogous problem of Rutherford scattering of charged particles by ionized nuclei [18]. As shown by Takagi *et al.* [2], the effective mobility of electrons decreases with an increase in the substrate doping density. Hence, the ionized impurity scattering increases with an increasing doping density.

### 2.2.1.2 The Remote Charge Scattering (RCS)

The aggressive scaling down of MOSFETs is quickly approaching the deep submicron regime. For sub-100 nm devices, an equivalent  $\text{SiO}_2$  thickness of less than 2 nm will be required, according to the National Technological Roadmap for Semiconductors (NTRS) [19]. This is due to the fact that, as the dielectric constant of  $\text{SiO}_2$  is low ( $\approx 3.9$ ), one has to scale down the oxide thickness in order to boost the oxide capacitance value (since the conductance of devices in analog circuits is proportional to the oxide capacitance). However, the serious disadvantages of the ultrathin oxides are

- 1) Since  $\text{SiO}_2$  is covalent in nature, the dopant atoms from the heavily doped poly gate can easily diffuse through the dielectric to the semiconductor layer, and, hence, can alter the doping concentration of the MOSFET channels.
- 2) The gate leakage current (due to the direct tunneling of electron from the gate to the channel) can change the normal current voltage characteristics of the device [20].

Recently, alternative gate dielectrics (e.g.,  $\text{Ta}_2\text{O}_5$ ,  $\text{Si}_3\text{N}_4$ ,  $\text{Al}_2\text{O}_3$ , etc., [19]) have demanded extensive attention, since they are expected to combine with (or even replace)  $\text{SiO}_2$  in order to reduce the problems mentioned above. These alternative gate oxides have the following properties.

- Since these materials have high values of permittivity ( $\epsilon$ ), hence, a higher value of oxide capacitance per unit area ( $C'_{\text{ox}}$ ) can be obtained with a relatively high value of oxide thickness ( $t_{\text{ox}}$ ), and, obviously, the gate tunneling leakage current would reduce for a thicker dielectric.
- Most of these alternative gate oxides are ionic in nature, and, hence, the dopant atoms can not easily diffuse through it.

Therefore, as suggested by Momose *et al.* [20], the development of high- $\epsilon$  gate insulators for MOSFETs is important as a future replacement of ultrathin  $\text{SiO}_2$ . Another disadvantage of ultrathin gate oxides is that the Coulomb scattering effect from remote charges in the poly gate (i.e., the ionized atoms which are introduced in the poly gate in order to make it conductive) or from poly gate/oxide interface roughness may lead to mobility degradation of channel electrons in MOSFETs having ultrathin gate oxides. The RCS effect on the effective mobility of the

inversion layer electrons may not be significant for higher oxide thicknesses ( $> 3$  nm or so) or even for the alternative gate oxides, since the distance between the inversion layer electrons and the remote charges on the poly gate becomes too large for these cases to initiate the RCS effects.

Besides the substrate impurities and the remote poly gate charges, the interface state charges and the charges trapped in the  $\text{SiO}_2$  layer can also act as Coulomb centers, and take part in the Coulomb scattering event. It is shown that [2], when the substrate impurity concentration ( $N_A$ ) is greater than  $5 \times 10^{16} \text{ cm}^{-3}$ , the Coulomb scattering is dominated by the ionized impurity scattering and  $\mu_c$  becomes inversely proportional to  $N_A$ . However, when  $N_A$  is less than  $5 \times 10^{16} \text{ cm}^{-3}$ , other Coulomb centers determine the mobility degradation due to Coulomb scattering.

### 2.2.2 The Phonon Scattering Effect

The scattering of the inversion layer electrons by the vibration of the lattice atoms is known as the lattice scattering or the phonon scattering. In a semiconductor device, there exist two systems: one is the electron system and the other is the lattice system. The energy gained by the electron system from the applied electric field is transferred to the lattice system via the emission of phonons. There are two types of phonons: the acoustic phonon and the optical phonon. The dispersion characteristics of these phonons are shown in Fig.2.1. (The energy versus momentum characteristics of these phonons will be similar to their dispersion characteristics, since the former can be found by multiplying the ordinate and abscissa of the later characteristics with  $h$  and  $\hbar$  respectively). From this figure, it can be noticed that the energy of the optical phonon is larger than that of the acoustic phonon, however, the variation of this energy (contrary to the acoustic phonons) is very little with the momentum change [21]. Under



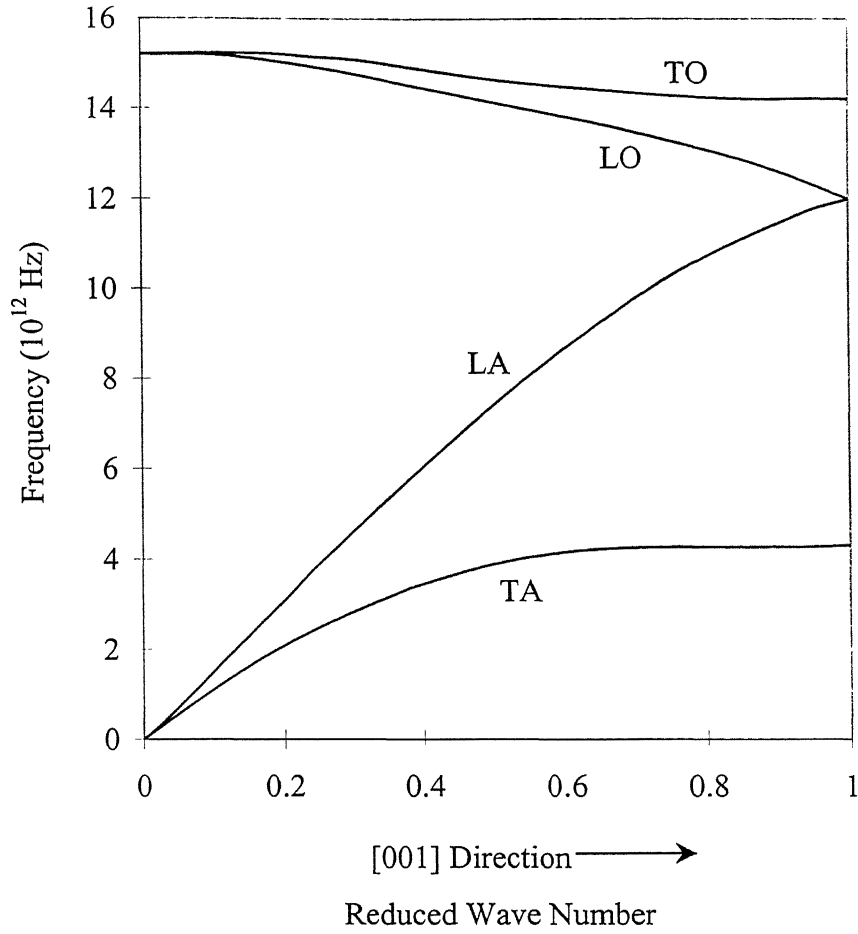


**FIGURE 2.1 :** Measured phonon spectra in silicon as a function of the wave vector along the [001] direction. The legends TO, LO, TA, and LA stand for transverse optical mode, longitudinal optical mode, transverse acoustic mode, and longitudinal acoustic mode respectively (after Sze [21]).

low electric fields, the emission of low energy acoustic phonons is responsible for lattice scattering and under large electric fields, the lattice scattering is due to the high energy optical phonons, since these optical phonons are not excited in thermal equilibrium due to the large amount of energy required for this process to happen. However, at very high electric fields, the carriers will gain enough energy between successive collisions in order to excite optical phonons. This process of emission of optical phonons sets an upper limit on the energy which a carrier can gain, since during optical phonon emission, a small change of energy requires a large change in the momentum. Because of this energy limitation, the drift velocity tends towards saturation, and, consequently, the effective mobility decreases [18,22]. However, this lattice scattering effect is more important for the heterojunction (e.g., GaAs-AlGaAs) MESFETs than Si-MOSFETs.

### **2.2.3. The Surface Roughness Scattering Effect**

At the Si-SiO<sub>2</sub> interface, the periodicity of the lattice ceases to exist, and various foreign materials (which may come from contaminations during the fabrication process) may get attached to the surface. As a consequence, the number of intermediate levels within the forbidden band gap at the insulator-semiconductor interface will increase sharply, and the recombination rate can be greatly increased. In a practical MOS structure, there exist four types of surface states or charges, which can trap electrons from the inversion layer [21]. These are

- 1) the surface states or the interface states, which are defined as the energy levels within the band gap at the Si-SiO<sub>2</sub> surface, and which can exchange charges with the semiconductor in a short time,

- 2) the fixed surface charges, which are located near or at the semiconductor surface and are immobile under applied electric fields,
- 3) the mobile ions, such as sodium, potassium, etc., which are mobile within the insulator layer under the bias temperature stress conditions, and
- 4) the ionized traps, which can be created, for example, by X-ray radiation.

Since the number of carriers recombining at a surface will be dependent on the area rather than the volume, it is convenient to define a recombination rate per unit area in the following way

$$r_{sr} = s\hat{n}_s \quad \text{or} \quad r_{sr} = s\hat{p}_s, \quad (2.6)$$

where  $r_{sr}$  is expressed in carriers recombining per unit area per second, and  $s$  is called the surface recombination velocity (a measure of the “quality” of the surface) [18]. Equation (2.6) is equivalent to saying that the excess carrier concentrations  $\hat{n}$  and  $\hat{p}$  are moving towards the surface with a velocity  $s$ , i.e., there is a diffusion of excess carriers towards the surface where they disappear by recombination. Therefore, the higher rate of recombination at a surface reduces the average surface lifetime, which is anyway lower than the bulk lifetime. As a matter of fact, when the current flows near the surface, the scattering due to surface recombination can be extremely important. As the gate voltage increases, the electrons are attracted more and more towards the Si-SiO<sub>2</sub> interface, and the surface roughness scattering becomes more dominant.

## 2.3 The Screening Effect

The screening effect is an important phenomenon, which controls the mobility of the inversion layer electrons in the moderate inversion region. To understand this phenomenon, let

us consider a point charge  $q$  placed in a medium with permittivity  $\epsilon$ . Then, the Coulomb potential  $\varphi_0(r)$  at a distance  $r$  from the point charge can be expressed as

$$\varphi_0(r) = \frac{q}{4\pi\epsilon r}. \quad (2.7)$$

Now, if the same point charge is placed in a sea of conduction electrons having a concentration of  $n_0$ , then the expression for the modified Coulomb potential  $\varphi(r)$  can be given by [23-25]

$$\varphi(r) = \frac{q}{4\pi\epsilon r} \exp(-k_s r), \quad (2.8)$$

where  $k_s$ , which is given by the relation  $k_s^2 = 4(3/\pi)^{1/3} n_0^{1/3} / a_0$  (here  $a_0$  is known as the Bohr radius), is known as the screening parameter and has the unit of  $\text{cm}^{-1}$ . The potential  $\varphi_0(r)$  is known as the unscreened potential and  $\varphi(r)$  is known as the screened potential. The screened and the unscreened potentials, which are given by Eqs.(2.7) and (2.8) respectively, are schematically plotted as a function of the radial distance in Fig.2.2. As can be seen from this figure, the screened Coulomb potential ( $\varphi(r)$ ) behaves similar to the unscreened Coulomb potential ( $\varphi_0(r)$ ) in the vicinity of the atom, but falls off drastically for large values of  $r$  due to the screening of the charge by the electron cloud.

## 2.4 The Effective Mobility

Figure 2.3 shows the dependence of the electron mobility in the inversion channel on the effective electric field ( $E_{\text{eff}}$ ) at 300 K and 70 K for different values of the substrate doping

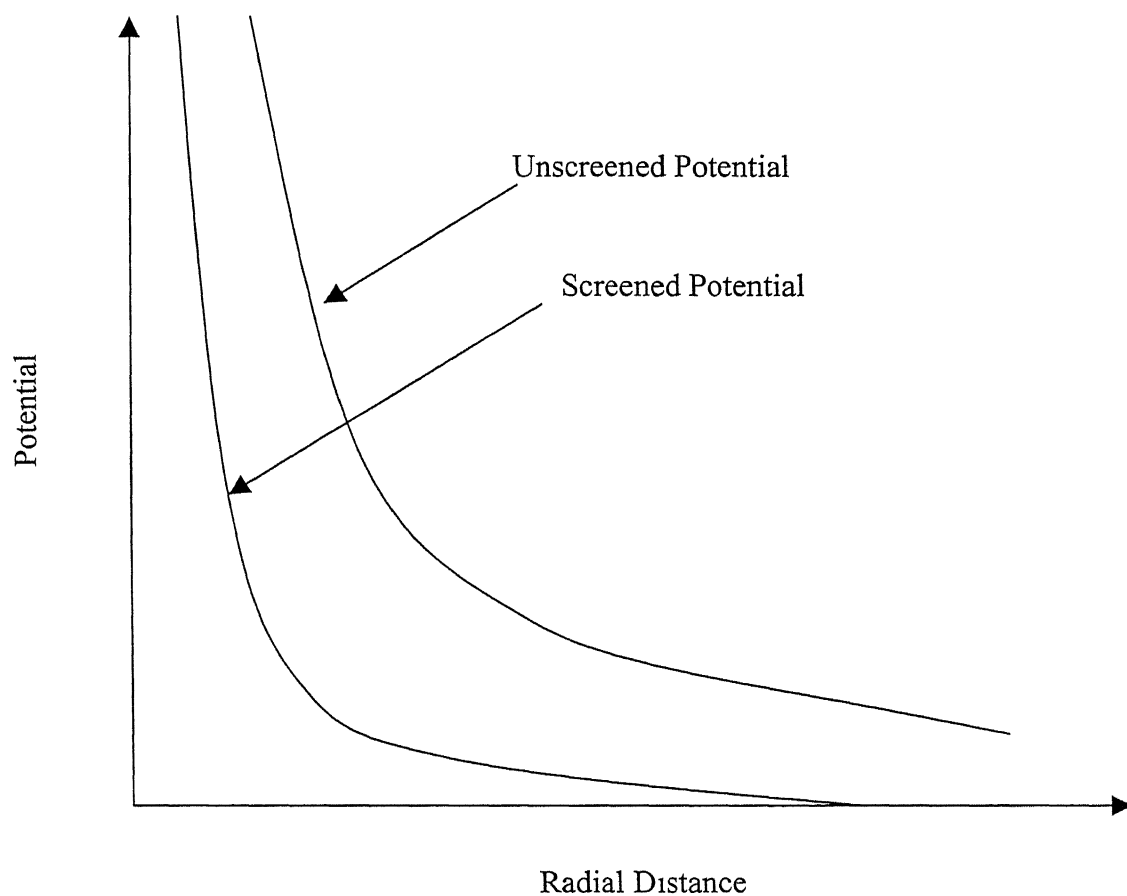


**FIGURE 2.2:** Schematic diagram for the comparison between the screened and the unscreened Coulomb potential of a static charge, as a function of the radial distance.

densities ( $N_A$ ), as reported by Takagi *et al.* [2], where  $E_{\text{eff}}$  in the inversion channel can be written as [2]

$$E_{\text{eff}} = \varepsilon_{\text{si}}^{-1}(\chi Q'_i + Q'_d), \quad (2.9)$$

where  $\varepsilon_{\text{si}}$  is the permittivity of silicon,  $Q'_i$  is the inversion charge density per unit area,  $Q'_d$  is the bulk (depletion) charge density per unit area, and  $\chi$  is a fitting parameter with typical values being 0.5 for (100) electrons and 0.33 for holes and electrons in (111) or (110) planes [2]. These experimental results confirm that the electron mobility follows the universal relationship with  $E_{\text{eff}}$  (which is given by the relation  $\mu_{\text{eff}} \propto E_{\text{eff}}^{-0.3}$  and  $\mu_{\text{eff}} \propto E_{\text{eff}}^{-2}$  at 300 K and 77 K respectively and are shown by dotted line in Fig.2.3) [2] for lower substrate doping densities, however, for higher substrate doping densities, it exhibits a significant deviation from the universal curve near the low field region or the moderate inversion region. The cause behind such deviation is believed to be due to the Coulomb scattering effect [2], which becomes more important when the doping concentration is high and the gate voltage or the normal field is low, since in the low field region,  $\mu_c$  is much lower as compared to  $\mu_{\text{sr}}$  or  $\mu_{\text{ph}}$ . There is less effect of the Coulomb scattering on mobility when the inversion charge density is high because of the charge screening effect, which has been discussed in the earlier paragraphs.

Figure 2.4 shows the dependence of the different mobility components on the effective field ( $E_{\text{eff}}$ ). According to this figure, the effective mobility characteristics can be broadly divided into three contributing terms, i.e., the phonon scattering term ( $\mu_{\text{ph}}$ ), the Coulomb scattering term ( $\mu_c$ ), and the surface scattering term ( $\mu_{\text{sr}}$ ). According to Matthiesian's rule [3], the effective nobility ( $\mu_{\text{eff}}$ ) is usually assumed to be related in a reciprocal manner to the individual contributions by these three mechanisms as [2,3]

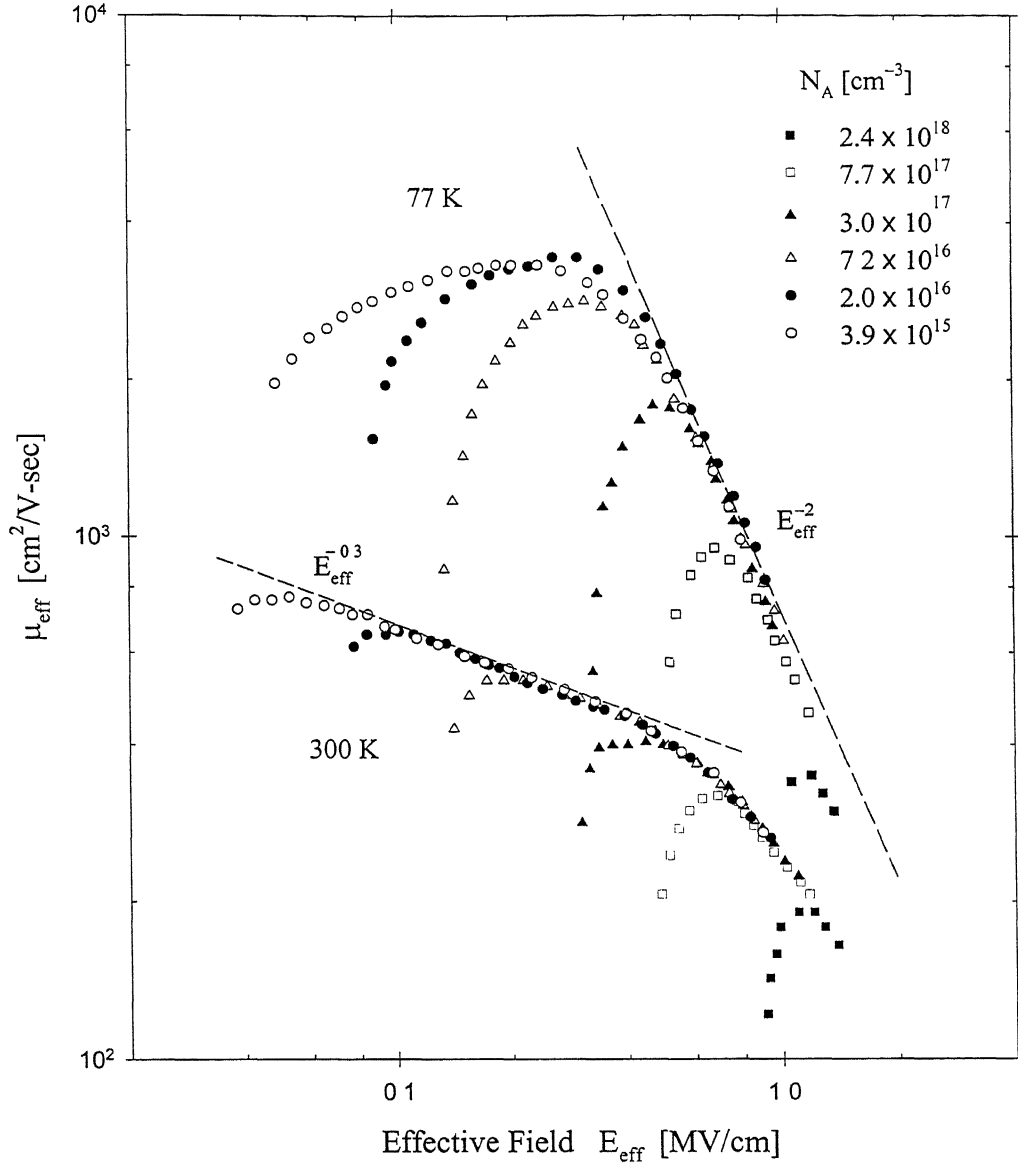


**FIGURE 2.3:** The effective electron mobility ( $\mu_{\text{eff}}$ ) at 300 K and 77 K in n-channel MOSFETs versus the effective normal field  $E_{\text{eff}}$ , for varying substrate acceptor concentrations ( $N_A$ ), as given by Takagi *et al.* [2].

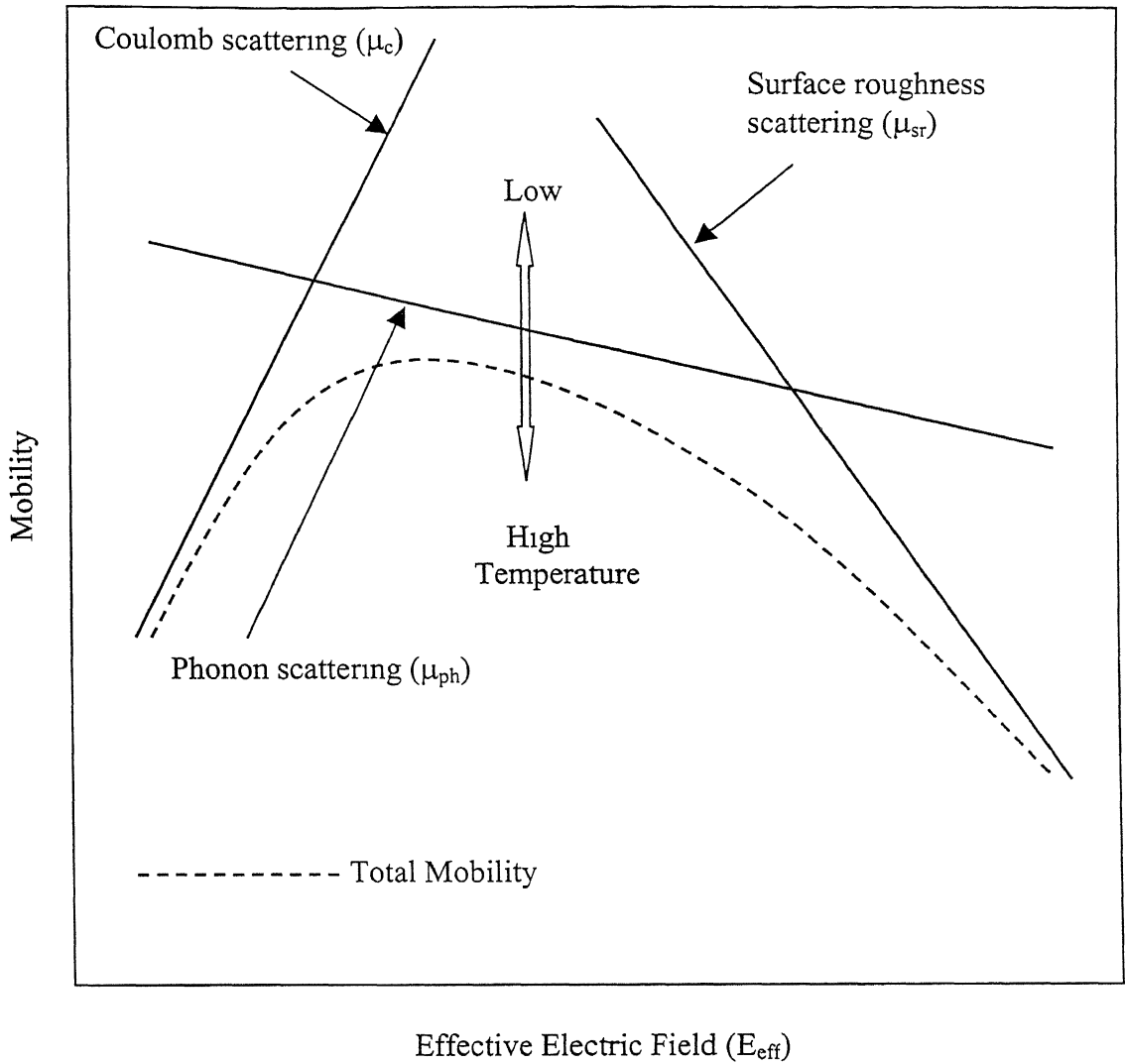


**FIGURE 2.4:** Schematic diagram of the effective electric field ( $E_{\text{eff}}$ ) dependence of the carrier mobility in the inversion layer by the three dominant scattering mechanisms, i.e., the phonon scattering ( $\mu_{\text{ph}}$ ), the surface roughness scattering ( $\mu_{\text{sr}}$ ), and the Coulomb scattering ( $\mu_c$ ), as given by Takagi *et al.* [2].



$$\frac{1}{\mu_{\text{eff}}} = \frac{1}{\mu_c} + \frac{1}{\mu_{\text{ph}}} + \frac{1}{\mu_{\text{sr}}} \quad (2.10)$$

When  $E_{\text{eff}}$  is low, i.e., the channel is in the moderate inversion region, the value of  $\mu_c$  is much lesser than either  $\mu_{\text{ph}}$  or  $\mu_{\text{sr}}$ . Hence, in this region, the effective mobility is determined mainly by the Coulomb scattering (i.e.,  $\mu_{\text{eff}} \approx \mu_c$ , since  $\mu_c \ll \mu_{\text{ph}}, \mu_{\text{sr}}$ ). A further study of this curve reveals that in this region, the Coulomb scattering term ( $\mu_c$ ), and, subsequently, the effective mobility ( $\mu_{\text{eff}}$ ) increases with an increase in the effective electric field  $E_{\text{eff}}$  (i.e., with the gate voltage). In Fig.2.5, the mobility variation due to the Coulomb scattering effect has been plotted as a function of the inversion layer electron density ( $N'_i$ ) for different values of the substrate doping density ( $N_A$ ). From Fig.2.5, it can be seen that the mobility due to the Coulomb scattering term ( $\mu_c$ ) increases almost linearly with the inversion layer electron density ( $N'_i$ ) and decreases with substrate doping density ( $N_A$ ). This phenomenon is due to the screening effect of the electrons in the inversion layer [2,26], which has been discussed in Section 2.3.

As stated previously, in a MOS structure, there are many charge centers located near the Si-SiO<sub>2</sub> interface, called the Coulomb charge centers, and they play important roles in carrier scattering. If the Coulomb centers near the interface are positively charged, then they attract electrons, and, in general, tie them up to a bound state. The properties of the bound states depend strongly on the amount of screening by the inversion layer electrons. At low temperatures, in the absence of screening, the bound states are deep enough to trap the first electrons that enter the inversion layer. As the gate voltage is increased, more and more electrons are added to the inversion layer, and some of these electrons will enter the quantum subband and will contribute to screening, thus weakening the scattering potential of the Coulomb centers. Alternatively, it

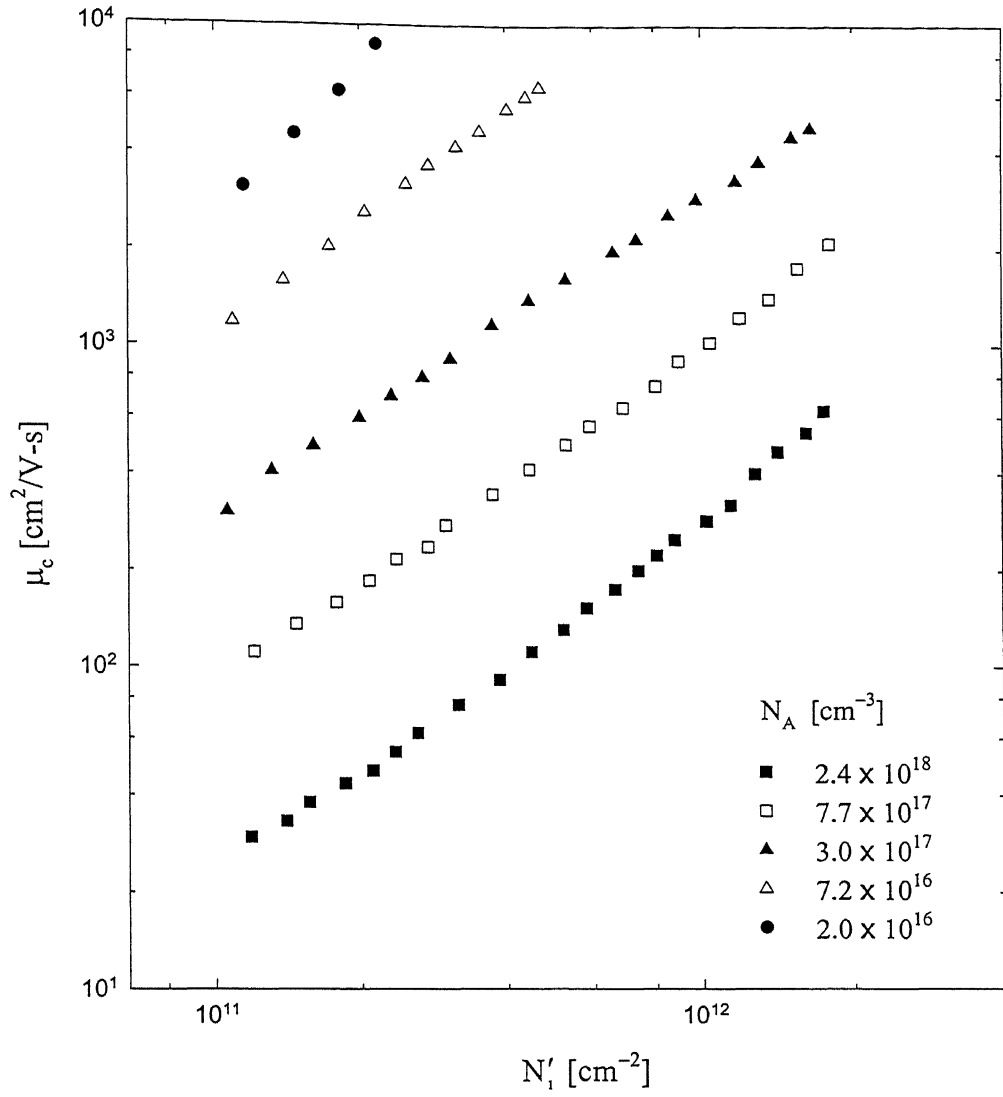


**FIGURE 2.5:** Inversion carrier density ( $N'_i$ ) dependence of  $\mu_c$  for n-channel MOSFETs with varying substrate impurity concentrations ( $N_A$ ), after Takagi *et al.* [2].

can be stated from Eq.(2.8) that, as the inversion layer electron concentration increases with increasing  $V_{GS}$ , the screening effect by the inversion layer electrons also increases. As a consequence, the scattering effect due to the Coulomb centers gets reduced and the effective mobility of the electron increases with the gate to source voltage ( $V_{GS}$ ) until the effect of the Coulomb scattering becomes comparable to that of the phonon scattering. With higher  $V_{GS}$  (i.e., when the channel is in the strong inversion region and the screening is too high due to the high electron density),  $\mu_c$  becomes very much larger than  $\mu_{ph}$  and  $\mu_{sr}$ . Hence, according to the Matthiesian's rule, it can be inferred that for high values of  $V_{GS}$ , the effect of the Coulomb scattering on  $\mu_{eff}$  becomes insignificant, and it is mainly determined by the phonon scattering ( $\mu_{ph}$ ) and the surface roughness scattering ( $\mu_{sr}$ ) effects.

## 2.5 The Threshold Voltage ( $V_T$ )

When a voltage  $V_G$  is applied to the gate of a MOSFET, part of it appears as a potential drop  $V_{ox}$  across the oxide and the rest appears as a band bending  $\Psi_s$  in silicon. It is straightforward to write that [7]

$$V_G = V_{ox} + \Psi_s = \frac{-Q'_s}{C'_{ox}} + \Psi_s, \quad (2.11)$$

where  $Q'_s$  is the total charge per unit area induced in silicon, and  $C'_{ox}$  is the oxide capacitance per unit area given by  $C'_{ox} (= \epsilon_{ox} / t_{ox})$  for an oxide thickness  $t_{ox}$ , and  $\epsilon_{ox} = \epsilon_0 \epsilon_{r(ox)}$ , where  $\epsilon_0$  is the permittivity of free space and  $\epsilon_{r(ox)}$  is the relative permittivity of  $SiO_2$ . There is a negative sign before  $Q'_s$  in Eq.(2.11) because the charge on the metal gate is always opposite in sign to the

charge in silicon, i.e.,  $Q'_s$  is negative when  $V_G$  is positive and vice versa. Now, if the work function difference is  $\phi_{ms}$  ( $= \phi_m - \phi_s$ , where  $\phi_m$  is the metal work function and  $\phi_s$  is the semiconductor work function), and the equivalent oxide charge per unit area at the oxide-silicon interface is  $Q'_{ox}$ , then the flat-band voltage ( $V_{FB}$ ) can be given by

$$V_{FB} = \phi_{ms} - \frac{Q'_{ox}}{C'_{ox}} . \quad (2.12)$$

Introducing the  $V_{FB}$  term in Eq.(2.11), it can be rewritten as

$$V_G = V_{FB} + \Psi_s - \frac{Q'_s}{C'_{ox}} . \quad (2.13)$$

The term  $Q'_s$  has two components, one is the depletion charge density per unit area ( $Q'_d$ ) and the other is the inversion charge density per unit area ( $Q'_i$ ). These can be modeled by the following equations [7]

$$Q'_d = -\sqrt{2\epsilon_{si}qN_A\Psi_s} , \text{ and} \quad (2.14)$$

$$Q'_i = \sqrt{\frac{2\epsilon_{si}kTn_i^2}{N_A}} e^{q\Psi_s/2kT} . \quad (2.15)$$

Here  $N_A$  is the acceptor doping density in the substrate,  $q$  is the electronic charge,  $n_i$  is the intrinsic carrier concentration for Si,  $k$  is the Boltzmann constant,  $T$  is the temperature (in K), and  $\epsilon_{si}$  is the permittivity of silicon. Equation (2.13) allows us to calculate the threshold gate voltage ( $V_T$ ). It is assumed that at  $V_G = V_T$ , the surface potential ( $\Psi_s$ ) is pinned at a value equal to  $\phi_B$ , and there is no further change in  $\Psi_s$  with an increase of  $V_G$ . At this surface potential, the

charge of free carriers induced at the insulator-semiconductor interface is still small compared to the charge in the depletion layer (i.e.,  $Q'_d \gg Q'_i$ ). Therefore, using Eqs.(2.13) and (2.14), the expression for  $V_T$  can be formulated as follows

$$V_T = V_{FB} + \phi_B + \frac{\sqrt{2\epsilon_{si}qN_A\phi_B}}{C'_{ox}} . \quad (2.16)$$

Different theories have been proposed in the literature in order to model  $\phi_B$  for an accurate extraction of  $V_T$ , and some of these are listed below.

1. The most conventional definition states that the threshold voltage occurs when  $\phi_B = 2\phi_F$ , where  $\phi_F$  is the bulk potential, given by

$$\phi_F = v_{th} \ln\left(\frac{N_A}{n_i}\right) . \quad (2.17)$$

Here  $v_{th}$  is the thermal voltage, defined as  $v_{th} = (kT/q)$ . At this point, the surface becomes as strongly n-type as the bulk is p-type

2. According to Tsividis [11], the surface potential ( $\Psi_s$ ) actually increases with  $V_G$  beyond the value of  $2\phi_F$ , however, the rate of this increase is much slower than that in the subthreshold regime (i.e., for  $\Psi_s < 2\phi_F$ ). According to this theory [11], the surface potential  $\Psi_s$  saturates at a value equal to  $2\phi_F + (4\sim 5)v_{th}$ . At this value of  $\Psi_s$ , the channel becomes strongly inverted. From this theory,  $\phi_B$  can be modeled as follows

$$\phi_B \approx 2\phi_F + (4\sim 5)v_{th} . \quad (2.18)$$

3. Recently, a new theory has been proposed by Conde *et al.* [8]. They have considered both the inversion and the depletion charge densities in order to calculate the threshold voltage. According to their theory,  $\phi_B$  can be formulated by the following equation

$$\phi_B = 2\phi_F + v_{th} \ln \left( \frac{2\phi_F}{v_{th}\zeta} \right) . \quad (2.19)$$

Here  $\zeta$  is a fitting parameter. With the help of a 2-D device simulator (MICROTEC [8]), it has been demonstrated that using  $\zeta = 10$  yields the closest agreement of the results obtained from this theory with the majority of the threshold voltage data obtained from the various extraction methods [9,10,12-14] for a wide range of substrate doping densities. With  $\zeta = 10$  and using standard values of substrate doping densities give  $\phi_B \approx 2\phi_F + 0.98v_{th}$ . Therefore, it seems that this threshold voltage model gives an average value of the threshold voltage, which is somewhere in between the ‘onset of the moderate inversion’ and the ‘onset of the strong inversion’ regions, as per Tsividis [11].

## 2.6 The Drain Current Model

To compute the drain current  $I_D$ , it is convenient to adopt the ‘regional’ approach, where the various operating regions of MOSFETs are identified by the values of the gate to source voltage ( $V_{GS}$ ) or by the surface potential ( $\Psi_s$ ), as discussed below.

### 2.6.1. The Drain Current Model in the Subthreshold Region

The subthreshold region, by definition, is the operating region of the MOSFET, where  $0 < \Psi_s < 2\phi_F$ . In this region, the drain current is entirely diffusive in nature (i.e., it is primarily

contributed by the diffusion of electrons from the source to the channel). This subthreshold component of the drain current ( $I_{\text{sub}}$ ) can be modeled in the following way [11]

$$I_{\text{sub}} = \frac{W}{L} \mu_n \frac{\gamma C'_{\text{ox}}}{2\sqrt{1.5\phi_F + V_{\text{SB}} - v_{\text{th}}}} v_{\text{th}}^2 e^{0.5\phi_F / v_{\text{th}}} e^{(V_{\text{GS}} - V_T) / \eta v_{\text{th}}} (1 - e^{-V_{\text{DS}} / v_{\text{th}}}), \quad (2.20)$$

where  $\gamma$  is the body effect coefficient, given by  $\gamma = \frac{\sqrt{2q\epsilon_{\text{si}} N_A}}{C'_{\text{ox}}}$ , and  $\eta$  is an ideality factor,

defined by  $\eta = 1 + \frac{\gamma}{2\sqrt{1.5\phi_F + V_{\text{SB}}}}$ . Here  $\mu_n$  is the effective mobility of the electrons (in

$\text{cm}^2/\text{V}\cdot\text{sec}$ ) in the subthreshold region,  $V_{\text{SB}}$  is the source to substrate voltage, and  $V_{\text{DS}}$  is the drain to source voltage. Now for any  $V_{\text{DS}}$ ,  $I_{\text{sub}}$  can be simplified to

$$I_{\text{sub}} = I_0 \exp\left(\frac{V_{\text{GS}} - V_T}{\eta v_{\text{th}}}\right), \quad (2.21)$$

where  $I_0$ , which is independent of  $V_{\text{GS}}$ , can be expressed as

$$I_0 = \frac{W}{L} \mu_n \frac{\gamma C'_{\text{ox}}}{2\sqrt{1.5\phi_F + V_{\text{SB}} - v_{\text{th}}}} v_{\text{th}}^2 e^{0.5\phi_F / v_{\text{th}}} (1 - e^{-V_{\text{DS}} / v_{\text{th}}}). \quad (2.22)$$

## 2.6.2 The Drain Current Model in the Strong Inversion Region

The operating region of MOSFETs, where  $V_{\text{GS}} > V_T$  is defined as the strong inversion region, where the surface potential is pinned at a value equal to  $2\phi_F + (4\sim 5)v_{\text{th}}$ . In this region, the drift process contributes primarily to the current conduction. This strong inversion component of the drain current ( $I_{\text{inv}}$ ) can be modeled with the help of BSIM [6] in the following way

$$I_{inv} = \frac{W}{L} C'_{ox} \mu_{eff} \left( (V_{GS} - V_T) V_{DS} - \frac{V_{DS}^2}{2} \right) \quad \text{for } (V_{GS} - V_T) \geq V_{DS}, \quad (2.23)$$

and

$$I_{inv} = \frac{W}{2L} C'_{ox} \mu_{eff} (V_{GS} - V_T)^2 (1 + \lambda V_{DS}) \quad \text{for } (V_{GS} - V_T) < V_{DS}. \quad (2.24)$$

Here  $\mu_{eff}$  is the effective mobility of the carriers in the channel, given by [6]

$$\mu_{eff} = \frac{\mu_0}{1 + \theta(V_{GS} - V_T)}, \quad (2.25)$$

where  $\mu_0$  is the low field mobility and  $\theta$  (in  $V^{-1}$ ) is the mobility degradation coefficient. The parameter  $\lambda$  (in  $V^{-1}$ ) is known as the channel length modulation parameter. Here the velocity saturation co-efficient ( $U_1$ ), which was proposed in BSIM, is omitted for the sake of simplicity. Now, for low values of  $V_{DS}$  and  $V_{GS}$ , one can neglect the  $V_{DS}^2$  and the  $\theta(V_{GS} - V_T)$  terms in Eqs.(2.23) and (2.25) respectively. Thus, under these conditions, Eq.(2.23) can be rewritten in the following way

$$I_{inv} = K(V_{GS} - V_T)V_{DS}, \quad (2.26)$$

where  $K$  (in  $A/V^2$ ) is known as the device transconductance parameter and is given by

$$K = \frac{W}{L} C'_{ox} \mu_0.$$



# Development of the Mobility Model

---

In this chapter, a new mobility model for short channel MOSFETs has been developed, which is based primarily on the BSIM mobility model. The Coulomb scattering effect at low electric field has been considered in this new model in order to apply it in the moderate inversion region.

## 3.1 The Definition of the Threshold Voltage

Today the world of IC devices has become broadly divided into two categories: one belonging to the analog devices and the other to the digital devices. The topologies, challenges, and the design techniques of these two types of devices are completely different. For most digital IC operations, the MOSFET devices act as electronic switches, which can either be in the ON state or in the OFF state. Therefore, for digital IC simulation and characterization, an accurate modeling of the moderate inversion region and the subthreshold region is not that important. These regions are only studied in order to measure the OFF state current of the digital IC devices. Therefore, for digital IC design and simulation, the definition of the threshold voltage ( $V_T$ ) should be such that it represents the ‘onset of the strong inversion region’ (i.e.,  $V_{TS}$ ), such

that when  $V_{GS}$  becomes greater than  $V_{TS}$ , the device is assumed to be strongly turned ON, otherwise it is OFF.

On the other hand, as analog VLSI gains popularity, designers are trying to bias the devices in the moderate inversion region in order to reduce the power dissipation. An immediate consequence is that the threshold voltage is becoming the most important parameter for analog IC design, simulation, and characterization. In analog ICs, the MOSFET devices act as variable resistances (contrary to the electronic switches for digital ICs). Therefore, an accurate modeling of the moderate inversion region is extremely important for devices in analog IC applications. For a proper modeling of the moderate inversion region, the definition of the threshold voltage should be such that it represents the ‘onset of the moderate inversion region’ (i.e.,  $V_{TM}$ ).

Figure 3.1 shows the schematic diagram of the surface potential  $\Psi_s$  versus the gate to source voltage  $V_{GS}$  characteristic for a typical MOSFET device. As per Tsividis[11], the characteristic can be divided into three major regions:

- 1) The weak inversion region (for  $V_L < V_{GS} < V_{TM}$ ; where  $V_{GS} = V_L$  when  $\Psi_s = \phi_F$ ): In this region,  $\Psi_s$  increases from  $\phi_F$  to  $2\phi_F + \Delta\phi$  almost linearly with respect to  $V_{GS}$ . The value of  $\Delta\phi$  (which is discussed in detail in Chapter 6) is a few millivolts.
- 2) The moderate inversion region (for  $V_{TM} < V_{GS} < V_{TS}$ ): In this region,  $\Psi_s$  varies between  $2\phi_F + \Delta\phi$  to  $2\phi_F + (4\sim 5)V_{th}$  in a nonlinear fashion with respect to  $V_{GS}$ .

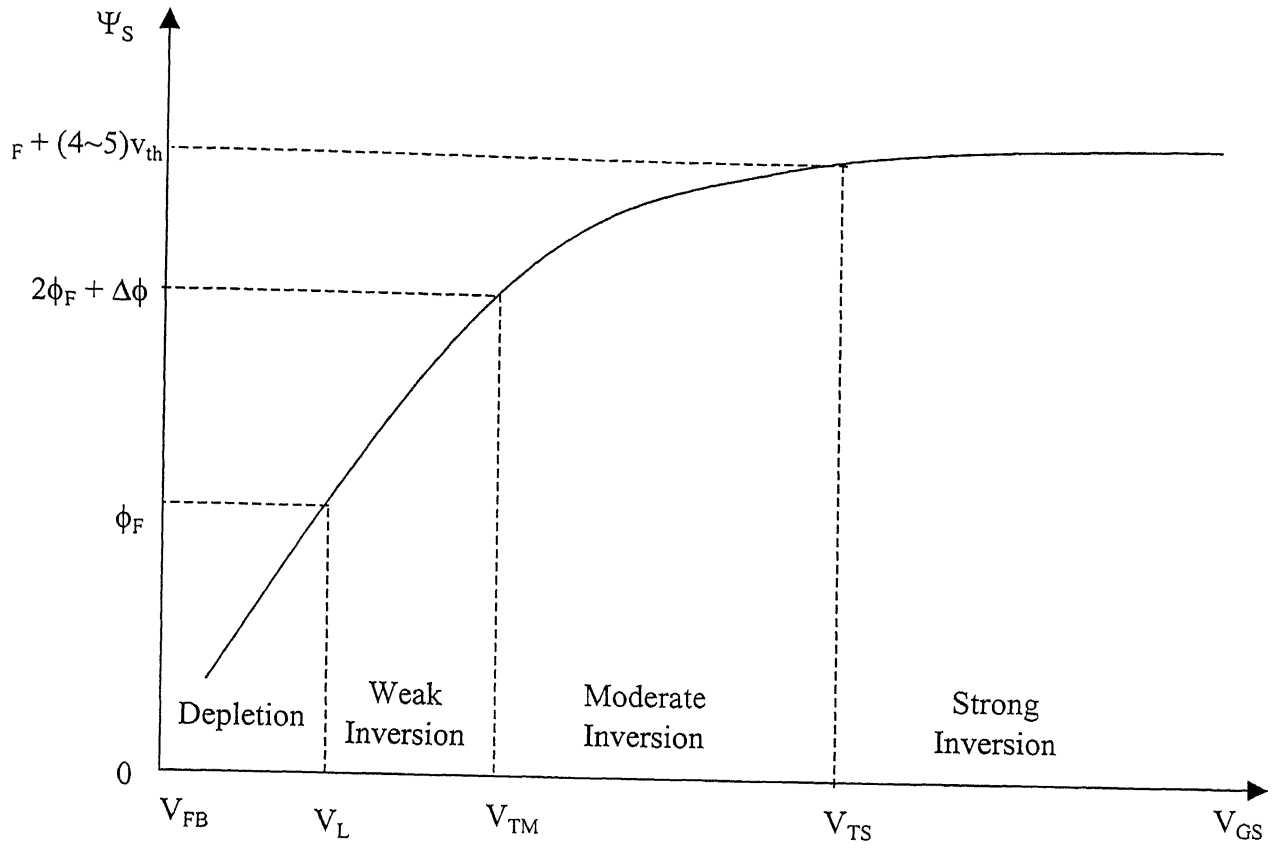


**FIGURE 3.1** : Schematic diagram of the variation of the surface potential  $\Psi_S$  with respect to the gate-to-source voltage  $V_{GS}$  for a typical MOSFET device, as presented by Tsividis [11].

- 3) The strong inversion region (for  $V_{TS} < V_{GS}$ ): In this region,  $\Psi_s$  becomes almost pegged at a value equal to  $2\phi_F + (4\sim 5)v_{th}$  and does not show any significant change with any further increase in  $V_{GS}$ .

To date, several drain current models [6,27] have been proposed in the literature in order to explain the MOSFET drain current characteristics. In these models, the threshold voltage parameter ( $V_T$ ) acts as the boundary between the strong inversion and the weak inversion regions. Then effort has been made in order to find proper models for the strong inversion and the weak inversion components of the drain current. Afterwards, these two components have been joined using different types of smoothing functions [27] or by some interpolation techniques [28] in order to obtain the overall drain current model. However, these techniques are quite inadequate to model the moderate inversion region accurately due to the following facts.

- 1) These models use the value of the threshold voltage, which is neither  $V_{TM}$  nor  $V_{TS}$ , but an average of the two, and they only rely on the smoothing functions for the modeling of the moderate inversion region.
- 2) These models use the BSIM mobility model, which does not consider the Coulomb scattering effect, and, hence, is inapplicable in the moderate inversion region.

Therefore, these drain current models are more suitable for modeling devices in digital IC applications rather than for the analog IC ones. For analog IC design, in order to accurately model the moderate inversion region, one has to not only take  $V_{TM}$  as the threshold voltage, but also use a modified expression for the mobility in order to account for the Coulomb scattering effect. In conclusion, it can be stated that for digital and analog IC designs, designers have to

switch between two different threshold voltage ( $V_{TS}$  and  $V_{TM}$ ) and two different mobility models.

## 3.2 Development of the Modified Drain Current Model

The BSIM drain current model as discussed in Section 2.6 is based on the following two major approximations, which are not valid in the moderate inversion region.

- 1) It is based on the simple charge control model for the inversion charge density  $Q'_i$  [i.e.,  $Q'_i = C'_{ox}(V_{GS} - V_T)$ ], which obviously is not valid in the moderate inversion region, since  $\Psi_s$  is not a constant in this region, and also that the inversion charge density is not so high that one can neglect the depletion charge density in comparison with it.
- 2) The BSIM mobility model [as given by Eq.(2.26)] takes into account only the phonon scattering and the surface roughness scattering effects, however, it ignores the Coulomb scattering effect, which is *the* most important parameter for determining the effective mobility of electrons in the moderate inversion region.

Due to these two major approximations, the BSIM drain current model gives accurate results only when the device is biased in the strong inversion region, and fails in the moderate inversion region. Therefore, one has to modify the BSIM drain current model in order to apply it in the moderate inversion region. In this work, an effort has been made in proposing a new mobility model, so that the BSIM drain current model can be applied in the moderate inversion region without changing its basic form [i.e.,  $I_D = (W/L)C'_{ox} \mu_{eff}(V_{GS} - V_T)V_{DS}$ ], but only substituting the BSIM mobility model with the proposed mobility model and  $V_T$  with  $V_{TM}$

### 3.3 Modeling of the Inversion Charge

Generally, the inversion layer electron density  $N'_i$  is modeled as [7,9,11]

$$N'_i = \frac{C'_{ox}}{q} (V_{GS} - V_{TM}). \quad (3.1)$$

However, as presented by Hauser [3], this linear relationship between  $N'_i$  and  $V_{GS}$  does not quite hold good in the moderate inversion region and gives appreciable error, since in this region  $\Psi_s$  is not a constant but varies slowly with  $V_{GS}$ . In the weak inversion region, as  $\Psi_s$  varies almost linearly with  $V_{GS}$ , the inversion charge density increases exponentially with increasing  $V_{GS}$ . On the other hand, in the strong inversion region, as  $\Psi_s$  starts to saturate, the inversion charge density becomes a linear function of  $V_{GS}$ . Therefore, it can be stated that in the moderate inversion region, the variation of  $N'_i$  with respect to  $V_{GS}$  is neither exponential nor linear. In this work, a better formulation of  $N'_i$  in the moderate inversion region has been developed, which can be expressed as

$$N'_i = \xi \frac{C'_{ox}}{q} (V_{GS} - V_{TM})^{1.5}, \quad (3.2)$$

where  $\xi$  (in  $V^{-0.5}$ ) is a fitting parameter. The origin of this equation is semi-empirical. Physically it is obvious that the value of  $\partial N'_i / \partial V_{GS}$  in the moderate inversion region is greater than that in the strong inversion region, and smaller than that in the weak inversion region. One point must be noted here that, this model is valid only in the moderate inversion region, and in the strong inversion region  $N'_i$  follows the linear model [as given by Eq.(3.1)].

### 3.4 The Proposed Mobility Model

From the discussion of the previous chapter, it can be stated that in the moderate inversion region, the effective mobility of the inversion layer electrons is mainly determined by the Coulomb scattering effect ( $\mu_c$ ); and in the strong inversion region, it is primarily controlled by the phonon scattering effect ( $\mu_{ph}$ ) and the surface roughness scattering effect ( $\mu_{sr}$ ). From the work of Takagi *et al.* [2] and Manzini [4], it can also be stated that  $\mu_c$  varies linearly with the inversion layer electron density ( $N'_i$ ) in the moderate inversion region. Hence, it can be written that

$$\mu_c \propto N'_i \quad \text{or} \quad \mu_c \propto (V_{GS} - V_{TM})^{1.5} \quad (3.3)$$

Now, if one uses the term  $\mu_{phsr}$  in order to represent the phonon scattering and the surface roughness scattering effects, then with the help of the BSIM mobility model,  $\mu_{phsr}$  can be expressed as

$$\mu_{phsr} = \frac{\mu_0}{1 + \theta(V_{GS} - V_{TM})} \quad (3.4)$$

Now, the overall effective mobility ( $\mu_{eff}$ ) model of the inversion layer electrons should be such that it satisfies the following conditions

$$\begin{aligned} \mu_{eff} &\approx \mu_c && \text{for } V_{TM} < V_{GS} < V_{TS}, \text{ and} \\ \mu_{eff} &\approx \mu_{phsr} && \text{for } V_{GS} > V_{TS}. \end{aligned} \quad (3.5)$$

In order to obtain the overall mobility model, a new function  $U(V_{GS})$  is developed in this work, which is defined as

$$U(V_{GS}) = z \left[ y + \frac{M(V_{GS} - V_{TM})^{1.5}}{M + (V_{GS} - V_{TM})^{1.5}} \right], \quad (3.6)$$

where  $M$  and  $y$  are two fitting parameters having units of  $V^{1.5}$  and  $z$  is another fitting parameter having the unit of  $V^{-1.5}$ . The function  $U(V_{GS})$  has been plotted as a function of  $(V_{GS} - V_{TM})$  for four different values of  $M$  ( $0.05 V^{1.5}$ ,  $0.087 V^{1.5}$ ,  $0.1 V^{1.5}$ , and  $0.17 V^{1.5}$ ) in Fig.3.2. Now, for proper modeling of  $\mu_{eff}$ , the value of  $M$  has to be taken such that the second term in the square bracket of Eq.(3.6) approaches a constant value for  $V_{GS}$  greater than  $V_{TS}$ . This is due to the fact that the Coulomb scattering effect only dominates in the moderate inversion region. Generally, the difference between  $V_{TS}$  and  $V_{TM}$  (i.e., the region of the moderate inversion) is within 0.2 to 0.3 V. Therefore, typical values of  $M$  range from  $0.089 (= 0.2^{1.5})$  to  $0.165 (= 0.3^{1.5})$ . The values of the other two fitting parameters ( $z$  and  $y$ ) have to be chosen in such a manner that the value of the quantity  $z \times (y + M)$  tends to unity for  $V_{GS}$  greater than  $V_{TS}$ . Thus, the effective mobility model proposed in this work can be given as

$$\mu_{eff,proposed} = \frac{\mu_0 U(V_{GS})}{1 + \theta(V_{GS} - V_{TM})}. \quad (3.7)$$

From Eqs.(3.6) and (3.7) it can be seen that, in the moderate inversion region (i.e., for  $V_{TM} < V_{GS} < V_{TS}$ ), the variation of the  $[1 + \theta(V_{GS} - V_{TM})]$  term is quite small as compared to the variation of the  $U(V_{GS})$  function, since typical values of  $\theta$  lie between 0.6 and  $0.8 V^{-1}$ . Therefore, in the moderate inversion region, the effective mobility ( $\mu_{eff}$ ) increases with increasing  $V_{GS}$ . For  $V_{GS} >$



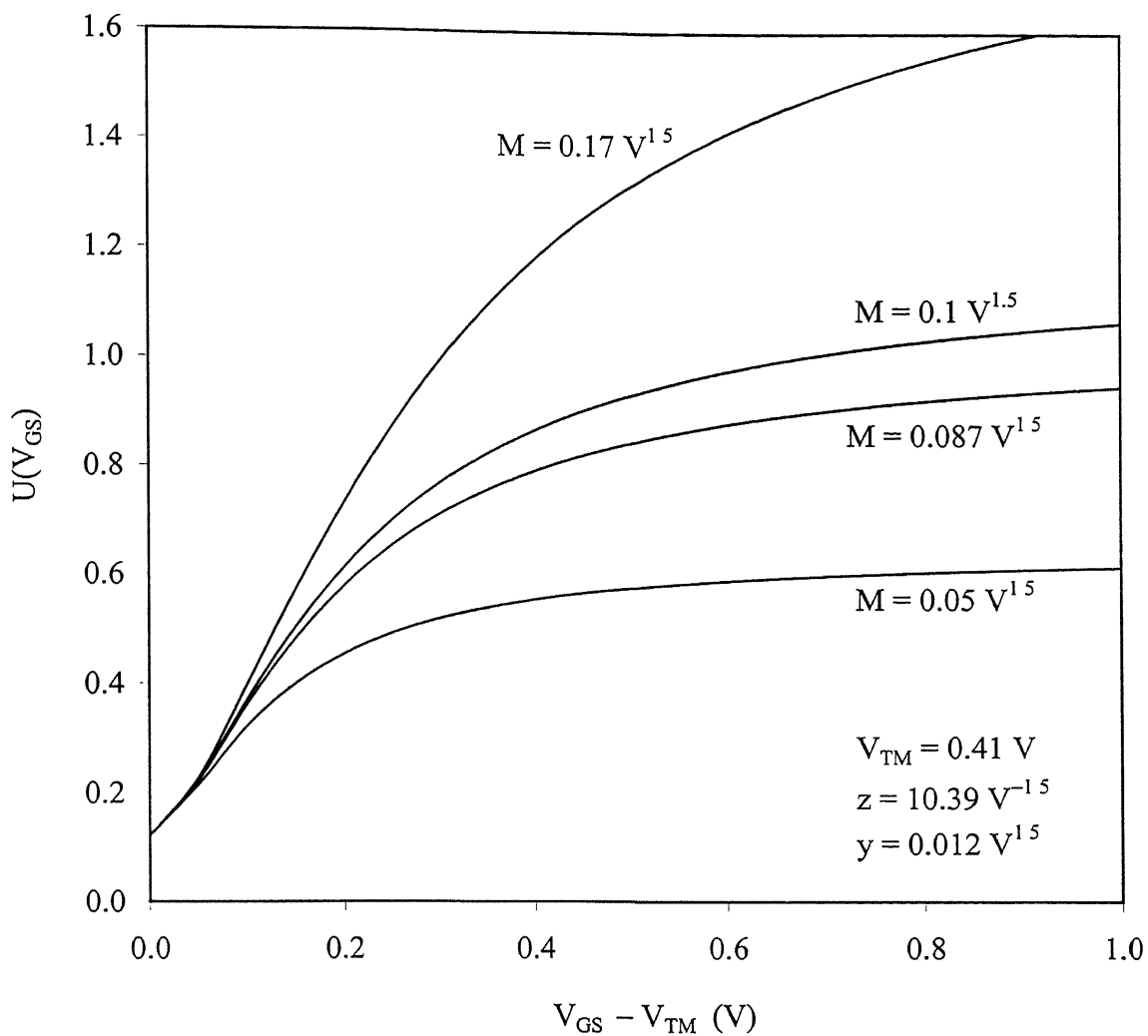


**FIGURE 3.2 :** Plots of  $U(V_{GS})$  versus  $V_{GS} - V_{TM}$  for four values of  $M$ .

$V_{TS}$ , the function  $U(V_{GS})$  tends to attain a constant value of unity, and the proposed mobility model shows a similar behavior as the well-known BSIM mobility model. Hence, it can be stated that the proposed mobility model incorporates the Coulomb scattering effect in the moderate inversion region, which is absent in the BSIM mobility model, and, therefore, the proposed model seems to be more reliable, accurate, and robust than the BSIM mobility model for modeling devices to be used in low power analog IC designs.

### 3.5 The Drain Current Model in the Moderate Inversion Region

In this section, an approximate drain current model applicable to the moderate inversion region is proposed, which can be very helpful for quick calculations of the drain current in the said region. Here, two new functions  $f(V_{GS})$  and  $h(V_{GS})$  have been introduced, which can be defined as

$$f(V_{GS}) = \zeta(V_{GS} - V_{TM})^{0.5}, \text{ and} \quad (3.8)$$

$$h(V_{GS}) = \frac{U(V_{GS})}{1 + \theta(V_{GS} - V_{TM})}, \quad (3.9)$$

where  $\zeta$  is a new fitting parameter having a unit of  $V^{-0.5}$ . For a set of typical values of  $z$ ,  $M$ ,  $y$ , and  $\theta$  (which will be discussed in detail in the next chapter), both  $h(V_{GS})$  and  $f(V_{GS})$  functions have been plotted as a function of  $(V_{GS} - V_{TM})$  in Fig.3.3 for three different values of  $\zeta$  ( $0.85 V^{-0.5}$ ,  $1.15 V^{-0.5}$ , and  $2 V^{-0.5}$ ). From this figure, it can be inferred that by a proper choice of the value of  $\zeta$ , the function  $h(V_{GS})$  can be made to approximate the function  $f(V_{GS})$  in the moderate

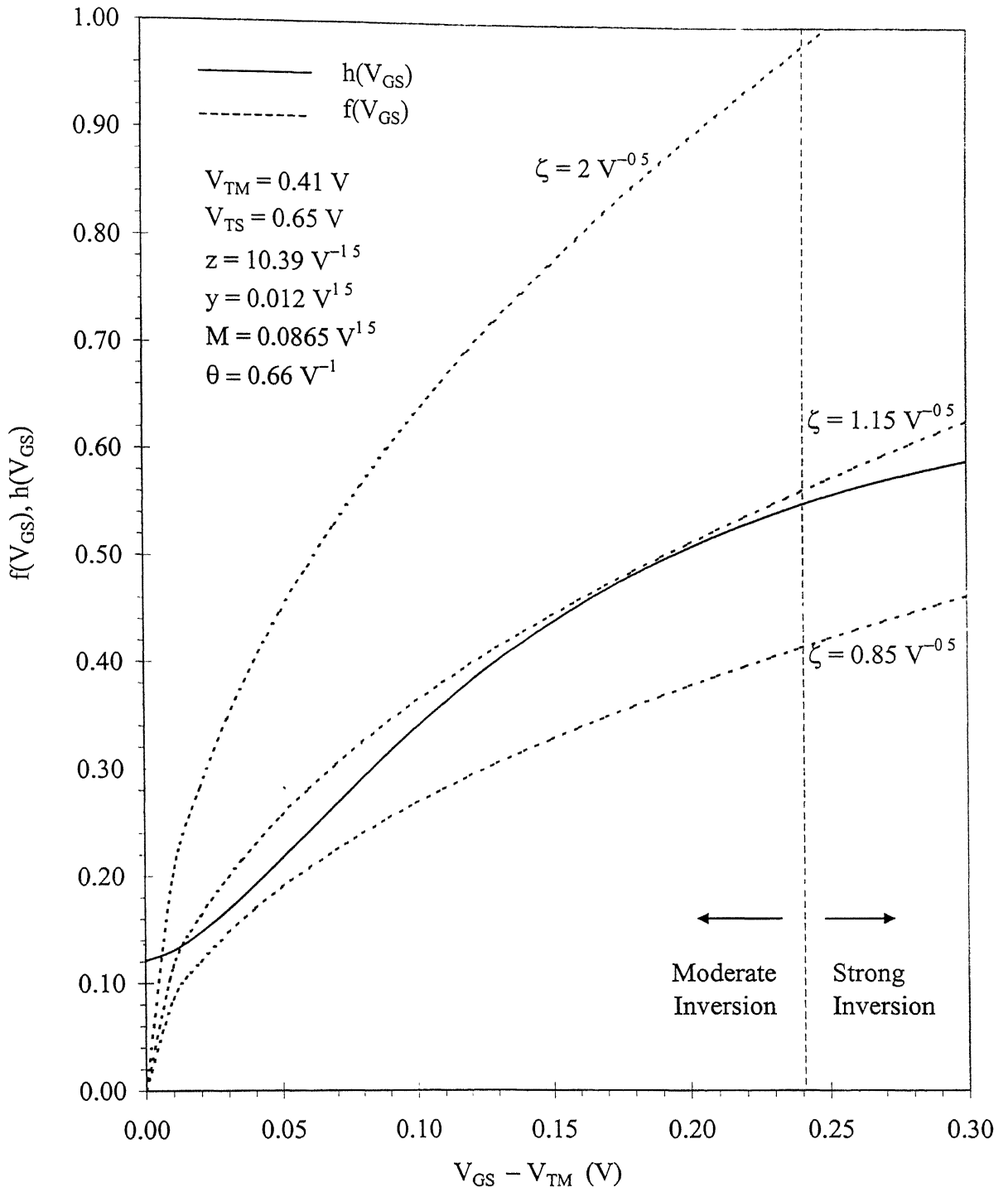


**FIGURE 3.3 :** Plots of the functions  $f(V_{GS})$  and  $h(V_{GS})$  as a function of  $V_{GS} - V_{TM}$  for three values of  $\zeta$ .

inversion region [i.e., for  $V_{TM} < V_{GS} < V_{TS}$ ,  $h(V_{GS}) \rightarrow f(V_{GS})$ ]. Thus, in this region, the proposed mobility model [Eq.(3.7)] can be approximated by

$$\mu_{\text{eff}} \approx \mu_0 \zeta (V_{GS} - V_{TM})^{0.5}. \quad (3.10)$$

This approximate mobility model is valid only in the moderate inversion region and loses its validity in the strong inversion region. Putting this expression of  $\mu_{\text{eff}}$  in Eq.(2.23) and neglecting the  $V_{DS}^2$  term for low values of  $V_{DS}$ , the approximate drain current equation in the moderate inversion region can be given by

$$I_{\text{inv}} = \frac{W}{L} C'_{\text{ox}} \mu_0 \zeta (V_{GS} - V_{TM})^{1.5} V_{DS}. \quad (3.11)$$

Similarly, this drain current model is also valid only in the moderate inversion region (i.e., for  $V_{TM} < V_{GS} < V_{TS}$ ), since the mobility model (as given by Eq.(3.10)) only considers the Coulomb scattering effect and ignores the phonon and the surface roughness scattering effects. Although this is a semi-empirical approximate model, it is very useful for the hand-calculation of drain current in the moderate inversion region. In the next chapter, the validity of this drain current model has been tested with the experimental data reported in the literature.

## Model Verification and Discussion

---

In this chapter, the proposed mobility model is verified with some recently reported measured data for short channel MOSFETs.

### 4.1 The Modified Drain Current Model

The total drain current ( $I_D$ ) can be expressed as the summation of the subthreshold component ( $I'_{sub}$ ) and the drift component ( $I'_{str}$ ). Hence, one can write

$$I_D = I'_{sub} + I'_{str} \quad (4.1)$$

Here, the subthreshold component  $I'_{sub}$  is defined by [6,27]

$$I'_{sub} = \frac{I_{sub} I_{sat}}{I_{sub} + I_{sat}}, \quad (4.2)$$

where  $I_{sub}$  can be given by

$$I_{sub} = I_0 \exp\left(\frac{V_{GS} - V_{TM}}{\eta V_{th}}\right). \quad (4.3)$$

In Eq.(4.2),  $I_{\text{sat}}$  is a new fitting parameter, which represents the saturated value of the subthreshold current in the strong inversion region, and its value can be extracted from the experimental data of the device. It is defined in order to remove the higher order discontinuity in the drain current equation at  $V_{\text{GS}} = V_{\text{TM}}$  [6,27]. By replacing all the  $(V_{\text{GS}} - V_{\text{T}})$  terms in Eqs.(2.23), (3.6), and (3.7) with a new function  $V_{\text{GTMX}}$  and neglecting the  $V_{\text{DS}}^2$  term for low values of  $V_{\text{DS}}$ , one can obtain the expression for the drift component  $I'_{\text{sr}}$  as

$$I'_{\text{sr}} = \frac{W}{L} C'_{\text{ox}} \mu_{\text{eff,proposed}} V_{\text{GTMX}} V_{\text{DS}}, \quad (4.4)$$

where the new function  $V_{\text{GTMX}}$  is defined as [27]

$$V_{\text{GTMX}} = s \ln \left( 1 + e^{\frac{V_{\text{GS}} - V_{\text{TM}}}{s}} \right), \quad (4.5)$$

where  $s$  is a fitting parameter having the unit of Volts. This function is defined in order to join the weak inversion and the strong inversion components of the drain current at  $V_{\text{TM}}$ , and also to ensure the continuity of the transconductance and its higher order derivatives. Thus, the overall drain current expression becomes

$$I_{\text{D}} = \frac{I_{\text{sat}} I_0 e^{\frac{V_{\text{GS}} - V_{\text{TM}}}{\eta V_{\text{th}}}}}{I_{\text{sat}} + I_0 e^{\frac{V_{\text{GS}} - V_{\text{TM}}}{\eta V_{\text{th}}}}} + \frac{W}{L} C'_{\text{ox}} \frac{\mu_0}{1 + \theta V_{\text{GTMX}}} \left[ z \left( y + \frac{M V_{\text{GTMX}}^{1.5}}{M + V_{\text{GTMX}}^{1.5}} \right) \right] V_{\text{GTMX}} V_{\text{DS}}. \quad (4.6)$$

The second term in the right hand side of the above equation can be approximated by Eq.(3.11) in the moderate inversion region.

## 4.2 Parameter Extraction

In order to apply the present model in circuit simulation, it is necessary to find a practical way of extracting the model parameters from the experimental data. The accuracy of the parameter extraction procedure depends on the accuracy of the model and on the accuracy and the completeness of the experimental data. Basically, there are two approaches for the extraction of the model parameters from the experimental data. In the first approach, special measurements are performed, from which the parameters can be extracted directly. This is termed as the analytical approach, and Tsividis [11] described such a procedure in detail. However, this approach becomes impractical when the number of parameters to be extracted increases. The second approach that is used for such cases is the numerical approach, which uses optimization techniques. In this approach, the model parameters are extracted from a given set of data using a nonlinear least-square optimizer, which curve fits the model to the experimental data using the controlling parameters as the variables.

In this work here, the nonlinear optimization method is used to extract the model parameters from the experimental data. The well-known GNUPLOT software [29] is used to carry on the nonlinear optimization procedure. For the experimental data, the  $I_D$ - $V_{GS}$  characteristics for a 0.26  $\mu\text{m}$  channel length n-MOSFET have been taken from the work reported by Langevelde and Klaassen [15]. These characteristics are measured at a constant low value of  $V_{DS}$  (50 mV), and  $V_{GS}$  is incremented from 0 V to 1.5 V in steps of 10 mV. The device has the following parameters: gate length (L) of 0.26  $\mu\text{m}$ , gate width (W) of 10  $\mu\text{m}$ , and oxide thickness ( $t_{ox}$ ) of 4.5 nm. The threshold voltage at the onset of the moderate inversion ( $V_{TM}$ ) is extracted by the method proposed in Section 6.1 of this work and it is found to be equal to 0.41 V. Then,

Eq.(4.6) is fitted with the experimental data using the nonlinear optimization software. In Fig.4.1, the  $I_D$ - $V_{GS}$  characteristics obtained from the proposed model are compared with the experimental data and a perfect match is seen between the two. The extracted values of the model parameter are given along side in Fig.4.1.

### 4.3 Comparison between the BSIM Mobility Model and the Proposed Mobility Model

In order to make a comparison between the BSIM mobility model and the proposed mobility model, the following steps are performed:

- 1) The drain current model proposed by Deshpande and Dutta [27] (which uses the traditional BSIM mobility model) is taken up and fitted with the experimental data for a short channel device.
- 2) The drain current model proposed in this work [as given by Eq.(4.6)] is then taken up and fitted with the experimental data for the same device.
- 3) Then, the values of the model parameters obtained from steps 1 and 2 are used in order to make a comparison between the two mobility models.

The details of the procedure are explained as follows.

For the experimental data, the  $I_D$ - $V_{GS}$  characteristics for a 0.26  $\mu\text{m}$  channel length n-MOSFET have been taken from the work reported by Langevelde and Klaassen [15]. The drain current model, as proposed by Deshpande and Dutta [27], can be expressed as



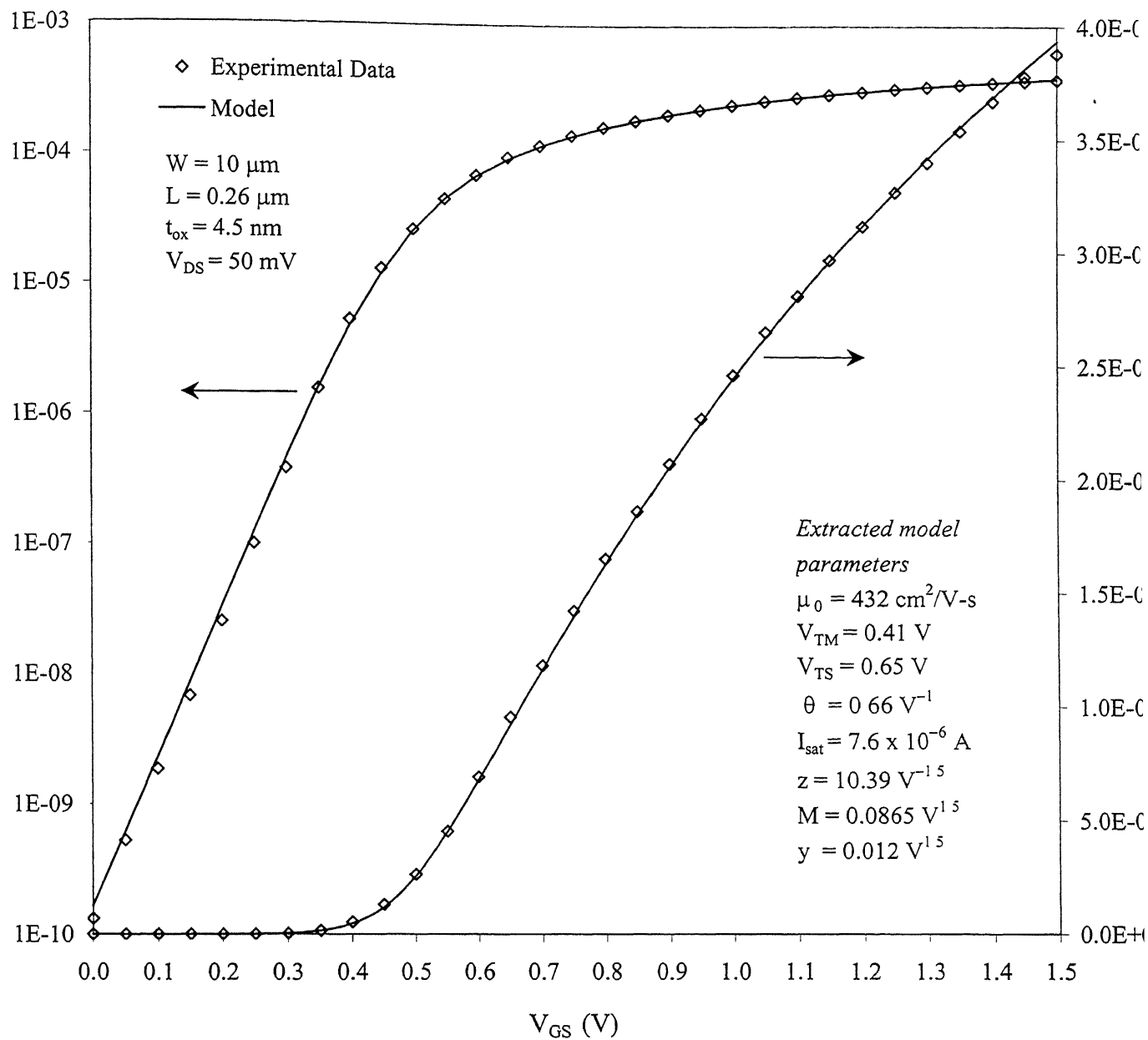


**FIGURE 4.1 :** Comparison of the  $I_D$  versus  $V_{GS}$  characteristics obtained from the proposed model with the experimental data for a  $0.26 \mu\text{m}$  channel length MOSFET, as reported by Langevelde and Klaassen [15]. This comparison has been shown both in log scale (in left) and in linear scale (in right).

$$I_D = \frac{I_{sat} I_{sub}}{I_{sat} + I_{sub}} + \frac{W}{L} C'_{ox} \mu_{eff,BSIM} V_{GTX} V_{DS}, \quad (4.7)$$

where  $I_{sub}$  is defined by Eq.(2.21), and  $\mu_{eff}$  and  $V_{GTX}$  can be defined as

$$\mu_{eff,BSIM} = \frac{\mu_0}{1 + \theta V_{GTX}}, \quad (4.8)$$

and

$$V_{GTX} = s \ln \left( 1 + e^{\frac{V_{GS} - V_T}{s}} \right), \quad (4.9)$$

where  $s$  (in  $V^{-1}$ ) is the fitting parameter. Here, it should be noted that the term  $V_T$  is used instead of  $V_{TM}$  because the authors [27] did not use the term  $V_{TM}$  in their drain current model. Thus, the overall drain current model becomes

$$I_D = \frac{I_{sat} I_0 e^{\frac{V_{GS} - V_T}{\eta V_{th}}}}{I_{sat} + I_0 e^{\frac{V_{GS} - V_T}{\eta V_{th}}}} + \frac{W}{L} C'_{ox} \frac{\mu_0}{1 + \theta V_{GTX}} V_{GTX} V_{DS}. \quad (4.10)$$

Now, this equation is fitted with the experimental data using the nonlinear optimization software. The extracted values of  $\mu_0$ ,  $\theta$ ,  $s$ , and  $V_T$  are  $432 \text{ cm}^2/\text{V-sec}$ ,  $0.66 \text{ V}^{-1}$ ,  $0.0463 \text{ V}$ , and  $0.503 \text{ V}$  respectively. Using these model parameters, the BSIM mobility model [as given by Eq.(4.8)] is plotted as a function of  $V_{GS}$  in Fig.4.2, which shows a continuous fall off of  $\mu_{eff}$  with increasing  $V_{GS}$ .

In the same figure, using the values of the model parameters (which are listed along side in Fig.4.1), the proposed mobility model [which can be found by replacing  $V_{GS} - V_{TM}$  terms with

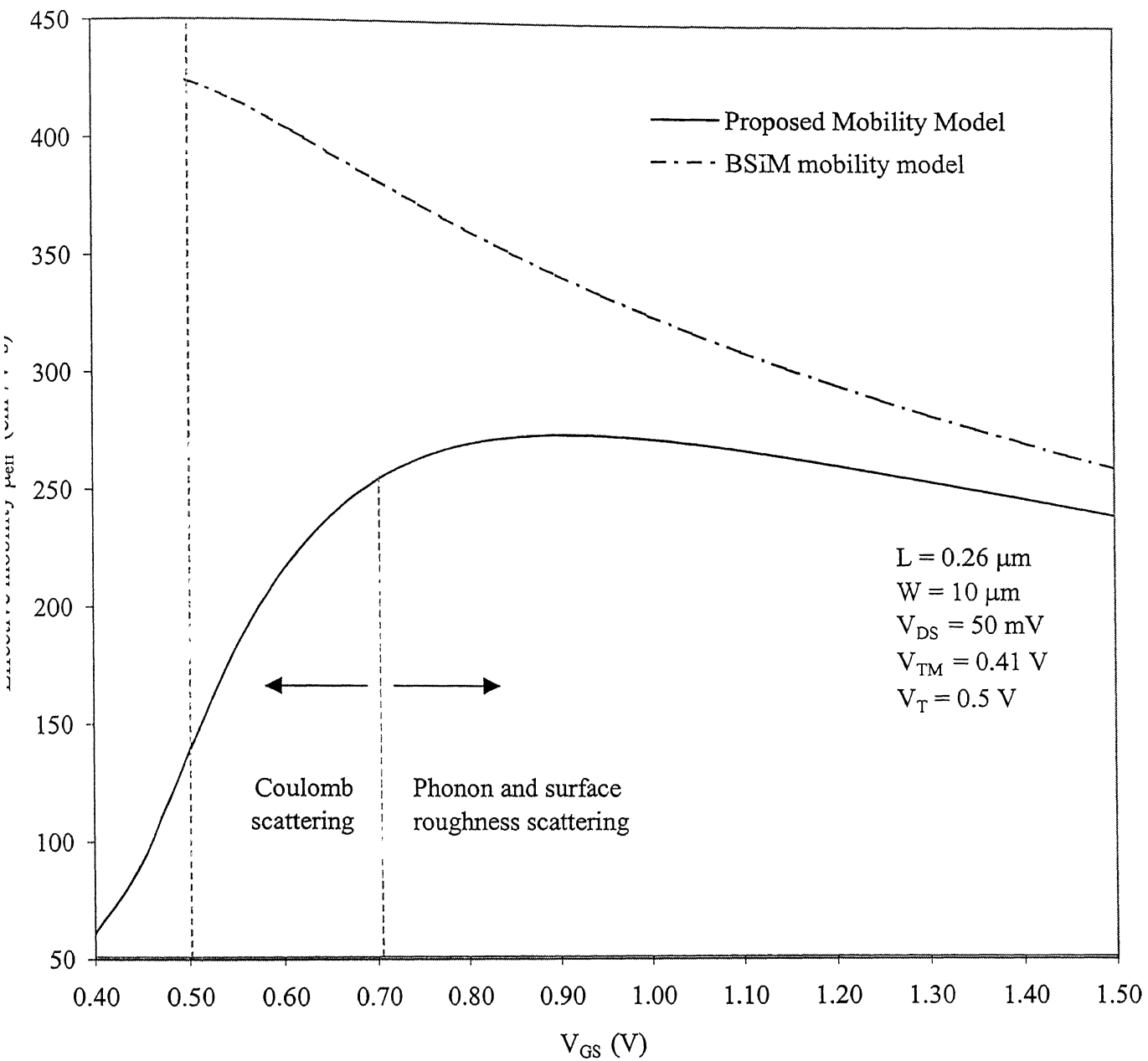


**FIGURE 4.2 :** Comparison between the traditional BSiM mobility model with the model proposed in this work, based on the experimental data for a  $0.26 \mu\text{m}$  channel length MOSFET, as reported by Langevelde and Klaassen [15].

$V_{GTMX}$  in Eqs.(3.6) and (3.7)] is also plotted as a function of  $V_{GS}$ . From this figure, it can be seen that the proposed mobility model ( $\mu_{eff,proposed}$ ) increases with  $V_{GS}$  for  $V_{GS} < V_{TM} + 0.3$  V. However, for the same condition,  $\mu_{eff,BSIM}$  decreases with  $V_{GS}$ . This behavior proves that the proposed model can explain the Coulomb scattering phenomenon in the moderate inversion region, whereas the BSIM mobility model seems to be overestimating the mobility in this region. As the gate voltage increases beyond  $V_{TM} + 0.3$  V,  $\mu_{eff,proposed}$  decreases with  $V_{GS}$  due to the effects of the phonon scattering and the surface roughness scattering, and  $\mu_{eff,BSIM}$  also shows a similar behavior in this region. For high values of  $V_{GS}$ , both the proposed model and BSIM tend to converge with each other. However, for high  $V_{GS}$ , the two curves do not exactly coincide with each other since the values of  $V_T$  and  $s$  are quite different for the two cases. Therefore, it can be concluded that in the low field region (i.e., for  $V_{TM} < V_{GS} < V_{TM} + 0.3$  V), the proposed model differs from the BSIM mobility model due to the inclusion of the Coulomb scattering effect. However, for high electric fields, the Coulomb scattering has less effect on the effective mobility of the inversion layer electrons and  $\mu_{eff}$  is mostly determined by the phonon and the surface roughness scattering effects. As the proposed model considers all the three scattering effects ( $\mu_c$ ,  $\mu_{ph}$ , and  $\mu_{sr}$ ) and BSIM only includes the phonon and the surface roughness scattering effects, hence, these two models differ in the moderate inversion region, however, show a similar behavior in the strong inversion region.

## 4.4 Verification of the Proposed Drain Current Model

In this section, the drain current model, which is given by Eq.(3.11), is verified with the recently published experimental data for short channel MOSFETs. In this work here, nonlinear

optimization method is used to extract the model parameters from the experimental data. For the experimental data, the same  $I_D$ - $V_{GS}$  characteristics for the 0.26  $\mu\text{m}$  channel length n-MOSFET [15] have been taken and the extracted value of  $V_{TM}$  is found to be equal to 0.41 V. Using Eqs. (3.11) and (4.1), one can express the overall drain current model for the weak and the moderate inversion regions as

$$I_D = I'_{sub} + I'_{str}$$

$$= \frac{I_{sat} I_0 e^{\frac{V_{GS}-V_{TM}}{\eta V_{th}}}}{I_{sat} + I_0 e^{\frac{V_{GS}-V_{TM}}{\eta V_{th}}}} + \frac{W}{L} C'_{ox} \mu_0 \zeta V_{GTMX}^{1.5} V_{DS} \quad (4.11)$$

Here, Eq.(3.11) is used in order to model the  $I'_{str}$  component of Eq.(4.1). The region of the experimental data is taken up for values of  $V_{GS}$  from 0 V to 0.6 V, since the drain current model as given by Eq.(4.11) is valid only in the weak and the moderate inversion regions. Afterwards, this equation is fitted with the experimental data of the said region using the nonlinear optimization software. In Fig.4.3, the  $I_D$ - $V_{GS}$  characteristics obtained from the proposed model is compared with the experimental data and it shows a perfect match between the two. The extracted values of the model parameters are given along side in Fig.4.3.

The results predicted by the proposed model are also verified with the experimental data reported in the literature for sub-0.1  $\mu\text{m}$  channel length devices. As another example, the experimental data obtain from the  $I_D$ - $V_{GS}$  characteristics for a 0.09  $\mu\text{m}$  channel length device has been taken from the work reported by Mii *et al.* [16]. The device has the following parameters: gate length (L) of 0.09  $\mu\text{m}$ , gate width (W) of 10  $\mu\text{m}$ , and oxide thickness ( $t_{ox}$ ) of 35  $\text{\AA}$ . The

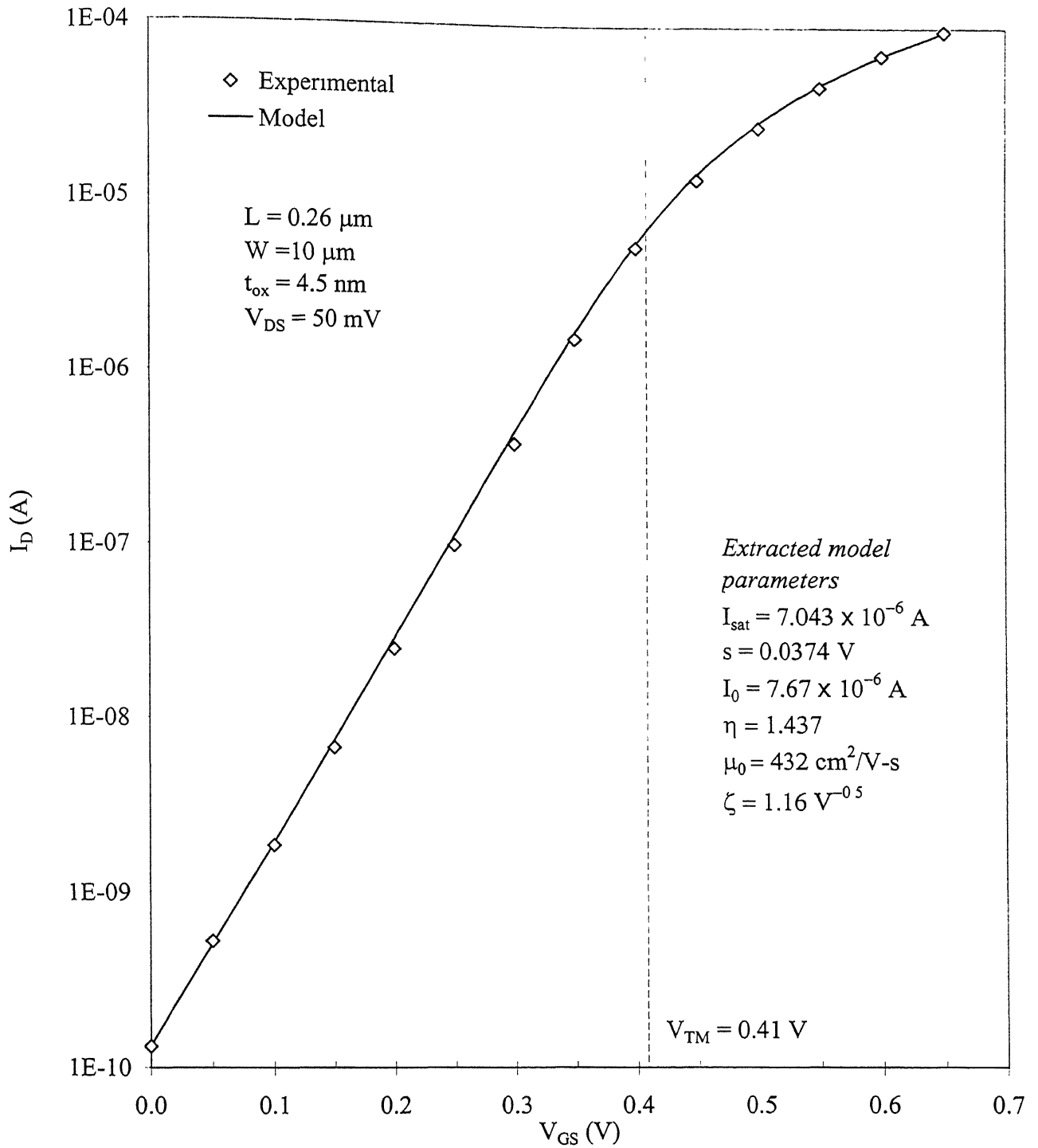


**FIGURE 4.3 :** Comparison of the  $I_{\text{D}}$  versus  $V_{\text{GS}}$  characteristics obtained from the proposed drain current model [Eq.(4.11)] with the experimental data for a  $0.26 \mu\text{m}$  channel length MOSFET, as reported by Langevelde and Klaassen [15].

parameter  $V_{TM}$  is extracted using the method proposed in Section 6.1, and is found to be equal to 0.25 V. The region of the experimental data is taken up for values of  $V_{GS}$  from 0 V to 0.45 V for the comparison between the model and the experimental data. Then, the parameter extraction procedure is carried out to find the values for the model parameters in the same way as was done for the 0.26  $\mu\text{m}$  channel length device. In Fig.4.4, the  $I_D$ - $V_{GS}$  characteristics obtained from the proposed model is compared with this experimental data [16] and it shows a perfect match between the two. The extracted values of the model parameters are given along side in Fig.4.4. From these results, it can be inferred that the proposed model can be reliably applied for the characterization of the moderate inversion region behavior of short channel MOSFETs.

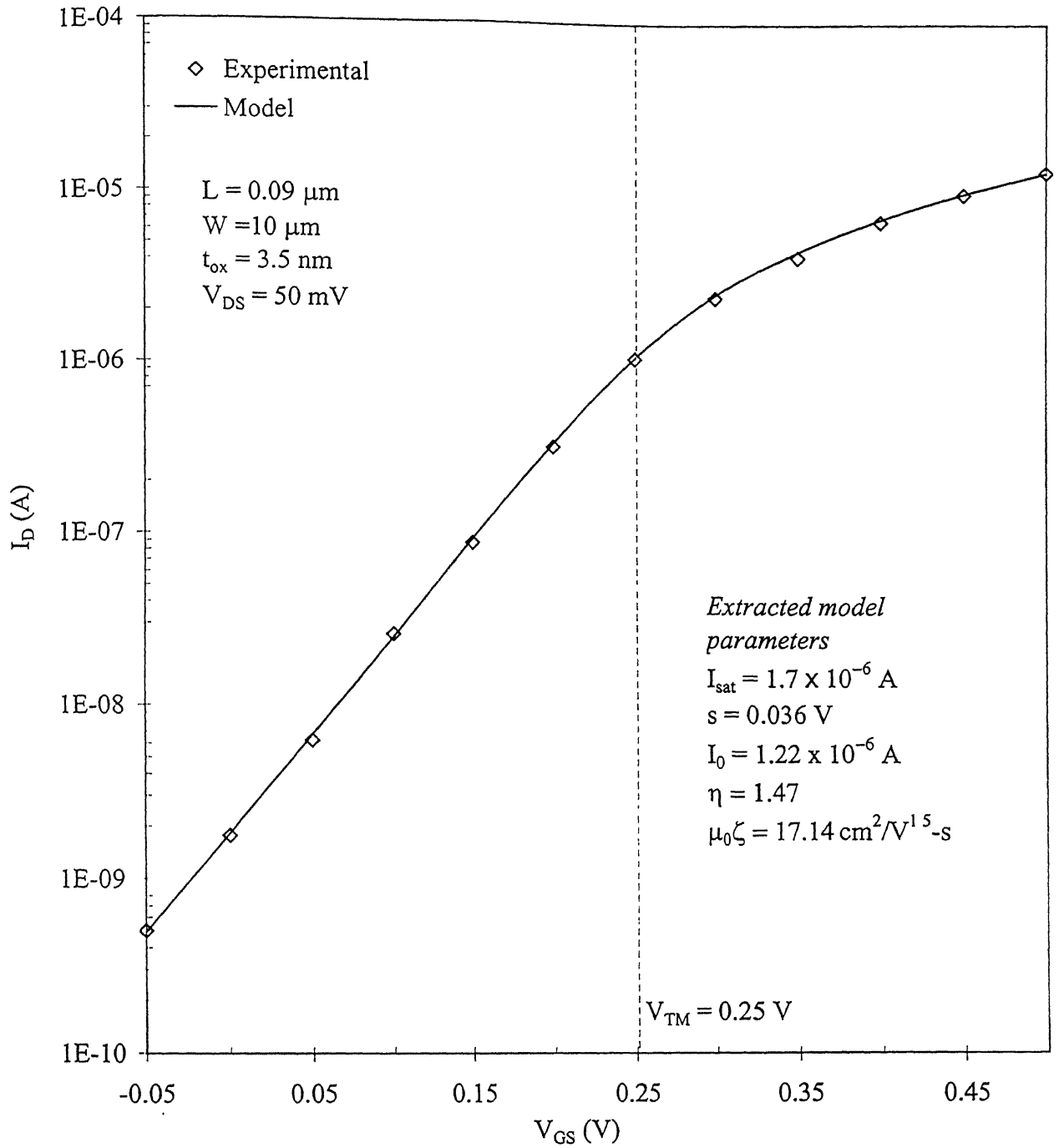


**FIGURE 4.4 :** Comparison of the  $I_D$  versus  $V_{\text{GS}}$  characteristics obtained from the proposed drain current model [Eq.(4.11)] with the experimental data for a  $0.09 \mu\text{m}$  channel length MOSFET, as reported by Mii *et al.* [16].



# Development of the Threshold Voltage Extraction Method

---

Parasitic source/drain series resistance is frequently significant in submicron MOSFETs. It represents a complication for the extraction of the device model parameters from the experimental I-V characteristics. Many methods have been proposed in the literature to perform the threshold voltage extraction even in the presence of series resistance [9,12–14]. Most of these methods rely upon differentiating the measured I-V characteristics, which tends to worsen the experimental measurement errors that might be present in the data. Conde *et al.* [10] has proposed an alternative method, which is based on the use of the integral of the data in place of the differentiation technique. They introduced a new function called the ‘D function’ [10,30], which acts as a low pass filter, and, thus, tends to lessen the effects of the measurement errors and the S/D resistance effects on the parameter extraction procedure. Based on their method, a superior method has been developed in this work in order to extract the threshold voltage ( $V_{TM}$ ) at the ‘onset of the moderate inversion region’ from the experimental  $I_D$ - $V_{GS}$  characteristics.

## 5.1 The ‘Difference Function’ $D$

Let  $d$  and  $r$  be two generalized two-terminal devices connected in series. A terminal voltage  $V$  is applied to this series combination causing a current  $I$  to flow through the devices, which produces voltage drops  $V_d$  and  $V_r$  across them respectively. Let the current be defined by the functions  $f(V_d)$ ,  $h(V_r)$ , and  $g(V)$  of the voltages across the terminals of the two devices and the series combination respectively. Thus,

$$I = f(V_d) = h(V_r) = g(V). \quad (5.1)$$

The voltages can be expressed by their corresponding inverse functions of current as

$$g^{-1}(I) = f^{-1}(I) + h^{-1}(I). \quad (5.2)$$

Using geometric considerations, equivalent to integration by parts, the following equalities can be written as

$$\int_0^{V_{d0}} I dV_d + \int_0^{I_0} V_d dI = I_0 V_{d0}, \quad (5.3)$$

$$\int_0^{V_{r0}} I dV_r + \int_0^{I_0} V_r dI = I_0 V_{r0}, \text{ and} \quad (5.4)$$

$$\int_0^{V_0} I dV + \int_0^{I_0} V dI = I_0 V_0. \quad (5.5)$$

where  $V_{d0}$ ,  $V_{r0}$ , and  $V_0$  are the upper voltage integration limits corresponding to an upper current integration limit  $I_0$  at a certain point in the  $I$ - $V$  characteristics of the devices and the terminals.

Integrating the sum of the two voltages of the devices with respect to the current from 0 to  $I_0$  gives

$$\int_0^{I_0} V \, dI = \int_0^{I_0} V_d \, dI + \int_0^{I_0} V_r \, dI. \quad (5.6)$$

Substitution of Eqs.(5.3), (5.4), and (5.5) into Eq.(5.6) produces a similar expression for the integrals of the current with respect to the three voltages

$$\int_0^{V_0} I \, dV = \int_0^{V_{d0}} I \, dV_d + \int_0^{V_{r0}} I \, dV_r. \quad (5.7)$$

Finally, subtracting Eq.(5.7) from Eq.(5.6), one can define the ‘difference function’  $D$  as

$$\begin{aligned} D &= \int_0^{I_0} V \, dI - \int_0^{V_0} I \, dV \\ &= \left( \int_0^{I_0} V_d \, dI - \int_0^{V_{d0}} I \, dV_d \right) + \left( \int_0^{I_0} V_r \, dI - \int_0^{V_{r0}} I \, dV_r \right). \end{aligned} \quad (5.8)$$

This function is valid not only for this case of two devices in series, but also in general for any number of generalized devices connected in series [10].

## 5.2 The Properties of the ‘ $D$ Function’

The first and second terms on the right hand side of Eq.(5.8) are defined as the content and co-content of the device, respectively, and  $V$  and  $I$  are the device terminal voltage and current respectively. The integral function can also be considered as a measure of the

nonlinearity of the device, which would be zero for a device with only linear elements, since the content and the co-content are identical for such a device [10].

Any arbitrary two-terminal device with both linear and nonlinear elements has the following properties [6]

- a) The summation of the contents over all branches (i.e., all the parasitic resistances and other nonlinear components associated with the equivalent circuit of the device) is zero.
- b) The summation of the co-contents over all branches is zero.

Therefore, the summation of the function D over all branches is zero. In other words, D eliminates the effect of the linear elements, such as series resistances, and can be used for extracting intrinsic parameters of semiconductor devices.

### 5.3 The ‘G Function’

The D function has two integral terms. In order to reduce the complexity of the calculations, a new function G can be derived from the D function in the following manner

$$D = \int_0^{I_0} V dI - \int_0^{V_0} I dV \quad (5.9)$$

By partial differentiation of the first integration term on the right - hand side of Eq.(5.9), one gets

$$D = I_0 V_0 - \int_0^{I_0} \left[ \frac{dV}{dI} \int dI \right] dI - \int_0^{V_0} I dV$$

Here  $g_D$  is defined as  $g_D = \frac{V_{DS}}{I_D}$ , where  $V_{DS}$  is the drain to source voltage and  $I_D$  is the drain current of the device.

Although these functions are especially defined for three terminal devices, it can be used for the parameter extraction for two terminal devices as well. These functions have been derived empirically in order to eliminate the effect of the parasitic series resistances on the MOSFET model parameter extraction procedure. These equations can be used as a tool for MOSFET parameter extraction. Although these functions are purely empirical in nature, however, it can be proved (both theoretically and with the help of AIM-SPICE simulator) that these functions can eliminate the effect of series resistances from the I-V characteristics of any nonlinear device.

## 5.5 Case of a Constant Series Resistance

Let a current  $I$ , flowing through a constant resistance  $R$ , produces a voltage drop  $V$  across it. If  $V_x$  and  $I_x$  are calculated for the resistance  $R$ , one gets

$$g_D = \frac{1}{R} .$$

Putting this value of  $g_D$  in Eqs.(5.12) and (5.13), one gets

$$V_x = V - \frac{\int_0^V \frac{1}{R} dV}{\frac{1}{R}} = V - \frac{\frac{V}{R}}{\frac{1}{R}} = 0, \text{ and} \quad (5.14)$$

$$I_x = \int_0^V \frac{1}{R} dV - I = \frac{V}{R} - I = 0. \quad (5.15)$$

From the above result, it can be inferred that if the  $V_x$  and  $I_x$  functions are calculated from the  $V_{GS}$  versus  $I_D$  characteristics of a MOSFET, then it will eliminate the series source/drain resistances, provided these are constants. This property of the  $V_x$  and  $I_x$  functions can also be proved from AIM-SPICE [7] simulation carried out in this work. The level-10 MOSFET model in AIM-SPICE is used for this simulation, and the following parameters are used: a threshold voltage of 0.7 V, a mask channel width of 8  $\mu\text{m}$ , a mask channel length of 0.5  $\mu\text{m}$ , a junction depth of 0.10  $\mu\text{m}$  with a lateral extent of 0.075  $\mu\text{m}$ , an oxide thickness of 10 nm, a substrate doping of  $10^{17} \text{ cm}^{-3}$ , and a low field mobility of  $331.5 \text{ cm}^2/\text{V}\cdot\text{s}$ . The value of  $V_{DS}$  is taken to be a constant at 50 mV and  $V_{GS}$  is incremented from 0 V to 1.5 V in steps of 10 mV. Four  $I_D$ - $V_{GS}$  characteristics have been simulated for four different values of source/drain series resistances ( $R_s$ ,  $R_d$ ), and these are shown in Fig.5.1(a). The  $V_x$  and  $I_x$  functions are numerically calculated for each of the four simulated characteristics. Then the numerically calculated values of the  $I_x$  function are plotted as a function of the  $V_x$  function for all the four cases, as shown in Fig.5.1(b). It can clearly be seen that all the four characteristics appear almost superimposed on each other, and, thus, it is conclusively proved that the effect of the series resistance is eliminated by these  $V_x$  and  $I_x$  functions. The method of the threshold voltage extraction using these  $V_x$  and  $I_x$  functions is presented in the next chapter.

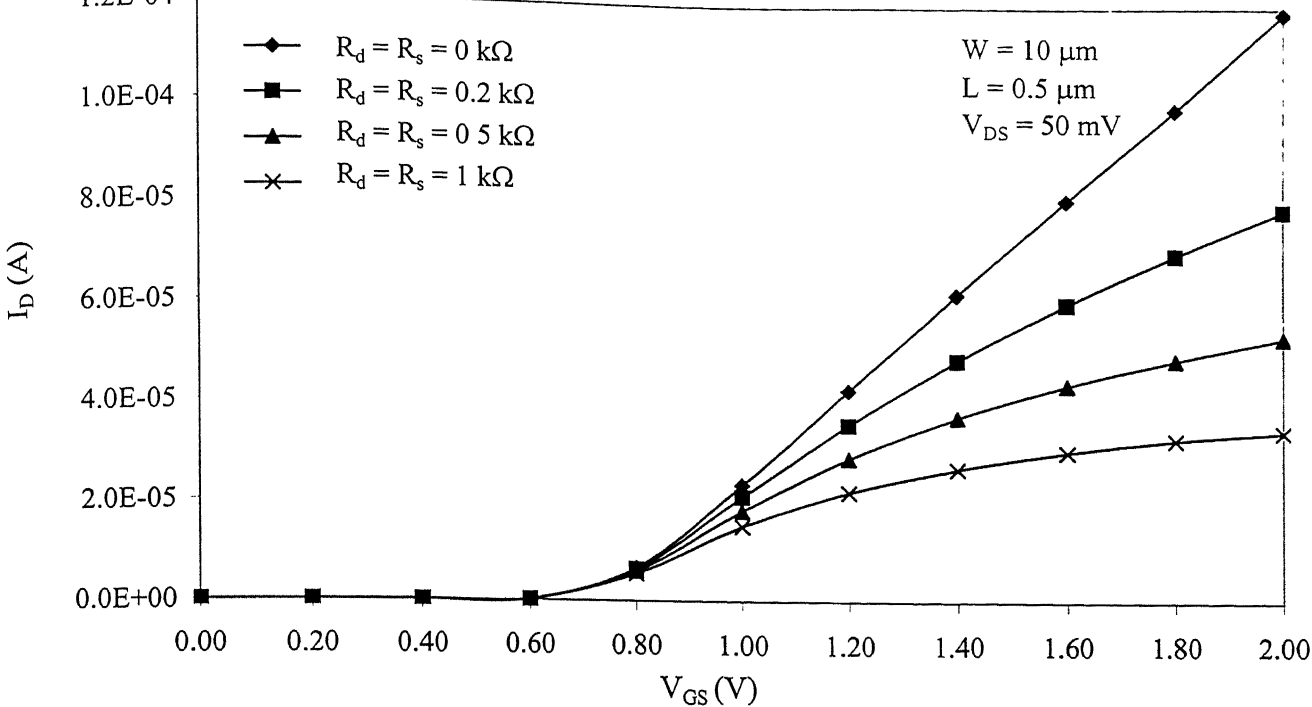


**FIGURE 5.1(a) :** The  $I_D$ - $V_{GS}$  characteristics of an n-MOSFET for four different values of series source/drain resistances, simulated with the help of the AIM-SPICE simulator (Level -10) [7].

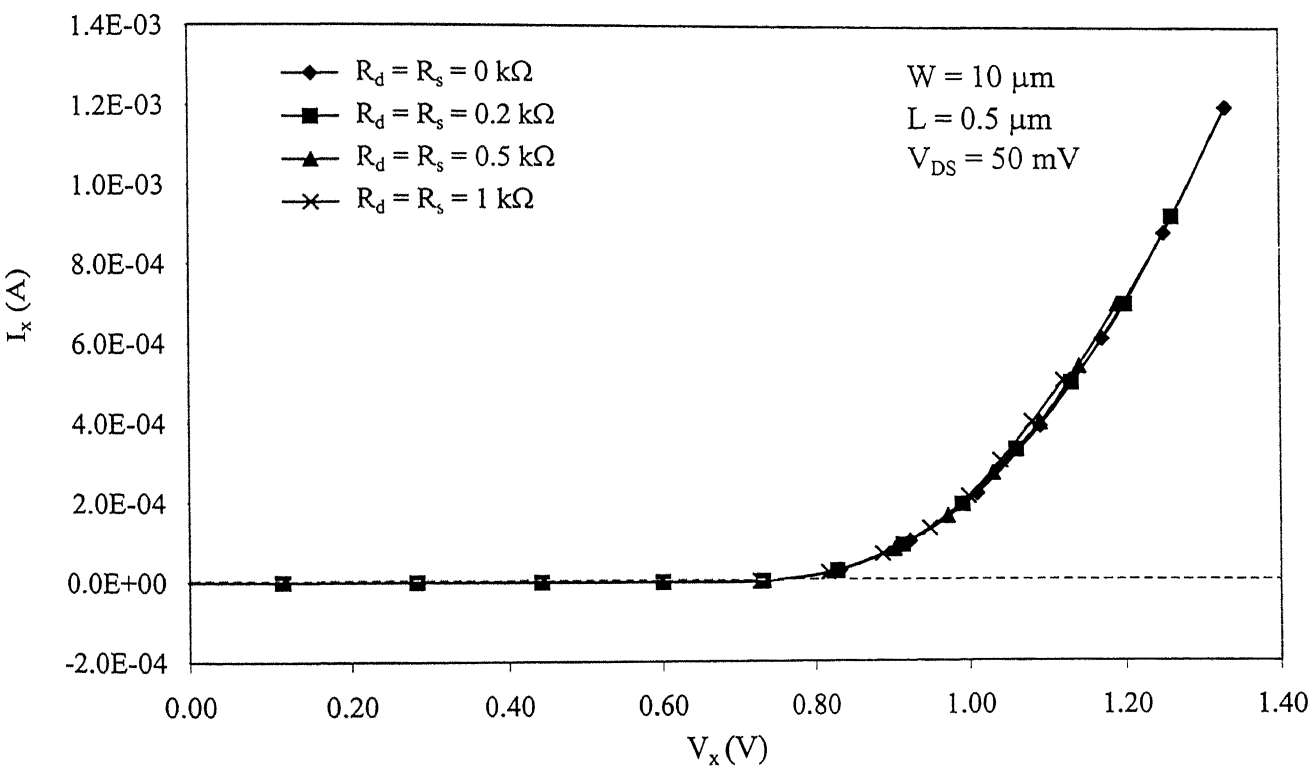


**FIGURE 5.1(b) :** The  $I_x$ - $V_x$  characteristics obtained from Fig.5.1(a) for the same values of series resistances as in Fig.5.1(a).

# The Threshold Voltage Extraction

---

In this chapter, an alternative technique for the threshold voltage extraction is presented. It uses the  $V_x(V_{GS}, I_D)$  and  $I_x(V_{GS}, I_D)$  functions, which are proposed in the previous chapter.

## 6.1 Description of the Procedure

For the experimental data, the  $I_D$ - $V_{GS}$  characteristics for a 0.26  $\mu\text{m}$  channel length n-MOSFET have been taken from the work reported by Langevelde and Klaassen [15]. The characteristics are measured at a constant  $V_{DS}$  (50 mV) and  $V_{GS}$  is incremented from 0 V to 1.5 V in steps of 10 mV. The device has the following parameters: gate length ( $L$ ) of 0.26  $\mu\text{m}$ , gate width ( $W$ ) of 10  $\mu\text{m}$ , and gate oxide thickness ( $t_{ox}$ ) of 45  $\text{\AA}$ . For each value of  $V_{GS}$ , the corresponding values of  $V_x$  and  $I_x$  have been calculated numerically using Eqs.(5.12) and (5.13). For example, if  $I_D = 2 \times 10^{-7}$  A at  $V_{GS} = 0.5$  V, then  $V_x(V_{GS}, I_D)$  and  $I_x(V_{GS}, I_D)$  at  $V_{GS} = 0.5$  V can be calculated in the following way



$$V_x|_{V_{GS}=0.5\text{ V}} = 0.5 - \frac{\int_0^{0.5} \frac{I_D}{0.05} dV_{GS}}{\frac{2 \times 10^{-7}}{0.05}}, \text{ and}$$

$$I_x|_{V_{GS}=0.5\text{ V}} = \int_0^{0.5} \frac{I_D}{0.05} dV_{GS} - 2 \times 10^{-7}.$$

The integration terms have to be calculated numerically. In this work, Simpson's rule is used for the numerical integration. In this way, for each value of  $V_{GS}$ , one can get unique values of  $V_x$  and  $I_x$ . The function  $I_x(V_{GS}, I_D)$  shows a negative peak at  $V_{GS} = 0.41\text{ V}$ , when it is plotted as a function of  $V_{GS}$ , as shown in Fig.6.1. This peak is denoted by  $V_{TM}$  in this work. From the same figure, it can be seen that a similar negative peak occurs when  $I_x(V_{GS}, I_D)$  is plotted as a function of  $V_x(V_{GS}, I_D)$ . The value of  $V_x(V_{GS}, I_D)$ , at which this peak occurs, is denoted by  $V_{2\phi}$  in this work. From Fig.6.1, it can be seen that  $V_{2\phi} = 0.368\text{ V}$ .

## 6.2 The Mathematical Foundation\*

Replacing the term  $(W/L)C'_{ox}\mu_0\zeta$  with a new parameter  $K_1$  (i.e.,  $K_1 = K\zeta$ ), one can rewrite Eq.(4.11) as

$$I_D = \frac{I_{sat} I_0 e^{\frac{V_{GS}-V_{TM}}{\eta V_{th}}}}{I_{sat} + I_0 e^{\frac{V_{GS}-V_{TM}}{\eta V_{th}}}} + K_1 V_{GTMX}^{1.5} V_{DS}. \quad (6.1)$$

---

\* For a complete derivation of the equations, please see the Appendix.

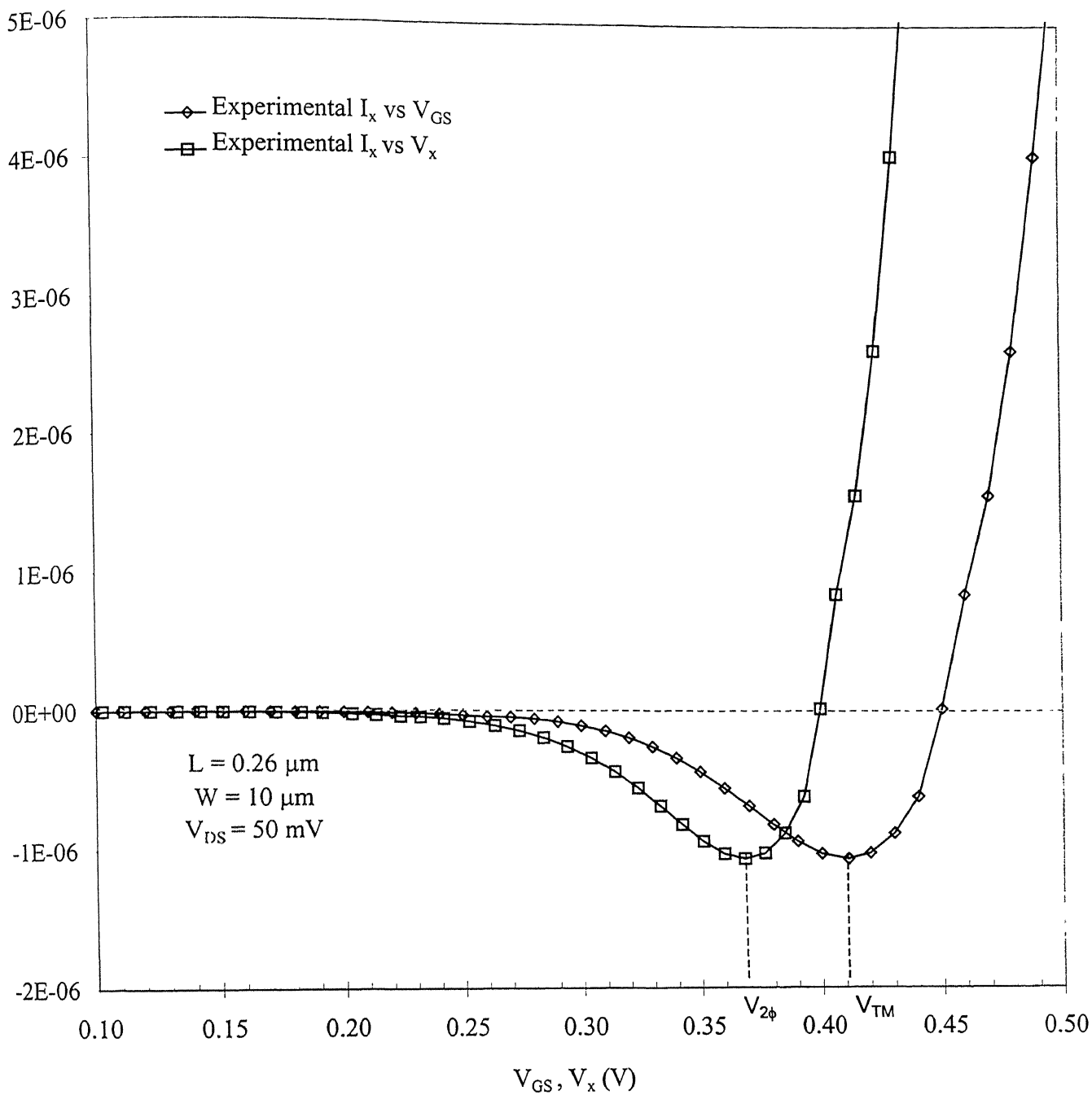


**FIGURE 6.1** : The  $I_x$  function calculated numerically from the experimental data, as reported by Langevelde and Klaassen [15], as a function of  $V_{GS}$  and  $V_x$ .

In order to obtain a simpler drain current model, the following assumptions have been made in this work.

1) For  $V_{GS} > V_{TM}$ ,  $I_0 e^{\frac{V_{GS}-V_{TM}}{\eta V_{th}}} \gg I_{sat}$ , and, hence, the first term of the right-hand side of Eq.(6.1)

becomes approximately equal to  $I_{sat}$ .

2) For  $V_{GS} < V_{TM}$ ,  $V_{GTMX} = 0$ , and otherwise it is equal to  $(V_{GS} - V_{TM})$ .

Therefore, one can simplify Eq.(6.1) into the following equations

$$I_D \approx I_0 e^{\frac{V_{GS}-V_{TM}}{\eta V_{th}}}, \quad \text{for } V_{GS} < V_{TM}, \text{ and} \quad (6.2)$$

$$I_D \approx I_{sat} + K_1(V_{GS} - V_{TM})^{1.5} V_{DS}, \quad \text{for } V_{GS} < V_{TM} < V_{TS}. \quad (6.3)$$

With the help of Eqs.(6.2) and (6.3), one can derive the expressions for  $I_x(V_{GS}, I_D)$  as follows

$$I_x = \frac{a}{b V_{DS}} \exp(b V_{GS}) [1 - b V_{DS}] - \frac{a}{b V_{DS}}, \quad \text{for } V_{GS} \leq V_{TM}, \quad (6.4)$$

where  $a = I_0 \exp(-\frac{V_{TM}}{\eta V_{th}})$  and  $b = \frac{1}{\eta V_{th}}$ ,

and for  $V_{GS} > V_{TM}$ ,

$$I_x = \frac{I_0 - a}{b V_{DS}} + \frac{I_{sat}}{V_{DS}} (V_{GS} - V_{TM}) - I_{sat} + \frac{K_1 (V_{GS} - V_{TM})^{2.5}}{2.5} - K_1 (V_{GS} - V_{TM})^{1.5} V_{DS}. \quad (6.5)$$

In the same way, the analytical expression for  $V_x$  for  $V_{GS} \leq V_{TM}$  can be found as

$$V_x = V_{GS} - \eta v_{th} \left[ 1 - \exp \left( - \frac{V_{GS}}{\eta v_{th}} \right) \right], \quad (6.6)$$

and for  $V_{GS} \gg \eta v_{th}$ ,

$$V_x \approx V_{GS} - \eta v_{th}. \quad (6.7)$$

The exact analytical expression for  $V_x$ , for  $V_{GS} > V_{TM}$ , is not important for this work (since this work primarily aims at determining the exact value of  $V_{TM}$ ), and, hence, it is not derived here. As stated in the previous section, a negative peak in  $I_x$  appears at  $V_{GS} = 0.41$  V, when  $I_x(V_{GS}, I_D)$  is plotted as a function of  $V_{GS}$  (Fig.6.1). Here, an assumption is made in this work that the value of  $V_{GS}$  corresponding to this peak denotes the ‘onset of the moderate inversion region’ (i.e.  $V_{TM} = 0.41$  V). Taking this value to be that of  $V_{TM}$ , the parameter extraction procedure is carried out in order to find the values of the model parameters to be used in Eqs.(6.4) and (6.5). The parameter extraction procedure is performed in the following way.

1. One region of the experimental  $I_D$ – $V_{GS}$  data is taken for values of  $V_{GS}$  between 0 V and 0.41 V. Then, Eq.(6.2) is fitted (by nonlinear optimization software GNU PLOT [29]) with the experimental data for the said region. The following values of  $a$ ,  $b$ , and  $\eta$  have given the least error between the experimental data and the results predicted by our subthreshold drain current model:  $a = 1.3183 \times 10^{-10}$  A,  $b = 26.75$  V<sup>-1</sup>, and  $\eta = 1.43$ .
2. Again another region of the experimental  $I_D$ – $V_{GS}$  data is taken where  $V_{GS}$  is varying from 0.41 V to 0.61 V (since Eq.(6.3) is valid only within this region). Then, Eq.(6.3) is fitted (by nonlinear optimization software [29]) with the experimental data for the said region. The following values of  $I_{sat}$  and  $K_1$  have given the least error between the experimental data and

the results predicted by our drain current model:  $I_{\text{sat}} = 6.615 \times 10^{-6}$  A and  $K_1 = 1.488 \times 10^{-2}$   $\text{AV}^{-2.5}$

Now, these values of the model parameters are plugged into Eqs.(6.4) and (6.5) and the values of  $I_x$  are calculated and plotted as a function of  $V_{\text{GS}}$ , as shown in Fig.6.2. This characteristic can be treated as the theoretical  $I_x$  versus  $V_{\text{GS}}$  characteristic, and in Fig.6.2 it is denoted by A. The  $I_x(V_{\text{GS}}, I_{\text{D}})$  versus  $V_{\text{GS}}$  characteristic, which is calculated numerically from the experimental data and appears in Fig.6.1, is also plotted in Fig.6.2 and is denoted by B. This characteristic can be treated as the experimental  $I_x$  versus  $V_{\text{GS}}$  characteristic. In Fig.6.2, the numerically calculated  $I_x(V_{\text{GS}}, I_{\text{D}})$  characteristic is also plotted as a function of the numerically calculated  $V_x(V_{\text{GS}}, I_{\text{D}})$  and is denoted by C. From Fig.6.2, it can be seen that curves A and B show an almost exact match between them everywhere except near the peak region, and both of them exhibit negative peaks at  $V_{\text{GS}} = 0.41$  V.

## 6.3 Analysis

For typical values of  $\eta$  (which is almost always less than 2) the product term  $\eta v_{\text{th}} (= b^{-1})$  is always less than  $V_{\text{DS}}$  (50 mV). Consequently, the  $bV_{\text{DS}}$  term in Eq.(6.4) is always greater than unity. Therefore, below the onset of the moderate inversion (i.e.,  $V_{\text{GS}} < V_{\text{TM}}$ ), the theoretical  $I_x$  [Eq.(6.4)] values are always negative and decreases exponentially with an increase in  $V_{\text{GS}}$ . The experimental  $I_x$  values (numerically calculated) also show the same behavior for values of  $V_{\text{GS}}$  below  $V_{\text{TM}}$ . However, from Eq.(6.5), one can see that beyond threshold ( $V_{\text{GS}} > V_{\text{TM}}$ ), the

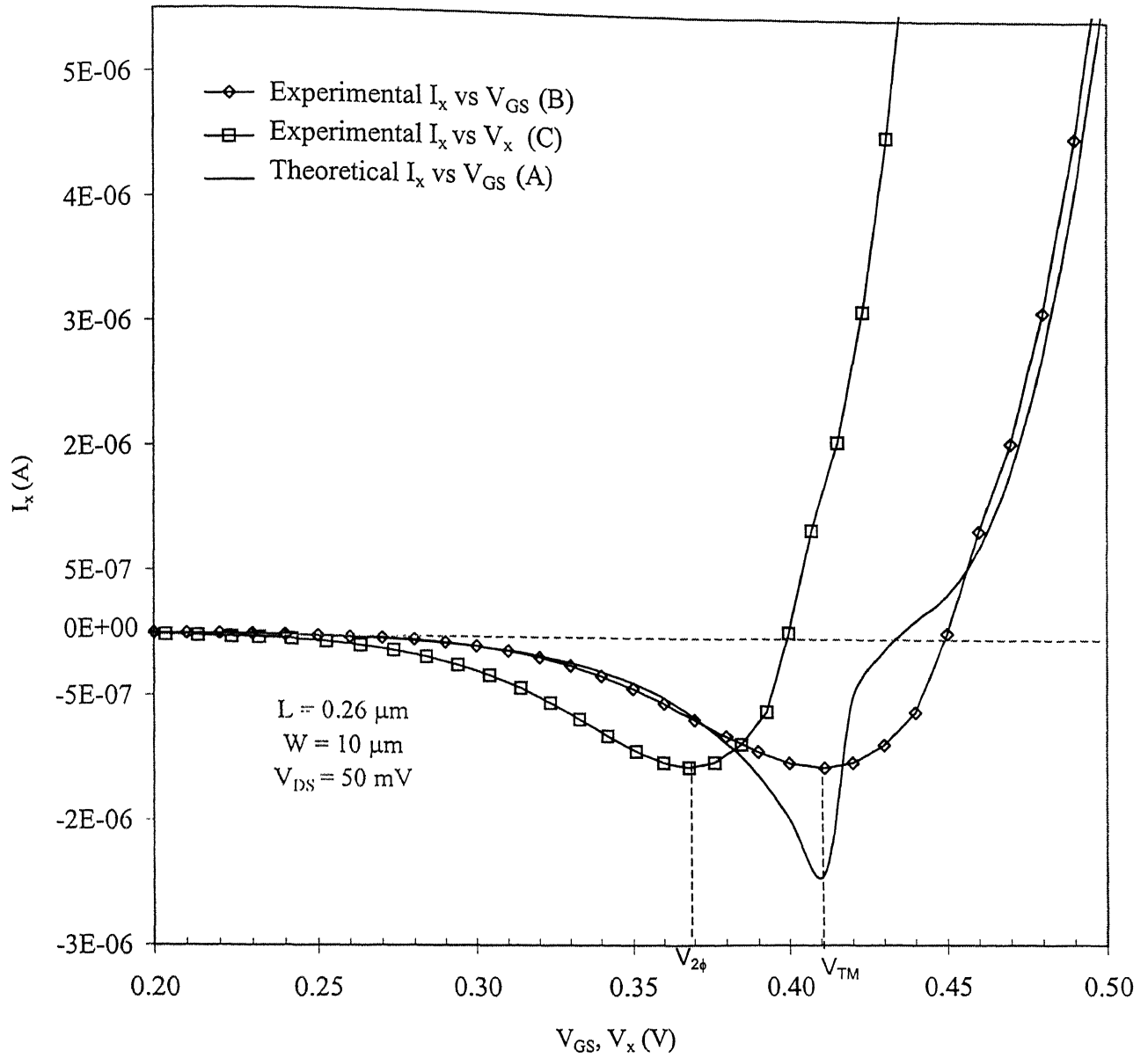


**FIGURE 6.2 :** The  $I_x$  function calculated numerically from the experimental data as reported by Langevelde and Klaassen [15] as a function of  $V_{GS}$  and  $V_x$  (curves B and C respectively). The results simulated from the theoretical model of  $I_x$  [Eqs.(6.4) and (6.5)] proposed in this work is also shown as a function of  $V_{GS}$  (curve A) for comparison.

theoretical values of  $I_x$  increase with increasing values of  $V_{GS}$ . This is because the subthreshold component of the drain current tends to saturate after the threshold voltage ( $V_{TM}$ ) and the drift component of the drain current dominates the current conduction process through the inversion channel. The experimental values of  $I_x$  also increase with increasing  $V_{GS}$  beyond the peak. As a result, both the theoretical (A) and the experimental (B) characteristics exhibit peaks, which separate the two regions, i.e., the weak inversion region and the moderate inversion region. As it was previously assumed that  $V_{TM} = 0.41$  V, and both the experimental and the theoretical values of  $I_x$  exhibit peaks at  $V_{GS} = 0.41$  V, therefore, it can be inferred that the assumption is valid and the negative peak in the  $I_x$  function (while plotted as a function of  $V_{GS}$ ) always occurs at  $V_{GS} = V_{TM}$  (i.e., at the onset of the moderate inversion).

Now from Fig.6.2, it can be seen that the theoretically calculated values of  $I_x$  (curve A) match with the numerically calculated values of  $I_x$  (curve B) everywhere except near the threshold ( $V_{GS} = V_{TM}$ ) region. Again from the characteristic C, it can be seen that a similar peak in  $I_x$  (while plotted as a function of  $V_x$ ) occurs at  $V_x \approx 0.368$  V. This value of  $V_x$  is denoted by  $V_{2\phi}$  in this work. It is interesting to note that the theoretical values of  $I_x$  deviate from the experimental values of  $I_x$  starting from  $V_{GS} = V_{2\phi}$ . In Fig.6.3, the results obtained from the subthreshold drain current model, which is given by Eq.(6.2), is plotted along with the experimental  $I_D$ - $V_{GS}$  characteristics, with the help of the extracted values of the model parameters. From this figure, it can be seen that the results obtained from our subthreshold drain current model match with the experimental data for  $V_{GS} \leq V_{2\phi}$ , however, they differ afterwards. This behavior can be explained in the following way. The subthreshold current model, given by Eq.(6.2), can also be written in the following manner [11]

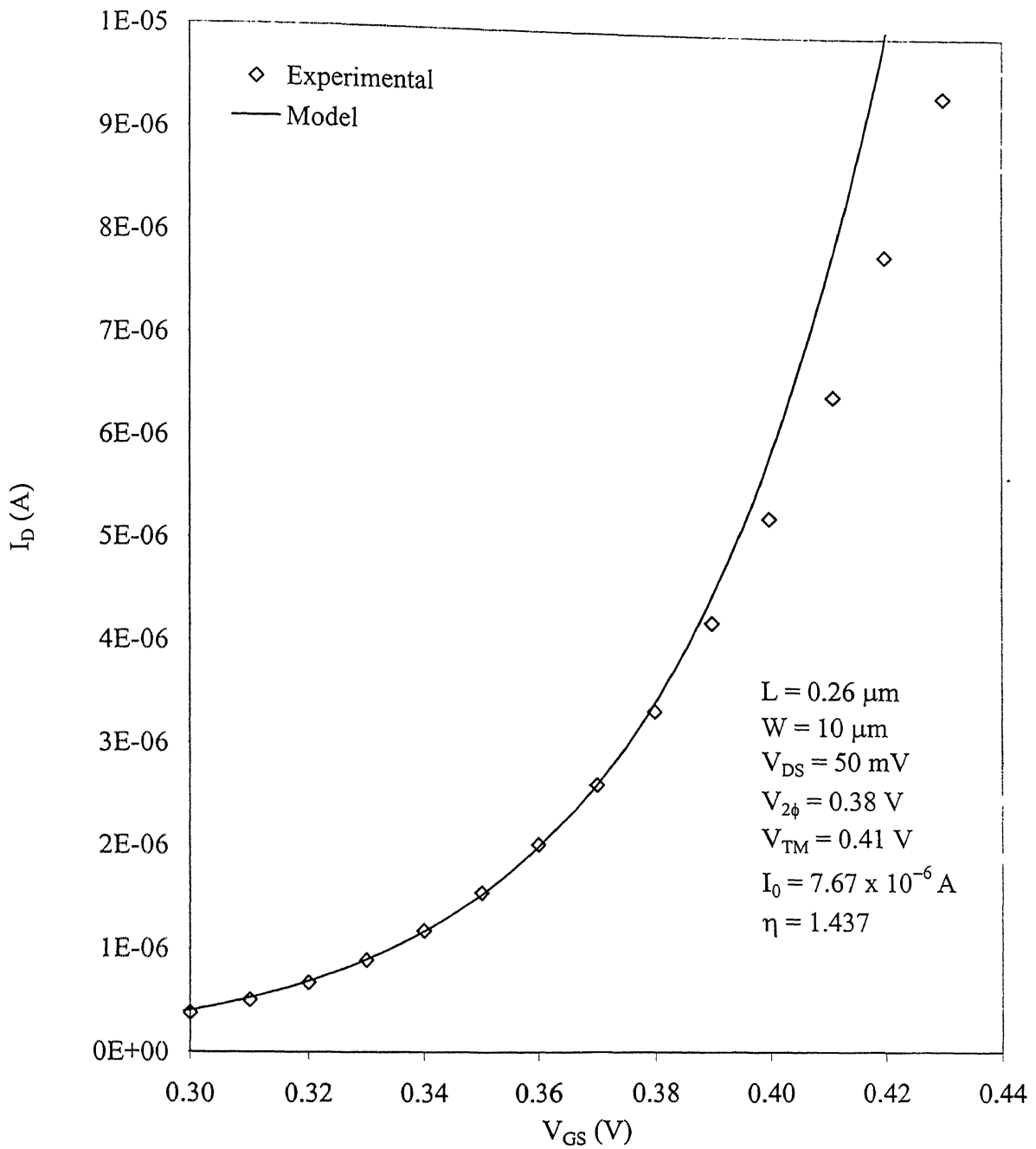


**FIGURE 6.3 :** Comparison of the  $I_D$  versus  $V_{GS}$  characteristics obtained from the proposed subthreshold component of the drain current model [Eq.(6.2)] with the experimental data for a  $0.26 \mu\text{m}$  channel length MOSFET, as reported by Langevelde and Klaassen [15]. These two characteristics exhibit a close match till  $V_{GS} = V_{2\phi} = 0.38 \text{ V}$ , however, they differ afterwards.



$$I_D = \left( \frac{W}{L} \right) \frac{\mu C'_{ox} \gamma V_{th}^2}{2\sqrt{\Psi_s(V_{GB})}} e^{[\Psi_s(V_{GB}) - 2\phi_F]/V_{th}} (e^{-V_{SB}/V_{th}} - e^{-V_{DB}/V_{th}}), \quad (6.8)$$

where  $V_{GB}$  is the gate to substrate voltage,  $V_{SB}$  is the source to substrate voltage, and  $V_{DB}$  is the drain to substrate voltage. The surface potential ( $\Psi_s$ ) increases almost linearly with  $V_{GS}$  until it reaches a value of  $2\phi_F$ . After this,  $\Psi_s$  increases very slowly with  $V_{GS}$  and saturates at a value of  $2\phi_F + (4\sim 5)V_{th}$  (at  $V_{GS} = V_{TS}$ ). From Eq.(6.8), it can be said that for  $\Psi_s \leq 2\phi_F$ ,  $I_D$  increases exponentially with  $V_{GS}$ . However, for  $\Psi_s > 2\phi_F$ ,  $\Psi_s$  increases very slowly with  $V_{GS}$ , and, consequently, the subthreshold current loses its exponential nature and tends to saturate. Since the experimental and the theoretical values of  $I_x$  match for values of  $V_{GS}$  upto  $V_{2\phi}$  and differ afterwards, it can be hypothesized that at  $V_{GS} = V_{2\phi}$ , the surface potential ( $\Psi_s$ ) reaches a value of  $2\phi_F$ . Another important feature that can be observed from Fig.6.2 is that the difference between  $V_{TM}$  and  $V_{2\phi}$  is nearly 42 mV. Now from Eq.(6.7), it can be stated that the difference between  $V_{TM}$  and  $V_{2\phi}$  is approximately equal to  $\eta V_{th}$  (37.3 mV). Hence, it can be written that

$$V_{TM} \approx V_{2\phi} + \eta V_{th}. \quad (6.9)$$

This relation gives a new model for the threshold voltage at the ‘onset of the moderate inversion’. Now,  $V_{2\phi}$  can be formulated by putting  $\phi_B = 2\phi_F$  in Eq.(2.16). Therefore, in this work, the proposed model of  $V_{TM}$  can be given as follows

$$V_{TM} \approx V_{FB} + 2\phi_F + \frac{\sqrt{4\epsilon_{si} N_A \phi_F}}{C'_{ox}} + \eta V_{th}. \quad (6.10)$$

According to this definition,  $V_{TM}$  is only 30 to 40 mV higher than  $V_{2\phi}$ . From this model, it can be hypothesized that the ‘onset of the moderate inversion’ does not actually occur at  $\Psi_s = 2\phi_F$ , rather it occurs when  $\Psi_s$  is a few tens of millivolts greater than  $2\phi_F$ .

It has been stated earlier that the theoretical and the experimental values of  $I_x$  do not match near around the threshold ( $V_{GS} = V_{TM}$ ) region. This happens because of the following facts.

- When  $V_{GS}$  varies between  $V_{2\phi}$  and  $V_{TM}$ , the subthreshold current seems to deviate from its exponential model and tends towards saturation. Therefore, Eqs.(6.2) and (6.4) lose their validity in this region.
- Here it is assumed that the subthreshold current ( $I_{sub}$ ) is saturated at a value equal to  $I_{sat}$  for  $V_{GS}$  values beyond  $V_{TM}$ . In fact, when  $V_{GS}$  is varying between  $V_{TM}$  and  $V_{TS}$ ,  $\Psi_s$  does not remain a constant but varies between  $2\phi_F$  and  $2\phi_F + (4\sim 5)v_{th}$ . Consequently,  $I_{sub}$  also does not remain a constant at a value equal to  $I_{sat}$  but varies slowly with  $V_{GS}$  in the moderate inversion region. However, this rate of variation of  $I_{sub}$  with respect to  $V_{GS}$  is too small, and when the drift component of the drain current becomes much larger than the subthreshold component, one can assume  $I_{sub}$  to take on a constant value.

In Section 6.5, a new drain current model is proposed in order to match the results obtained from the theoretical  $I_x$  function with the experimentally obtained values of  $I_x$ .

## 6.4 Verification of the Proposed Method with the Experimental Results for Sub-0.1 $\mu\text{m}$ Devices

The results predicted by the proposed method are also verified with the experimental data reported in the literature for sub-0.1  $\mu\text{m}$  channel length devices. For the experimental data, the  $I_D$ - $V_{GS}$  characteristics for a 0.09  $\mu\text{m}$  channel length device have been taken from the work reported by Mii *et al.* [16]. These characteristics are measured at a constant  $V_{DS}$  (50 mV) and  $V_{GS}$  is incremented from 0 V to 0.5 V in steps of 10 mV. The  $V_x(V_{GS}, I_D)$  and  $I_x(V_{GS}, I_D)$  functions are calculated numerically from the experimental data in the same manner as discussed earlier. In Fig.6.4, the numerically calculated  $I_x(V_{GS}, I_D)$  function is plotted as a function of  $V_{GS}$  (denoted by B) and also as a function of  $V_x(V_{GS}, I_D)$  (denoted by C). The characteristic B shows a negative peak in  $I_x$  at  $V_{GS} = 0.25$  V. Taking  $V_{TM} = 0.25$  V, the parameter extraction procedure for obtaining the values of the model parameters to be used in Eqs.(6.4) and (6.5) has been performed in the same manner as stated previously. After the parameter extraction, the following values of the model parameters are found:  $a = 1.81 \times 10^{-9}$  A,  $b = 26.05$  V $^{-1}$ ,  $\eta = 1.47$ ,  $K_1 = 1.94 \times 10^{-3}$  AV $^{-2.5}$  and  $I_{sat} = 1.25 \times 10^{-6}$  A.

These values of the model parameters are plugged into Eqs.(6.4) and (6.5) and the computed values of  $I_x(V_{GS}, I_D)$  are plotted as a function of  $V_{GS}$  (denoted by A) in Fig.6.4. Both the theoretical and the experimental characteristics of  $I_x(V_{GS}, I_D)$  [curves A and B] show peaks at  $V_{GS} = 0.25$  V. Also, curve C shows a peak at  $V_x = 0.21$  V. The difference between these two peaks is equal to 0.04 V, which is nearly equal to  $\eta v_{th}$  (0.038 V). From Fig.6.4, it can also be seen that the experimental  $I_x(V_{GS}, I_D)$  versus  $V_{GS}$  characteristic starts to deviate from the theoretical  $I_x(V_{GS}, I_D)$  versus  $V_{GS}$  characteristic from  $V_{GS} = 0.21$  V. Therefore, the observations

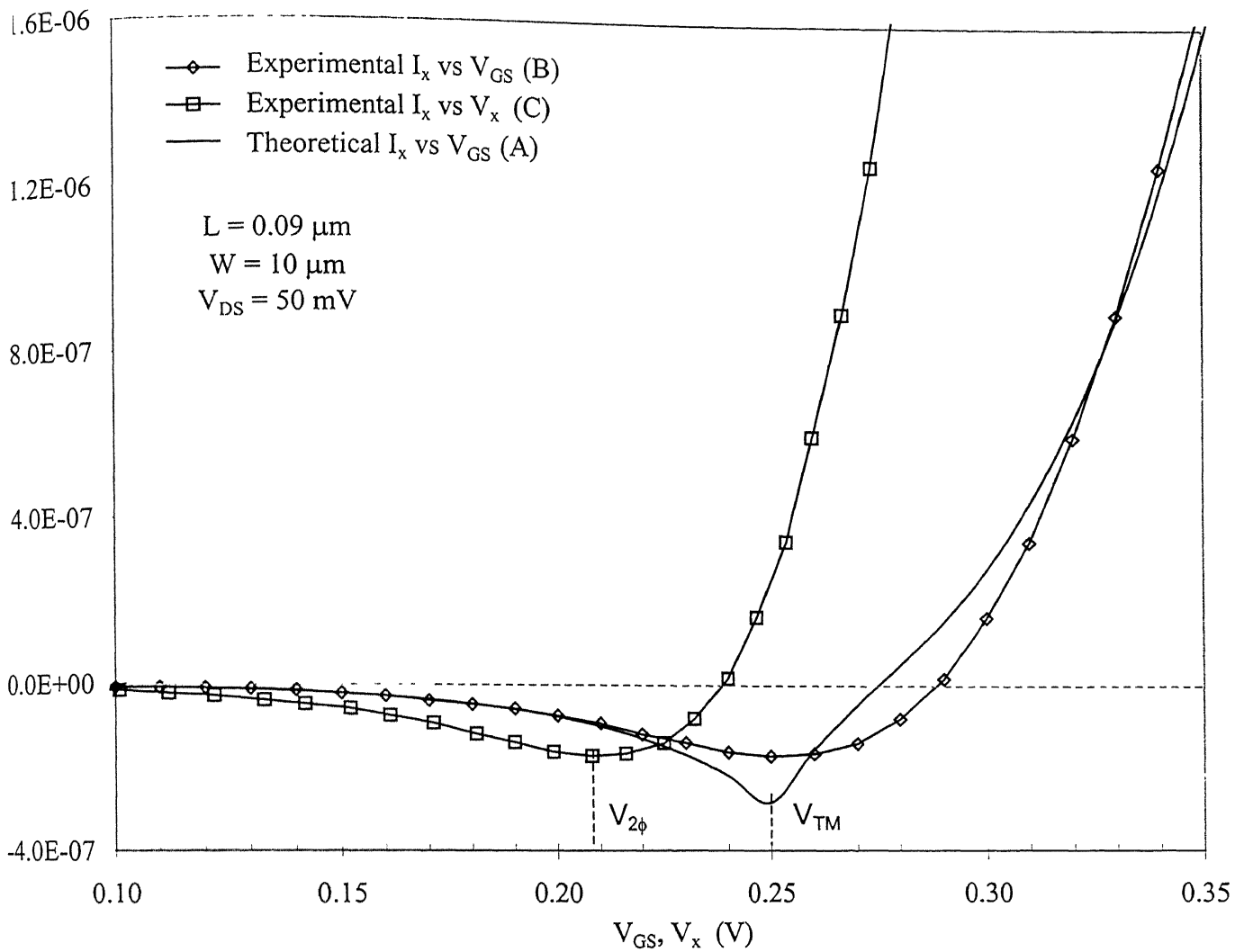


**FIGURE 6.4 :** The  $I_x$  function calculated numerically from the experimental data as reported by Mii *et al.* [16] as a function of  $V_{GS}$  and  $V_x$  (curves B and C respectively). The results simulated from the theoretical model proposed in this work for  $I_x$  [Eqs.(6.4) and (6.5)] are also shown as a function of  $V_{GS}$  (curve A) for comparison.

made for this device are quite similar to that of the 0.26  $\mu\text{m}$  device, given earlier. Hence, it can be stated that the proposed method is also valid for sub-0.1  $\mu\text{m}$  devices.

## 6.5 Further Analysis\*

Near the peak region, the discrepancies between the values of the  $I_x$  function, calculated from the theoretical model and from the experimental data, can be reduced using the drain current model as given by Eq.(6.1). The expression for  $I_x$ , calculated from this drain current model, can be written as

$$I_x = \frac{I_{\text{sat}}}{bV_{\text{DS}}} \left[ \ln \left( \frac{I_{\text{sat}} + a \exp(bV_{\text{GS}})}{I_{\text{sat}} + a} \right) \right] + \int_0^{V_{\text{GS}}} K_1 \left[ s \ln \left( 1 + \exp \left( \frac{V_{\text{GS}} - V_{\text{TM}}}{s} \right) \right) \right]^{1.5} dV_{\text{GS}} \\ - \frac{I_{\text{sat}} \times a \exp(bV_{\text{GS}})}{I_{\text{sat}} + a \exp(bV_{\text{GS}})} - K_1 \left[ s \ln \left( 1 + \exp \left( \frac{V_{\text{GS}} - V_{\text{TM}}}{s} \right) \right) \right]^{1.5} V_{\text{DS}}. \quad (6.11)$$

However, it is not possible to get an analytical expression for the integration term appearing in Eq.(6.11). Hence, in this work, this integration has been performed numerically. For the experimental data, the  $I_D$ - $V_{\text{GS}}$  characteristics for a 0.26  $\mu\text{m}$  channel length device have been taken from the work reported by Langevelde and Klaassen [15]. The value of the parameter  $V_{\text{TM}}$  is found numerically in the same manner as discussed in Section 6.1, which yielded  $V_{\text{TM}} = 0.41$  V, and the parameter extraction procedure is carried out to find the values of the model parameters to be used in Eq.(6.1). The parameter extraction procedure is performed in the same way as stated in Section 4.4. Now, these values of the model parameters (which are listed along

---

\* For a complete derivation of the equations, please see the Appendix

side in Fig.4.3) are plugged into Eq.(6.11) and the values of  $I_x$  are calculated and plotted as a function of  $V_{GS}$ , as shown in Fig.6.5. The  $I_x(V_{GS}, I_D)$  versus  $V_{GS}$  characteristic, which is calculated numerically from the experimental data is also plotted in the same figure. From this figure, it can be seen that the values obtained from the model of  $I_x$  match almost exactly with the values of  $I_x$  calculated numerically from the experimental data. Both the theoretical model and the numerical analysis show negative peaks at  $V_{GS} = 0.41$  V.

The results predicted by the proposed method are also verified with the experimental data reported in the literature for sub-0.1  $\mu\text{m}$  channel length devices. For the experimental data, the  $I_D$ - $V_{GS}$  characteristics for a 0.09  $\mu\text{m}$  channel length device have been taken for  $V_{GS}$  values between 0 V and 0.5 V, from the work reported by Mii *et al.* [16]. The value of the parameter  $V_{TM}$  is extracted numerically as stated in Section 6.1, which yielded  $V_{TM} = 0.25$  V, and the parameter extraction procedure is carried out to find the values of the model parameters in the same way as was done for the 0.26  $\mu\text{m}$  channel length device. The values of the model parameters are listed along side in Fig.4.4. Now, using these values of the model parameters, the  $I_x$  function is calculated and plotted as a function of  $V_{GS}$ , as shown in Fig.6.6. The  $I_x(V_{GS}, I_D)$  versus  $V_{GS}$  characteristic, calculated numerically from the experimental data is also plotted in the same figure. From this figure, it can be seen that the values obtained from the model of  $I_x$  match almost exactly with the values of  $I_x$  calculated numerically from the experimental data. In this case, both the characteristics show negative peaks at  $V_{GS} = 0.25$  V. From these results, it can be strongly concluded that the negative peaks in the  $I_x$ - $V_{GS}$  characteristics always occur at  $V_{GS} = V_{TM}$  (i.e. at the onset of the moderate inversion region).

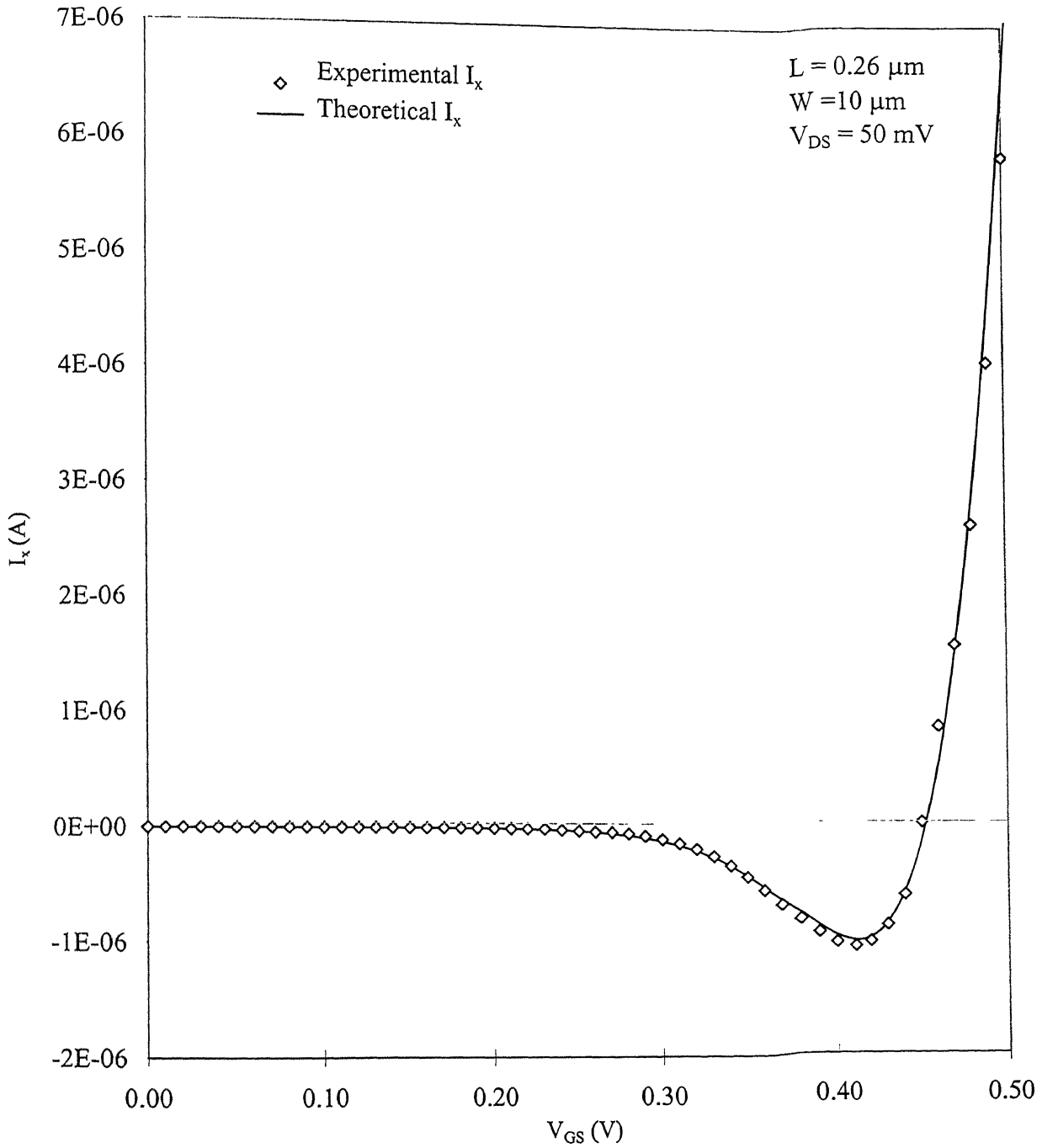


**FIGURE 6.5 :** The  $I_x$  function calculated numerically from the experimental data as reported by Langevelde and Klassen [15] as a function of  $V_{GS}$ . The results simulated from the theoretical model of  $I_x$  [Eq.(6.11)] proposed in this work are also shown as a function of  $V_{GS}$  for comparison.

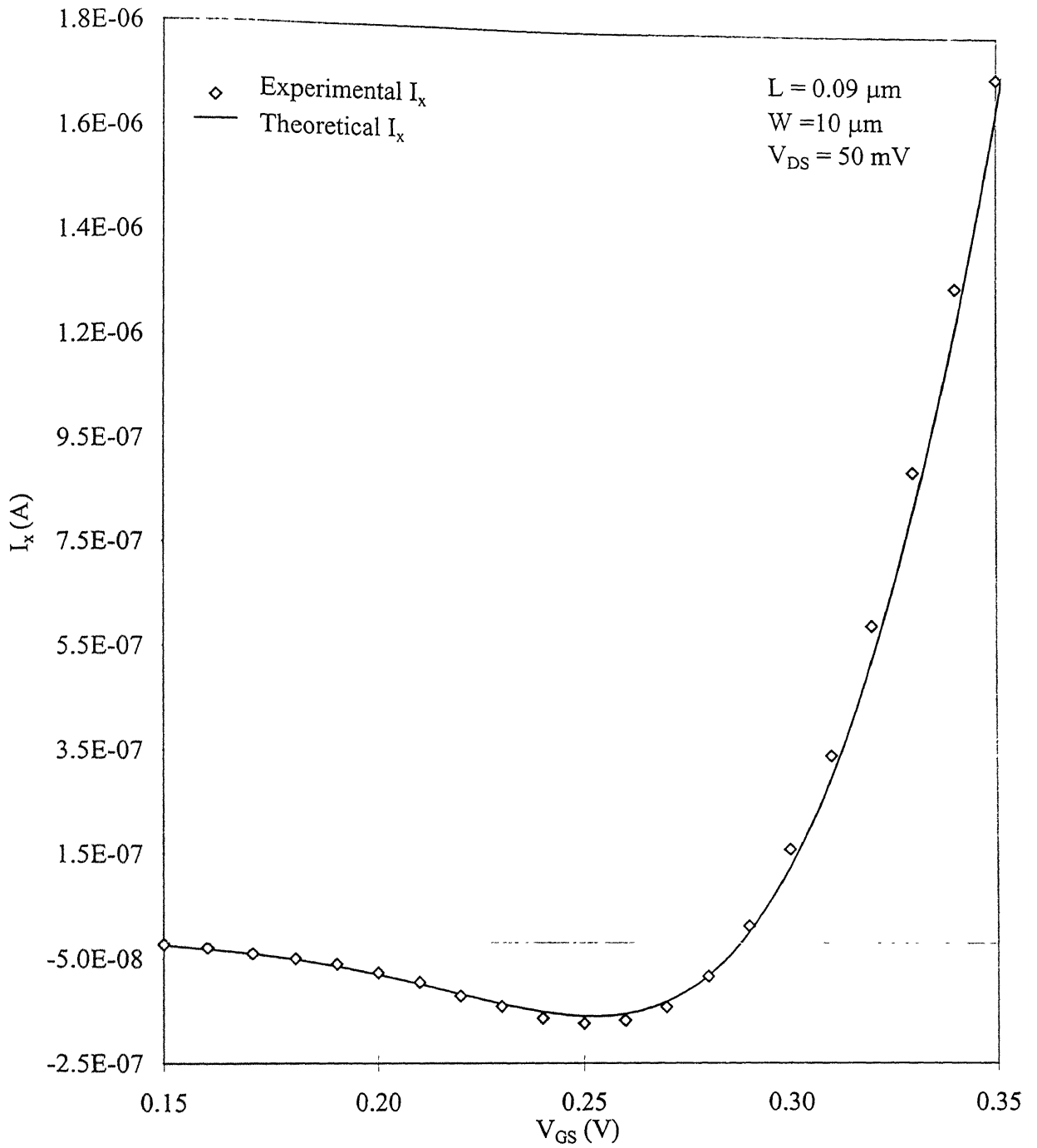


**FIGURE 6.6 :** The  $I_x$  function calculated numerically from the experimental data as reported by Mii *et al.* [16] as a function of  $V_{GS}$ . The results simulated from the theoretical model proposed in this work for  $I_x$  [Eq.(6.11)] are also shown as a function of  $V_{GS}$  for comparison.



## 6.6 Extraction of $V_{TS}$

When  $V_{GS}$  becomes equal to  $V_{TS}$ , the device is at the ‘onset of the strong inversion’. The  $V_{TS}$  extraction method developed in this work is termed as the ‘ $g_{m,max}$ ’ method. In this method, the values of  $g_m$  are calculated from the experimental  $I_D$ – $V_{GS}$  data by differentiating  $I_D$  with respect to  $V_{GS}$  numerically. Now, the value of  $V_{GS}$  at which the value of  $g_m$  attains a maxima, represents the onset of strong inversion (i.e., at this point,  $V_{GS} = V_{TS}$ ). From the discussion in Section 2.4, it can be stated that for  $V_{GS} < V_{TS}$ , the effective mobility ( $\mu_{eff}$ ) increases with  $V_{GS}$  due to the Coulomb scattering effect. However, for  $V_{GS} > V_{TS}$ , the effective mobility ( $\mu_{eff}$ ) decreases with  $V_{GS}$  due to the phonon and the surface roughness scattering effects. As a result,  $g_m$  increases with  $V_{GS}$  below  $V_{TS}$ , peaks at  $V_{GS} = V_{TS}$ , and then decreases with  $V_{GS}$ .

This method of  $V_{TS}$  extraction may contradict with other methods like the  $g_{m,max}/3$  [7] or other linear extrapolation methods. However, it seems that the other methods extract the value of the threshold voltage, which is neither  $V_{TM}$  nor  $V_{TS}$ , rather an intermediate value between the two. This is due to the fact that the other methods do not consider the Coulomb scattering effect, which is dominant in the moderate inversion region.

It is true that the differentiation method adopted in this work for the extraction of  $V_{TS}$  may depend on the series resistance effect and the errors due to noise introduced during measurements. However, for low power analog IC operation,  $V_{TM}$  (onset of the moderate inversion) is much more important than  $V_{TS}$  (onset of the strong inversion). Hence, the accuracy in the extraction of  $V_{TS}$  is not that much important for analog IC design. Therefore, in this work, much more importance is given on the extraction of an accurate value for  $V_{TM}$  rather than  $V_{TS}$ .

Moreover, an accurate modeling of  $V_{TS}$  seems to be a difficult task, since the assumption that  $Q'_d \gg Q'_i$  does not quite hold in this region.

In the next chapter, the proposed method is verified with the simulated data for devices having various gate lengths and widths. The effect of the parasitic series resistance on the proposed method has also been observed. The performance of the proposed method has been compared with other existing threshold voltage extraction methods.

# Reliability Test of the Proposed Method

---

The threshold voltage of short channel MOSFETs is dependent on the channel length ( $L$ ) and the channel width ( $W$ ) of the device. The S/D series resistances also have an important role to play in determining the drain current characteristics for short channel MOSFETs. In this chapter, all these short channel effects are discussed. Also, the proposed method of  $V_{TM}$  extraction is tested for devices having different channel lengths and widths. The results are compared with other threshold voltage extraction methods. The effect of the source/drain resistance on various existing threshold voltage extraction methods is also presented in this chapter.

## 7.1 Effect of Channel Length on the Threshold Voltage ( $V_{TM}$ )

MOSFETs with short channel lengths experience a shift in the threshold voltage with a change in the channel length (e.g., when  $L$  decreases,  $V_{TM}$  also decreases). An explanation for this shift in the threshold voltage for short channel devices can be given in terms of the charge sharing (or the charge conservation) concept [7]. This model [7] considers the sharing of the depletion charge in the regions where the gate depletion zone overlaps with the depletion zones

of the source and the drain contacts. This shared charge is balanced by the counter charges distributed between the gate electrode and the source and the drain contacts. As a result of this charge sharing, the effective depletion charge, which is induced by the gate voltage, is reduced. Hence, the model of  $Q'_d$ , as given by Eq.(2.14), no longer holds good. Including the charge sharing effect, Eq.(2.16) can be rewritten in the following way [11]

$$\hat{V}_{TM} = V_{FB} + \phi_B + \gamma\sqrt{\phi_B + V_{SB}}\left(1 - \frac{\alpha_1\delta}{L}\sqrt{\phi_B + V_{SB}}\right), \quad (7.1)$$

where  $\delta$  is given by  $\delta = \sqrt{\frac{2\epsilon_{si}}{qN_A}}$ , and  $\hat{V}_{TM}$  is the effective threshold voltage. Here  $\alpha_1$  is a dimensionless fitting parameter. With a decrease in the channel length ( $L$ ), the threshold voltage also decreases. This phenomenon should be reflected in the extracted value of the threshold voltage from the experimental  $I_D$ - $V_{GS}$  characteristics. In order to examine the effect of the channel length on the threshold voltage extraction procedure, AIM-SPICE simulation has been performed on a representative device. The level-17 MOSFET model of AIM-SPICE is used in the simulation, and the following parameters are used: a mask channel width of 5  $\mu\text{m}$ , an oxide thickness of 10 nm, a substrate doping of  $10^{16} \text{ cm}^{-3}$ , a channel doping concentration of  $10^{17} \text{ cm}^{-3}$ , and a threshold voltage of 0.7 V at zero substrate bias. For the other parameters (e.g., the low field mobility, the mobility degradation coefficient, etc.), the default values of the level-17 model are taken. The value of  $V_{DS}$  is taken to be a constant at 50 mV and  $V_{GS}$  is incremented from 0 V to 1.5 V in steps of 10 mV. Five  $I_D$ - $V_{GS}$  characteristics have been simulated for five different values of channel length (e.g., 0.5  $\mu\text{m}$ , 0.4  $\mu\text{m}$ , 0.3  $\mu\text{m}$ , 0.2  $\mu\text{m}$ , and 0.1  $\mu\text{m}$ ). From these five simulated characteristics, threshold voltages have been extracted using the GMLE method [9],

the TC method [13], and the proposed method. The first two methods can be discussed as follows.

1. **The GMLE Method [9]:** The simulated  $I_D$  versus  $V_{GS}$  characteristics are numerically differentiated with respect to  $V_{GS}$  in order to obtain the transconductance ( $g_m$ ) versus  $V_{GS}$  characteristics. The linear region of the  $g_m$  versus  $V_{GS}$  characteristics is extrapolated and its intersection with the  $V_{GS}$  axis gives the threshold voltage.
2. **The TC Method [13]:** The simulated  $I_D$  versus  $V_{GS}$  characteristics are numerically differentiated with respect to  $V_{GS}$  in order to obtain the  $g_m$  versus  $V_{GS}$  characteristics. Again, these characteristics are differentiated with respect to  $V_{GS}$  in order to get the second derivative of  $g_m$  with respect to  $V_{GS}$  (i.e.,  $\partial^2 g_m / \partial V_{GS}^2$ ) versus  $V_{GS}$  characteristics. The value of  $V_{GS}$ , at which the value of  $\partial^2 g_m / \partial V_{GS}^2$  is maximum, is taken to be the threshold voltage of the device.

In Fig.7.1, the extracted values of the threshold voltage from each of these methods are plotted as a function of the channel length. It can be seen that the results of the method proposed in this work are consistent with the theory, and also the extracted values of the threshold voltage using the proposed method are comparable to others, and lie intermediate between the values extracted by the other two methods.

## 7.2 Effect of Channel Width on the Threshold Voltage ( $V_{TM}$ )

MOSFETs with narrow channel widths also experience a shift in the threshold voltage with a change in the channel width (e.g., when  $W$  decreases,  $V_{TM}$  increases). For a MOSFET, the

depletion region under the gate is not limited to just the area directly below the thin oxide, rather some of the field lines emanating from the gate charges terminate on the ionized acceptor atoms on either side of the gate along the width of the channel. These field lines constitute what is called a fringing field. If  $W$  is large, the part of the depletion region on the two sides of the gate along the width of the channel is a small percentage of the total depletion volume, and, thus, it can be neglected. However, with values of  $W$  of only a few micrometers or less, the side parts of the depletion region become a significant fraction of the total depletion volume. Thus, the total effective depletion charge under the gate is increased, and, therefore, the threshold voltage increases with decreasing channel width. Including this narrow channel effect, Eq.(2.16) can be rewritten in the following way [11]

$$\hat{V}_{TM} = V_{FB} + \phi_B + \gamma\sqrt{\phi_B + V_{SB}}\left(1 + \frac{\alpha_2\delta\pi}{2W}\sqrt{\phi_B + V_{SB}}\right), \quad (7.2)$$

where  $\alpha_2$  is a dimensionless fitting parameter. In order to examine the effect of the channel width on the threshold voltage extraction procedure, AIM-SPICE simulation has been performed on a representative device. The level-17 MOSFET model in SPICE is used for this simulation, and the same values for the various parameters are used as stated in the preceding section. Here, the channel length is kept constant at  $0.5\text{ }\mu\text{m}$ , and four  $I_D$ - $V_{DS}$  characteristics have been simulated for four different values of gate width (e.g.,  $10\text{ }\mu\text{m}$ ,  $8\text{ }\mu\text{m}$ ,  $6\text{ }\mu\text{m}$ , and  $5\text{ }\mu\text{m}$ ). From these four simulated characteristics, the threshold voltages have been extracted using the GMLE method [9], the TC method [13], and the method proposed in this work. In Fig.7.2, the extracted values of the threshold voltage from each method are plotted as a function of the channel width. It can be seen that the results of the method proposed in this work are consistent with the theory, and

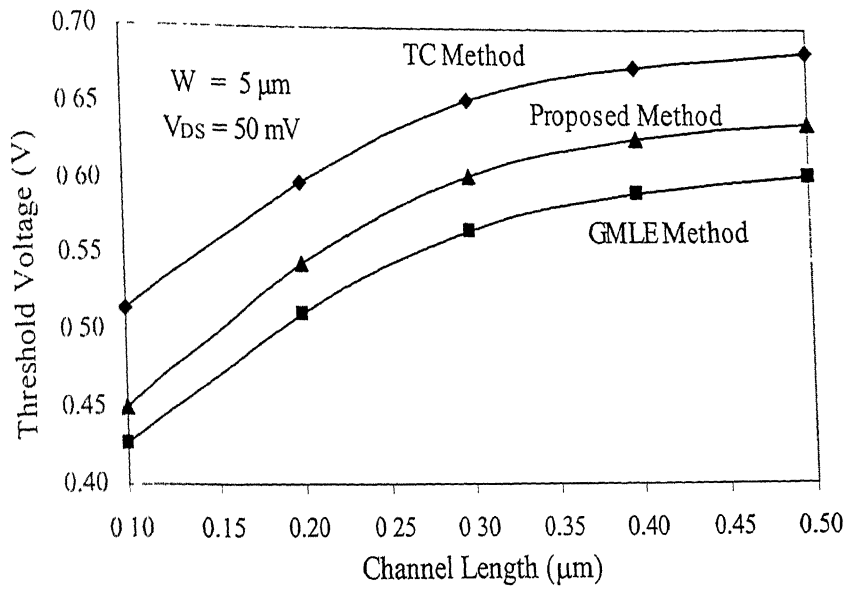


**FIGURE 7.1 :** Simulated values of the threshold voltage extracted by the GMLE method [9], the TC method [13], and the method proposed in this work as a function of the channel length (based on the results from AIM-SPICE simulation).

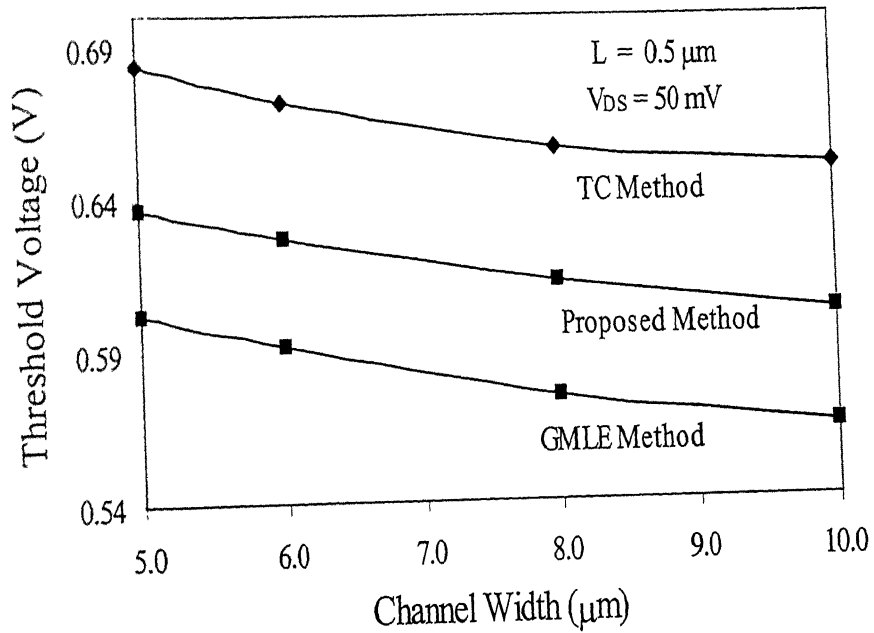


**FIGURE 7.2 :** Simulated values of the threshold voltage extracted by the GMLE method [9], the TC method [13], and the method proposed in this work as a function of the channel width (based on the results from AIM-SPICE simulation).

also the extracted values of the threshold voltage using the proposed method are comparable to others, and lie intermediate between the values extracted by the other two methods.

### 7.3 Effects of Source/Drain Series Resistance on the Extraction of the Threshold Voltage ( $V_{TM}$ )

The channel of a MOSFET is in series with two ‘parasitic’ resistances, one associated with the source and the other associated with the drain. A schematic diagram of the current-flow pattern in the source/drain region of a MOSFET is shown in Fig.7.3. The symbols (e.g.,  $l_c$ ,  $S$ ,  $\rho_c$ ,  $x_j$ ,  $x_c$ , and  $R_{sd}$ ) that appear in Fig.7.3 will be defined in the subsequent sections. The total source/drain resistance can be divided into several parts:  $R_{ac}$  is the accumulation layer resistance in the gate-source (or the gate-drain) overlap region where the current mainly stays near the surface;  $R_{sp}$  is associated with current spreading from the surface layer uniformly across the depth of the source-drain junction;  $R_{sh}$  is the sheet resistance of the source/drain region where the current flows uniformly, and  $R_{co}$  is the contact resistance (including the spreading resistance in silicon under the contact) in the region where the current flows into a metal line.

Once the current flows into the metal line, there is very little additional resistance introduced, since the resistivity of aluminum (which is commonly used as the interconnect metal) is very low ( $\rho_{AL} \approx 3 \times 10^{-6} \Omega\text{-cm}$  [31]). In VLSI interconnects, the thickness of the aluminum interconnects is typically between 0.5–1.0  $\mu\text{m}$ . Therefore, the sheet resistivity is of the order of 0.05  $\Omega/\square$ . This is negligible in comparison with the channel sheet resistivity  $\rho_{ch}$ , which is typically between 2000–7000  $\Omega/\square$ , except when a long, thin wire is used as the interconnect. Figure 7.3 only shows the series resistance on one side of the device. The total source/drain



resistance per device is, of course, twice of that shown in Fig. 7.3. The accumulation layer resistance  $R_{ac}$  depends on the gate voltage. Since it is not easily separable from the active channel resistance,  $R_{ac}$  is considered to be a part of the resistance of the channel having an effective length ( $L_{eff}$ ) of the device. The other components of the source/drain resistance can be modeled as discussed below [31].

### 7.3.1 The Spreading Resistance ( $R_{sp}$ )

The spreading resistance  $R_{sp}$  is given by [31]

$$R_{sp} = \frac{2\rho_j}{\pi W} \ln 0.75 \frac{x_j}{x_c}, \quad (7.3)$$

where  $W$  is the device width, and  $x_j$  and  $x_c$  are the junction depth and the inversion (or accumulation) layer thickness respectively. As shown in Fig.7.4, the current spreading takes place in a uniformly doped medium with resistivity  $\rho_j$ .

### 7.3.2 The Sheet Resistance ( $R_{sh}$ )

The sheet resistance  $R_{sh}$  is given by [31]

$$R_{sh} = R_{sd} \frac{S}{W}, \quad (7.4)$$

where  $S$  is the spacing between the gate edge and the contact edge, and  $R_{sd}$  is the sheet resistivity of the source-drain diffusion, typically of the order of 50–500  $\Omega/\square$  [31]. Since the equivalent value of  $R_{sd}$  is much smaller than that of  $\rho_{ch}$ , this term is usually negligible if  $S$  is kept to a minimum, limited by the overlay tolerance between the contact and the gate lithographic levels.

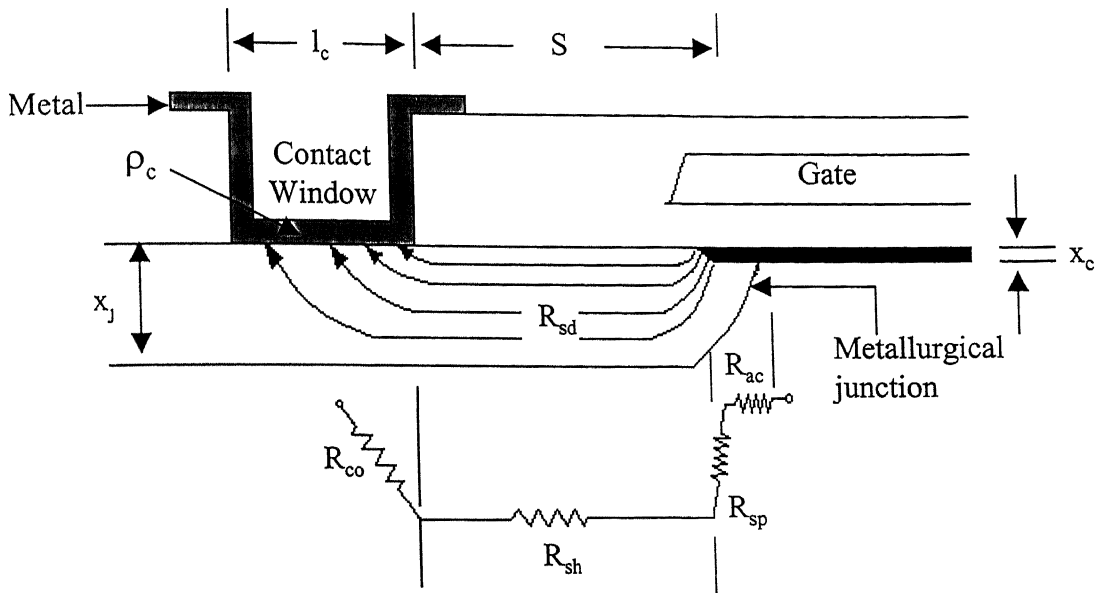


**FIGURE 7.3 :** A schematic cross section showing the pattern of current flow from a MOSFET channel through the source or drain region to the aluminum contact [31]. The diagram identifies various contributions to the series resistance.

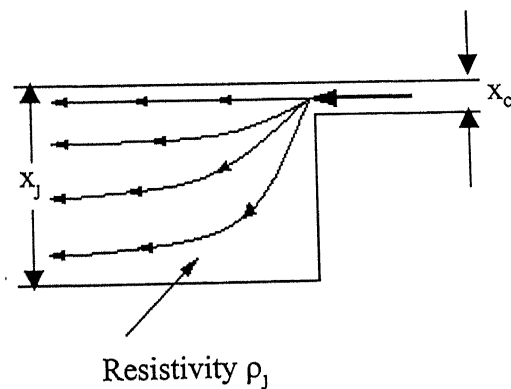


**FIGURE 7.4 :** A schematic diagram showing the resistance component associated with the injection region where the current spreads from a thin surface layer into a uniformly doped source or drain region [31].

### 7.3.3 The Contact Resistance ( $R_{co}$ )

The contact resistance  $R_{co}$  is given by [31]

$$R_{co} = \frac{\sqrt{R_{sd}\rho_c}}{W} \coth l_c \sqrt{\frac{R_{sd}}{\rho_c}}, \quad (7.5)$$

where  $l_c$  is the width of the contact window (Fig.7.3), and  $\rho_c$  is the interfacial contact resistivity (in  $\Omega\text{-cm}^2$ ) of the ohmic contact between the metal and silicon.

Now, the effective gate voltage ( $V_{GS,eff}$ ) and the effective drain voltage ( $V_{DS,eff}$ ) can be defined as

$$V_{GS,eff} = V_{GS} - I_D R_S \quad \text{and} \quad V_{DS,eff} = V_{DS} - I_D (R_D + R_S), \quad (7.6)$$

where  $R_D$  and  $R_S$  are the drain and source parasitic series resistances respectively and are given by  $R_S (R_D) = R_{co} + R_{sp} + R_{sh}$ . Thus, these parasitic resistances degrade both the  $V_{GS,eff}$  and  $V_{DS,eff}$ . As a result, there is a degradation of the drain current for short channel devices with low intrinsic resistance. This effect is more severe for ultra-short channel MOSFETs. As the device sizes are scaled down, the effective source/drain diffusion cross-sectional area also goes down, and, consequently, the source/drain series resistance increases. Moreover, in ultra short channel MOSFETs, LDD (lowly doped drain) structure is used in order to eliminate the hot electron hazards. This LDD structure also tends to increase the parasitic series resistance. The effect of series resistances is shown with the help of AIM-SPICE simulation in Fig.5.1(a). How these characteristics are obtained is discussed in Chapter 5. From these characteristics, the threshold voltage is extracted using the GMLE method [9], the TC method [13], and the method proposed in this work. Then, for each method, the error in the extracted values for  $V_T$  is calculated using the following equation

$$\% \text{ error} = \frac{V_T|_{R_d, R_s \neq 0} - V_T|_{R_d, R_s = 0}}{V_T|_{R_d, R_s = 0}} \quad (7.7)$$

This error value is plotted in Fig.7.5 as a function of source/drain resistance for each of the extraction methods. Since the proposed method can filter out the parasitic resistance effect, hence, it shows the least error among the three methods, and, therefore, it can be stated that this method is more reliable for ultra-short-channel length devices where the series resistances are too high.

## 7.4 Mathematical Complexity of the Proposed Method

It is more time consuming to perform a numerical integration than a numerical differentiation on a digital processor. Therefore, the proposed method for the threshold voltage extraction may take longer time than the extraction methods based on differentiation techniques, when it is executed on a computer. However, the computational time of the proposed method can be greatly reduced if one properly chooses the integration limits of the proposed  $V_x$  and  $I_x$  functions. If  $V_{\text{low}}$  and  $V_{\text{high}}$  are the lower and the upper limits of integration, then in this work it is found that  $V_{\text{low}} = V_{\text{TM}} - 0.1 \text{ V}$  and  $V_{\text{high}} = V_{\text{TM}} + 0.05 \text{ V}$  is a sufficient condition for getting a negative peak at the onset of the moderate inversion region. The function  $I_x$  is calculated from the experimental data for the  $0.26 \mu\text{m}$  channel length device [15] for two cases: in the first case,  $V_{\text{low}}$  and  $V_{\text{high}}$  are taken to be equal to  $0 \text{ V}$  and  $1.5 \text{ V}$  respectively, and is plotted in Fig.7.6 (denoted by curve A). In the second case,  $V_{\text{low}}$  and  $V_{\text{high}}$  are taken to be equal to  $0.31 \text{ V}$  ( $= V_{\text{TM}} - 0.1 \text{ V}$ ) and  $0.46 \text{ V}$  ( $= V_{\text{TM}} + 0.05 \text{ V}$ ) respectively, and is also plotted in Fig.7.6 (denoted by curve B). Both the curves show negative peaks at  $V_{\text{GS}} = 0.41 \text{ V}$ .

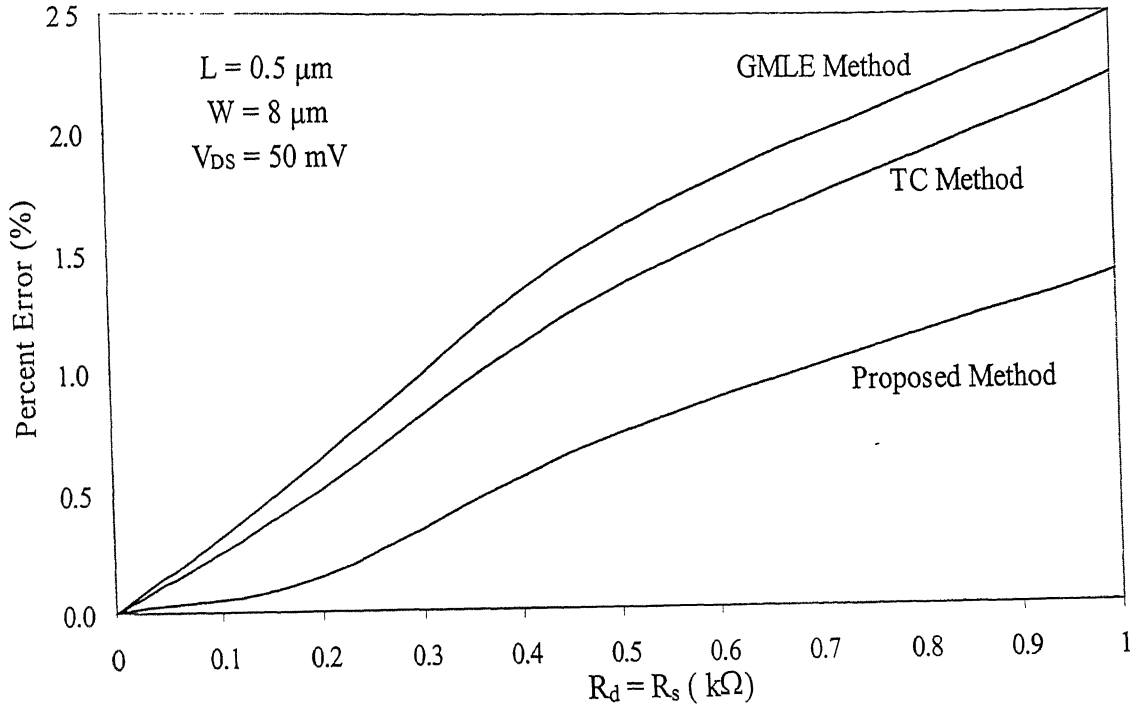


**FIGURE 7.5 :** Comparison of the percent error in the extraction of the threshold voltages using the GMLE method [9], the TC method [13], and the method proposed in this work as a function of S/D resistance, based on the results of AIM-SPICE simulation.

The same procedure has been repeated with the experimental data for a  $0.09\text{ }\mu\text{m}$  channel length device [16]. In this case, curve A in Fig.7.7 is found by taking  $V_{\text{low}} = 0\text{ V}$  and  $V_{\text{high}} = 0.5\text{ V}$ , and curve B in the same figure is found by taking  $V_{\text{low}} = 0.15\text{ V}$  and  $V_{\text{high}} = 0.3\text{ V}$ . It is to be noted here also that both the characteristics show negative peaks at  $V_{\text{GS}} = 0.25\text{ V}$ . Hence, it can be concluded that by a proper choice of the integration limits, the mathematical complexity and the computational time of the proposed method can be greatly reduced.

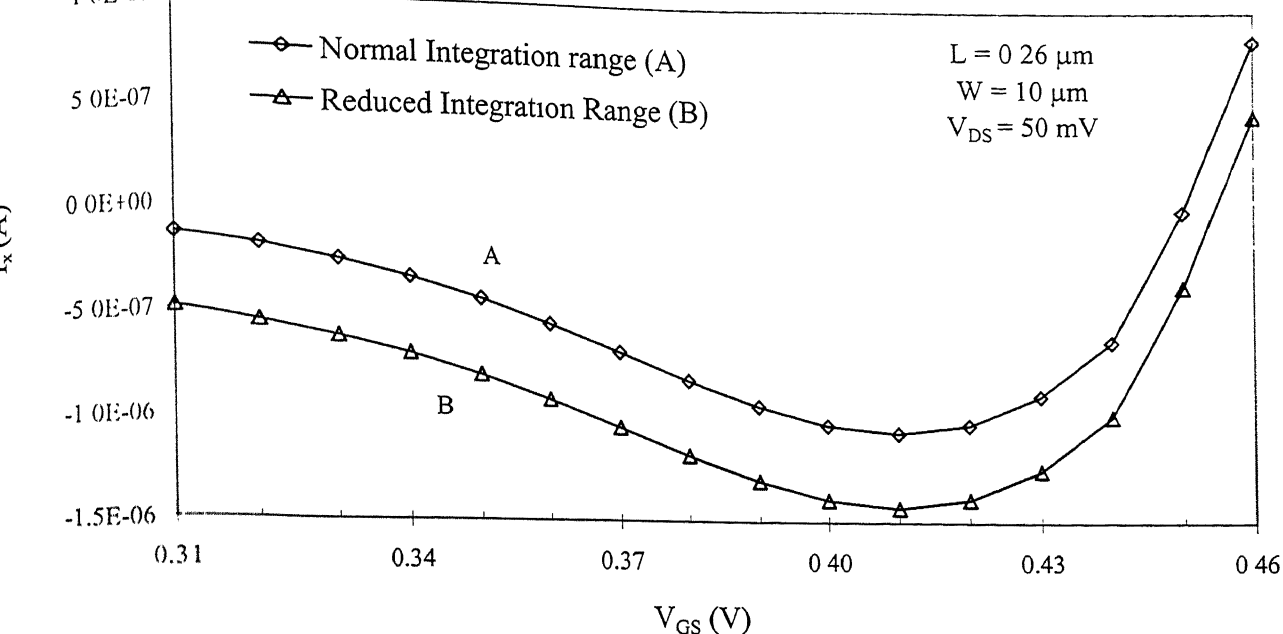


**FIGURE 7.6 :** The  $I_x$  function calculated numerically from the experimental data, as reported by Langevelde and Klaassen [15], as a function of  $V_{GS}$  for two different integration limits.

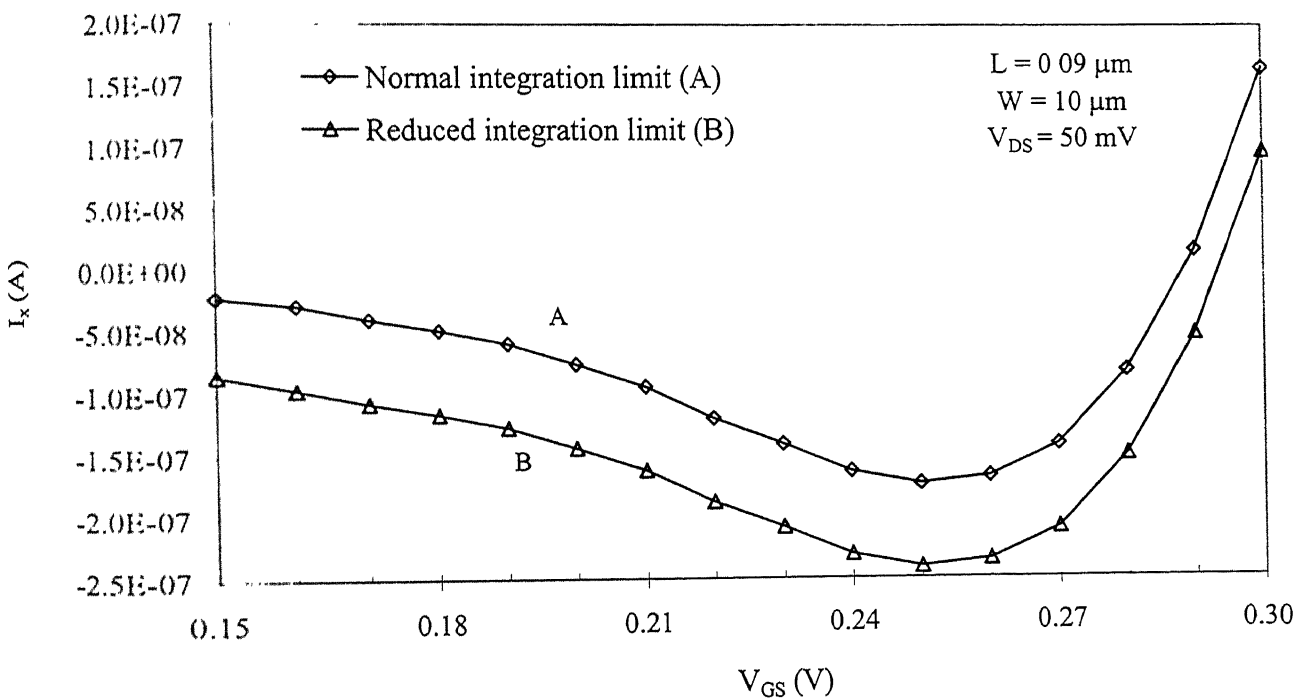


**FIGURE 7.7 :** The  $I_x$  function calculated numerically from the experimental data, as reported by Mii *et al.* [16], as a function of  $V_{GS}$  for two different integration limits.

# Summary and Conclusion

---

With the growing interest in mixed analog/digital circuit design in recent years, the use of MOS transistors has not only been restricted to digital circuit design alone, but also it has been extended to analog circuit design as well. With analog VLSI gaining popularity day by day, the moderate inversion region (i.e., the transition region between the subthreshold region and the strong inversion region) of operation of MOSFETs is becoming increasingly important for circuit designers. This region becomes particularly important with the continuous downscaling of MOS transistors towards submicron dimensions and the subsequent decrease in the power supply voltage. A point will soon be reached when the power dissipation alone will be the most important factor governing the performance, reliability, and the overall system cost. Therefore, this growth of low power analog circuit design has given rise to the need for developing accurate MOSFET models, which are capable of explaining the device behavior in the moderate inversion region.

To date, several drain current models have been proposed in the literature in order to explain the MOSFET dc characteristics. Although these models are quite adequate to explain the device characteristics in the strong and the weak inversion regions, however, most of them have



failed to explain the device behavior accurately in the moderate inversion region because of the following facts.

- These drain current models use the value of the threshold voltage, which does not represent the onset of the moderate inversion region.
- These models use different types of smoothing functions or interpolation techniques in order to join the weak inversion and the strong inversion components of the drain current near the threshold region, and these models depend on these so-called smoothing functions for explaining the moderate inversion region behavior. As a result, these models fail to represent the moderate inversion region characteristics accurately.
- These models use the well known BSIM mobility model, which is quite accurate in the strong inversion region, however, it seems to lose its validity in the moderate inversion region.

In consequence of these drawbacks, these drain current models are applicable only for the digital IC design purpose but not for the analog one. Also, an accurate model for the effective mobility of the inversion layer electrons in the moderate inversion region is extremely important for the design of low power analog ICs.

Another issue, which is tremendously important for low power analog IC design, is the proper extraction and modeling of the threshold voltage parameter. The existing threshold voltage extraction methods suffer from the following shortcomings.

- They can not extract the threshold voltage at the ‘onset of the moderate inversion region’, i.e., when the inversion layer electron density become equivalent to the substrate doping density.
- These extraction procedures are highly influenced by the parasitic source-drain resistance effect and the experimental noise error.

In this work, an effort has been made in order to propose a new improved mobility model and a threshold voltage extraction procedure in order to portray the moderate inversion region more accurately. A brief summary of this work is given below.

## 8.1 Summary of the work

As presented in literature [2,5,9], the Coulomb scattering effect is the most important in influencing the effective mobility ( $\mu_{\text{eff}}$ ) of the channel electrons in the moderate inversion region. Due to this effect,  $\mu_{\text{eff}}$  increases with increasing values of  $V_{\text{GS}}$ , in the moderate inversion region. This phenomenon is opposite to the results found from the widely used BSIM mobility model [6]. This is due to the fact that the BSIM mobility model does not consider the Coulomb scattering effect in the moderate inversion region, rather it considers only the phonon scattering and the surface roughness scattering effects in the strong inversion region. In this work, an attempt has been made in order to propose a new mobility model so that the device behavior in the moderate inversion region can be explained accurately. A new function  $U(V_{\text{GS}})$  has been proposed in this work in such a manner that when the existing BSIM mobility model is multiplied with it then one gets the modified mobility model, which can explain the Coulomb scattering phenomena in the moderate inversion region and has no effect in the strong inversion

region. An effort has also been made in order to propose a new drain current model for the moderate inversion region. This model can be immensely helpful to the low power analog circuit designers for the hand calculation of the drain current in the moderate inversion region.

Results obtained from the proposed model have been verified with the experimental data for a  $0.26\ \mu\text{m}$  [15] and a  $0.09\ \mu\text{m}$  [16] channel length MOSFET, which shows a perfect match between the two. Hence, it can be concluded that the mobility model developed in this work here is more reliable and accurate in describing the drain current characteristics in the moderate inversion region for short channel MOSFETs.

In this work, a new threshold voltage extraction method has been developed. The difference (D) function, proposed by Conde *et al.* [10], has been modified in order to apply it for three terminal devices. Based on their work, two new functions  $V_x(I_D, V_{GS})$  and  $I_x(I_D, V_{GS})$  have been proposed in this work. From the experimental  $I_D$ – $V_{GS}$  characteristics of any MOSFET, the  $V_x(I_D, V_{GS})$  and  $I_x(I_D, V_{GS})$  functions are calculated numerically. A negative peak appears in the  $I_x(I_D, V_{GS})$  function when it is plotted as a function of  $V_{GS}$ . It has been proved in this work that the gate to source voltage ( $V_{GS}$ ) at which this peak occurs, represents the ‘onset of the moderate inversion’ (i.e.  $V_{TM}$ ). A similar negative peak in the  $I_x(I_D, V_{GS})$  function appears when it is plotted as a function of  $V_x(I_D, V_{GS})$ . In this work, it is found that the separation between these two peaks in the  $I_x$  function is approximately equal to  $\eta V_{th}$  Volts. From theoretical calculation, it is observed that this second peak appears when the surface potential ( $\Psi_s$ ) becomes twice of the bulk potential ( $\phi_F$ ). From this result, a new model for the threshold voltage ( $V_{TM}$ ) have been proposed in this work, which can be expressed as

$$V_{TM} \approx V_{FB} + 2\phi_F + \frac{\sqrt{4\epsilon_{si} N_A \phi_F}}{C'_{ox}} + \eta V_{th}.$$

The proposed threshold voltage extraction method is different from the other methods in a sense that it extracts the threshold voltage from the experimental  $I_D$ - $V_{GS}$  data at the ‘onset of the moderate inversion’. Therefore, the proposed method and model for the threshold voltage extraction is much more accurate and reliable for device characterization for low power analog IC design.

Also, an attempt has been made to propose an alternative method for the extraction of  $V_{TS}$  (i.e., the threshold voltage at the onset of the strong inversion). However, we have not put much effort for the accuracy of this  $V_{TS}$  extraction procedure, since this parameter is not that important for low power analog IC design.

In summary, it can be stated that the proposed method for the threshold voltage extraction has the following advantages over the other existing extraction methods [9,12-14].

- It extracts the threshold voltage at the onset of the moderate inversion region.
- The extraction procedure uses the integral function, which acts as a low pass filter, and suppresses the error due to noise that may be introduced during the measurements.
- The extracted value of the threshold voltage is independent of the source/drain parasitic series resistance.

The results predicted by the proposed method is compared with the recently reported experimental results for 0.26  $\mu m$  [15] and 0.09  $\mu m$  [16] channel length devices. Also, its

performance has been studied and compared with the other methods with the help of AIM-SPIICE simulator. The short channel and the narrow channel effects and the parasitic series resistance effect on the threshold voltage extraction method are also observed using the AIM-SPIICE simulator. Although the proposed method has a computational complexity comparable to that of the linear extrapolation method, it has the advantage of being less sensitive to the measurement error and noise and being independent of the parasitic resistance effect.

## Scope for Improvement

- The subthreshold slope model as proposed by Thakare and Dutta [32] is based on the assumption that the subthreshold slope parameter is independent of the variation of the gate to source voltage ( $V_{GS}$ ). However, in reality, due to the Coulomb scattering effect, the subthreshold slope becomes a function of  $V_{GS}$ . Hence, there is a scope for improvement of that subthreshold slope model [32] using the results of the present work.
- The proposed mobility model can be further improved by considering the transconductance overshoot effect for ultra short channel MOSFETs, with the help of the correction factor  $F_v$  as proposed by Kolhatkar and Dutta [33].
- In this work, the numerical integration for the proposed threshold voltage extraction method has been performed using the Simpson's rule of the numerical integration. The computation time of the proposed threshold voltage extraction method can be highly reduced if any numerical integration method can be developed which is faster than the commonly used (e.g., Simpson's rule, trapezoidal rule, etc.) integration techniques.

# References

---

- [1] Y.P. Tsividis and K. Suyama, "MOSFET modeling for analog circuit CAD: problems and prospects", *IEEE J. Solid-State Circuits*, vol. 29, no. 3, pp. 210-216, March 1994.
- [2] S. Takagi, A. Toriumi, M. Iwase, and H. Tango, "On the universality of inversion layer mobility in Si MOSFETs: Part-I – Effects of substrate impurity concentration", *IEEE Trans. Electron Devices*, vol. 41, no. 12, pp. 2357-2362, December 1994.
- [3] J.R. Hauser, "Extraction of experimental mobility data for MOS devices", *IEEE Trans. Electron Devices*, vol. 43, no. 11, pp. 1981-1988, November 1996.
- [4] S. Manzini, "Effect of Coulomb scattering in n-type silicon inversion layers", *J. Appl. Phys.*, vol. 57, no. 2, pp. 411-414, January 1985.
- [5] J. Banqueri, J.A. LoÁpez-Villanueva, P. Cartujo-Cassinello, S. RodrÃ³iguez, and J.E. Carceller, "Experimental determination of the effective mobility in NMOSFETs: a comparative study", *Solid-State Electron.*, vol. 43, no. 4, pp. 701-707, April 1999.
- [6] B.J. Sheu, D.L. Scharfetter, P.K. Ko, and M.C. Jeng, "BSIM : Berkeley short channel IGFET model for MOS transistors", *IEEE J. Solid-State Circuits*, vol. SC-22, no. 4, pp. 558-565, August 1987.

- [7] T. Fjeldly, T. Ytterdal, and M.S. Shur, "Introduction to Device Modeling and Circuit Simulation", John Wiley and Sons, New York, 1998.
- [8] A. Ortiz-Conde, J. Rodriguez, F.J. Garcia-Sanchez, and J.J. Liou, "An improved definition for modeling the threshold voltage of MOSFETs ", *Solid-State Electron.*, vol. 42, no. 9, pp. 1743-1746, September 1998.
- [9] M. Tsuno, M. Suga, M. Tanaka, K. Shibahara, M.M. Mattausch, and M. Hirose, "Physically-based threshold voltage determination for MOSFETs of all gate lengths", *IEEE Trans. Electron Devices*, vol. ED-46, no. 7, pp. 1429-1433, July 1999.
- [10] A. Ortiz-Conde, E.D.G. Fernandes, J.J. Liou, R. Hassan, F.J. Garcia-Sanchez, G.D. Mercato, and W. Wong, "A new approach to extract the threshold voltage of MOSFETs", *IEEE Trans. Electron Devices*, vol. ED-44, no. 9, pp. 1523-1527, September 1997.
- [11] Y.P. Tsividis, "Operation and Modeling of the MOS Transistors", McGraw-Hill International Edition, New York, 1988.
- [12] L.A. Akers and J.J. Sanchez, "Threshold voltage models of short, narrow and small geometry MOSFETs : a review", *Solid-State Electron.*, vol. 25, no. 7, pp. 621-641, July 1982.
- [13] H.S. Wong, M.H. White, T.J. Krutsick, and R.V. Booth, "Modeling of transconductance degradation and extraction of threshold voltage in thin oxide MOSFETs", *Solid-State Electron.*, vol. 30, no. 9, pp. 953-968, September 1987.

- [14] M. Sasaki, H. Ito, and T. Horiuchi, "A new method to determine effective channel length, series resistance and threshold voltage", *Proceedings of the 1996 IEEE International Conference on Microelectronic Test Structures*, vol. 9, no. 3, pp. 139-144, March 1996.
- [15] R.V. Langevelde and F.M. Klaassen, "An explicit surface-potential-based MOSFET model for circuit simulation", *Solid-State Electron.*, vol. 44, no. 3, pp. 409-418, March 2000.
- [16] Y. Mii, S. Rishton, Y. Taur, D. Kern, T. Lee, K.A. Jenkins, D. Quinlan, T. Brown, Jr., D. Danner, F. Sewell, and M. Polcari, "Experimental high performance sub-0.1  $\mu\text{m}$  channel nMOSFETs", *IEEE Electron Dev. Lett.*, vol. 15, no. 1, pp. 28-30, January 1994.
- [17] M.S. Shur, "Physics of Semiconductor Devices", Prentice Hall, New Jersey, 1990.
- [18] J. Lindmayer and C.Y. Wrigley, "Fundamentals of Semiconductor Devices", D. Van Nostrand Company Inc., New Jersey, 1966.
- [19] N. Yang, W.K. Henson, and J.R. Hauser, "Estimation of the effects of remote charge scattering on electron mobility of n-MOSFETs with ultrathin gate oxides", *IEEE Trans. Electron Devices*, vol. 47, no. 2, pp. 440-446, February 2000.
- [20] H.S. Momose, M. Ono, T. Yoshitomi, T. Ohguro, S. Nakamura, M. Saito, and H. Iwai, "1.5 nm direct-tunneling gate oxide Si MOSFETs", *IEEE Trans. Electron Devices*, vol. 43, no. 8, pp. 1233-1241, August 1996.
- [21] S.M. Sze, "Physics of Semiconductor Devices", Wiley Eastern Ltd., New Delhi, 1981.



- [22] Victor I. Fistul, "Heavily Doped Semiconductors", Pentium Press, New York, 1969.
- [23] Charles Kittel, "Introduction to Solid State Physics", John Wiley and Sons, New York, 1996.
- [24] B.R. Nag, "Theory of Electrical Transport in Semiconductors", Pergamon Press, Oxford, 1972.
- [25] B.K. Ridley, "Quantum Processes in Semiconductors", Clarendon Press, Oxford, 1988.
- [26] F. Stern and W.E. Howard, "Properties of semiconductor surface inversion layers in the electric quantum limit", *Phys. Rev.*, vol. 163, no. 3, pp. 816-835, November 1967.
- [27] D. Deshpande and A.K. Dutta, "A new unified model for submicron MOSFETs", *Microelectronics Journal*, vol. 29, no. 8, pp. 565-570, August 1998.
- [28] C.C. Enz, F. Krummenacher, and E.A. Vittoz, "An analytical MOS transistor model valid in all regions of operation and dedicated to low-voltage and low-current applications", *Journal of Analog Integrated Circuits and Signal Processing*, vol. 8, no. 1, pp. 83-114, July 1995.
- [29] Gnuplot Users' Manual, Department of Computer Science, Dartmouth University, [www.cs.dartmouth.edu/gnuplot/gnuplot.html](http://www.cs.dartmouth.edu/gnuplot/gnuplot.html).
- [30] F.J. Garcia Sanchez, A. Ortiz-Conde, and J.J. Liou, "Parasitic series resistance-independent method for device-model parameter extraction", *IEE Proc. – Circuits Devices Syst.*, vol. 143, no. 1, pp. 68-70, February 1996.

- [31] Y. Taur and T.H. Ning, "Fundamentals of Modern VLSI Devices", Cambridge University Press, Cambridge, 1998.
  
- [32] S.B. Thakare and A.K. Dutta, "A new improved model for subthreshold slope for submicron MOSFETs", *Microelectronics Journal*, vol. 31, no.2, pp. 105-111, February 2000.
  
- [33] J.S. Kolhatkar and A.K. Dutta, "A new mobility model to explain the transconductance overshoot effect observed in ultra-short channel length MOSFETs", *Solid-State Electron.*, vol. 44, no. 4, pp. 691-696, April 2000.

# Appendix

---

Here, an effort has been made in order to find the analytical expressions for the  $I_x$  and  $V_x$  functions, where use has been made of the drain current model [as given by Eqs.(6.2) and (6.3)].

## A1. Calculation of $I_x$ in the Subthreshold Region

From Eq.(6.2), it can be written that

$$I_D = I_0 \exp\left(\frac{V_{GS} - V_{TM}}{\eta v_{th}}\right) \quad \text{for } V_{GS} < V_{TM},$$

and, hence,

$$\begin{aligned} I_x &= \int_0^{V_{GS}} g_D dV_{GS} - I_D \\ &= \int_0^{V_{GS}} \frac{I_0}{V_{DS}} \exp\left(\frac{V_{GS} - V_{TM}}{\eta v_{th}}\right) dV_{GS} - I_0 \exp\left(\frac{V_{GS} - V_{TM}}{\eta v_{th}}\right) \\ &= \int_0^{V_{GS}} \frac{a \exp(bV_{GS})}{V_{DS}} dV_{GS} - a \exp(bV_{GS}) \\ &= \frac{a}{bV_{DS}} [\exp(bV_{GS}) - 1] - a \exp(bV_{GS}) \\ &= \frac{a}{bV_{DS}} \exp(bV_{GS}) [1 - bV_{DS}] - \frac{a}{bV_{DS}} \end{aligned} \tag{A.1}$$

where  $a = I_0 \exp\left(-\frac{V_{TM}}{\eta v_{th}}\right)$ , and  $b = \frac{1}{\eta v_{th}}$ .

## A2. Calculation of $I_x$ in the Moderate Inversion Region

Again, from Eq.(6.3), it can be written that

$$I_D = I_{sat} + K_1(V_{GS} - V_{TM})^{1.5} V_{DS} \quad \text{for } V_{GS} > V_{TM} \quad (A.2)$$

In order to calculate  $I_x$  in the moderate inversion region, it is divided into two components:  $I_{x1}$  and  $I_{x2}$ , where  $I_{x1}$  is the subthreshold component and  $I_{x2}$  is the drift current component. The component  $I_{x1}$  can be calculated in the following manner, noting that for  $V_{GS} < V_{TM}$ ,  $I_{sub} = a e^{bV_{GS}}$ , and for  $V_{GS} > V_{TM}$ ,  $I_{sub} \approx I_{sat}$ .

$$\begin{aligned} I_{x1} &= \int_0^{V_{GS}} g_D dV_{GS} - I_D \\ &= \int_0^{V_{TM}} \frac{I_{sub}}{V_{DS}} dV_{GS} + \int_{V_{TM}}^{V_{GS}} \frac{I_{sub}}{V_{DS}} dV_{GS} - I_{sub} \\ &= \int_0^{V_{TM}} \frac{a \exp(bV_{GS})}{V_{DS}} dV_{GS} + \int_{V_{TM}}^{V_{GS}} \frac{I_{sat}}{V_{DS}} dV_{GS} - I_{sat} \\ &= \frac{a}{bV_{DS}} [\exp(bV_{TM}) - 1] + \frac{I_{sat}}{V_{DS}} [V_{GS} - V_{TM}] - I_{sat} \\ &= \frac{1}{bV_{DS}} [I_0 - a] + \frac{I_{sat}}{V_{DS}} [V_{GS} - V_{TM}] - I_{sat} \end{aligned} \quad (A.3)$$

The component  $I_{x2}$  can be calculated in the following manner, noting that for  $V_{GS} < V_{TM}$ ,  $I_{inv} \approx 0$ , and for  $V_{GS} > V_{TM}$ ,  $I_{inv} = K_1(V_{GS} - V_{TM})^{1.5} V_{DS}$ .

$$\begin{aligned} I_{x2} &= \int_0^{V_{GS}} g_D dV_{GS} - I_D \\ &= \int_0^{V_{GS}} \frac{I_{inv}}{V_{DS}} dV_{GS} - I_{inv} \end{aligned}$$

$$\begin{aligned}
&= \int_{V_{TM}}^{V_{GS}} \frac{K_1 (V_{GS} - V_{TM})^{1.5} V_{DS}}{V_{DS}} dV_{GS} - K_1 (V_{GS} - V_{TM})^{1.5} V_{DS} \\
&= \frac{K_1 (V_{GS} - V_{TM})^{2.5}}{2.5} - K_1 (V_{GS} - V_{TM})^{1.5} V_{DS} .
\end{aligned} \tag{A.4}$$

Hence, the total current  $I_x$  can be given by

$$\begin{aligned}
I_x &= I_{x1} + I_{x2} \\
&= \frac{1}{bV_{DS}} [I_0 - a] + \frac{I_{sat}}{V_{DS}} [V_{GS} - V_{TM}] - I_{sat} + \frac{K_1 (V_{GS} - V_{TM})^{2.5}}{2.5} - K_1 (V_{GS} - V_{TM})^{1.5} V_{DS} .
\end{aligned} \tag{A.5}$$

### A3. Calculation of $V_x$ at the Subthreshold Region

The function  $V_x$  can be calculated in the following manner.

$$\begin{aligned}
V_x &= V_{GS} - \frac{\int_0^{V_{GS}} g_D dV_{GS}}{g_D} \\
&= V_{GS} - \frac{\int_0^{V_{GS}} \frac{I_0}{V_{DS}} \exp\left(\frac{V_{GS} - V_{TM}}{\eta v_{th}}\right) dV_{GS}}{\frac{I_0}{V_{DS}} \exp\left(\frac{V_{GS} - V_{TM}}{\eta v_{th}}\right)} \\
&= V_{GS} - \frac{I_0 \exp\left(-\frac{V_{TM}}{\eta v_{th}}\right) \int_0^{V_{GS}} \exp\left(\frac{V_{GS}}{\eta v_{th}}\right) dV_{GS}}{I_0 \exp\left(\frac{V_{GS} - V_{TM}}{\eta v_{th}}\right)}
\end{aligned}$$

$$\begin{aligned}
&= V_{GS} - \frac{\eta v_{th} I_0 \exp\left(-\frac{V_{TM}}{\eta v_{th}}\right) \left[ \exp\left(\frac{V_{GS}}{\eta v_{th}}\right) - 1 \right]}{I_0 \exp\left(\frac{V_{GS} - V_{TM}}{\eta v_{th}}\right)} \\
&= V_{GS} - \eta v_{th} \left[ 1 - \exp\left(-\frac{V_{GS}}{\eta v_{th}}\right) \right].
\end{aligned} \tag{A.6}$$

#### A4. Calculation of $I_x$ from the Accurate Drain Current Model

In this section,  $I_x$  is calculated from the drain current model as given by Eq.(6.1). Thus,

$$I_D = \frac{I_{sat} I_0 e^{\frac{V_{GS} - V_{TM}}{\eta v_{th}}}}{I_{sat} + I_0 e^{\frac{V_{GS} - V_{TM}}{\eta v_{th}}}} + K_1 V_{GTMX}^{1.5} V_{DS}. \tag{A.7}$$

Hence,

$$\begin{aligned}
I_x &= \int_0^{V_{GS}} g_D dV_{GS} - I_D \\
&= \int_0^{V_{GS}} \left[ \frac{I_{sat} I_0 e^{\frac{V_{GS} - V_{TM}}{\eta v_{th}}} + K_1 V_{GTMX}^{1.5} V_{DS}}{I_{sat} + I_0 e^{\frac{V_{GS} - V_{TM}}{\eta v_{th}}}} \right] dV_{GS} - \frac{I_{sat} I_0 e^{\frac{V_{GS} - V_{TM}}{\eta v_{th}}}}{I_{sat} + I_0 e^{\frac{V_{GS} - V_{TM}}{\eta v_{th}}}} - K_1 V_{GTMX}^{1.5} V_{DS} \\
&= \int_0^{V_{GS}} \frac{I_{sat} I_0 e^{\frac{V_{GS} - V_{TM}}{\eta v_{th}}}}{V_{DS} \left( I_{sat} + I_0 e^{\frac{V_{GS} - V_{TM}}{\eta v_{th}}} \right)} dV_{GS} + \int_0^{V_{GS}} K_1 V_{GTMX}^{1.5} dV_{GS} - \frac{I_{sat} I_0 e^{\frac{V_{GS} - V_{TM}}{\eta v_{th}}}}{I_{sat} + I_0 e^{\frac{V_{GS} - V_{TM}}{\eta v_{th}}}} - K_1 V_{GTMX}^{1.5} V_{DS} \\
&= \frac{I_{sat}}{b V_{DS}} \left[ \ln \left( \frac{I_{sat} + a e^{b V_{GS}}}{I_{sat} + a} \right) \right] + \int_0^{V_{GS}} K_1 V_{GTMX}^{1.5} dV_{GS} - \frac{I_{sat} a e^{b V_{GS}}}{I_{sat} + a e^{b V_{GS}}} - K_1 V_{GTMX}^{1.5} V_{DS}.
\end{aligned} \tag{A.8}$$